Stony Brook University

OFFICIAL COPY

The official electronic file of this thesis or dissertation is maintained by the University Libraries on behalf of The Graduate School at Stony Brook University.

© All Rights Reserved by Author.

Powder Diffraction Tells You What Your Material Really Is: Case Studies

A Dissertation Presented

by

Saul H. Lapidus

to

The Graduate School

in Partial Fulfillment of the Requirements

for the Degree of

Doctor of Philosophy

in

Physics

Stony Brook University

May 2012

Stony Brook University

The Graduate School

Saul H. Lapidus

We, the dissertation committee for the above candidate for the Doctor of Philosophy degree, hereby recommend acceptance of this dissertation.

Peter W. Stephens – Dissertation Advisor
Professor, Department of Physics and Astronomy

Abhay Deshpande – Chairperson of Defense
Associate Professor, Department of Physics and Astronomy

Maria Victoria Fernandez-Serra
Assistant Professor, Department of Physics and Astronomy

Eric Dooryhee
Powder Diffraction Group Leader
National Synchrotron Light Source II, Brookhaven National Laboratory

This dissertation is accepted by the Graduate School.

Charles Taber
Interim Dean of the Graduate School

Abstract of the Dissertation

Powder Diffraction Tells You What Your Material Really Is: Case Studies

by

Saul H. Lapidus

Doctor of Philosophy

in

Physics

Stony Brook University

2012

Powder diffraction is a useful tool for examining a number of materials that do not form single crystal for a variety of reasons. Unlike with single crystals, structure determination with powders is not a routine task. In order to demonstrate the ability and efficacy of powder diffraction and its contribution to the understanding the correlation of structures and properties, a series of compounds will be presented from a wide range of types of materials: polymorphic materials, cocrystals, metal organic frameworks and magnetic materials. Each of these represent the forefront of the ability of powder diffraction, as they all introduce complications through large

numbers of independent molecules and/or disorder.

Two families of materials will be presented in detail, coordination polymers containing pyrazine and HF_2^- and Prussian Blue analogs, that were investigated with powder diffraction.

The bifluoride ion, HF_2^-, contains a two-coordinate H-atom exhibiting the strongest known hydrogen bond. This was used to form materials of the form, $Ni(HF_2)(pyz)_2X$ (X = PF_6^-, SbF_6^-). These materials are quasi-1D magnets, with magnetic pathways along the biflouride ion. Two polymorphs of the PF_6^- version were found and have different magnetic behavior, directly related to the structure. Additionally a number of compounds of novel and unknown composition were found and their structure was determined, $Ni_2F_2(pyz)_3(H_2O)_4(BF_4)_2$ and $NiF(pyz)_{1.5}(H_2O)_2$ TaF_6.

$Cs_2Mn^{II}[Mn^{II}(CN)_6]$ has the archetypal *fcc* Prussian blue structure, with the cations in the cubic voids. Substitution with smaller alkali ions lead to structural distortions and a marked increase in ordering temperatures. On the other hand, substitution of larger cations, NMe_4^+ drives a rearrangement of the Mn-CN-Mn network and produce several previously unobserved Mn^{II} coordination geometries and an unexpected structure.

To my wife, Carrie, and my daughter, Yvette.

Contents

List of Figures

List of Tables

Acknowledgements

First, I would like to thank my loving wife, Carrie, who has supported me through my many years at Stony Brook. Without her, I would not have made it to this point. My children, Yvette and Henri (who at the time of writing has yet to be born), bring me never-ending joy and inspire me to do my best as their father. My own parents, Harris and Diane, have been a guiding force in my life and their love and support have been never-ending.

The guidance and support that I have received from my advisor, Peter W. Stephens, has been key to my success. Though I will no longer be his graduate student, I look forward to continue to work with him in the future as a collaborator. Additionally, I would like to thank the other graduate student in our group, Kevin Stone, as he is always open to discussions and trouble shooting particularly hard problems.

Finally, I would like to point out a number of friends and fellow graduate students whose camaraderie have been particularly felt: Nathan Borggren, Amber Carr, Kevin Dusling, Marija Kotur, Jason Reeves, Phillip Schiff, Stephen Webb, and Clint Young.

Chapter 1

Introduction

Currently, there is a large amount of scientific effort in the discovery of new materials with particular desired properties. In order to understand the properties of these new materials, it is critical to determine how these compounds are arranged. Crystalline materials are particularly amenable to such an investigation. A crystal is a pattern of atoms that is made up by a particular subdivision, the unit cell, which repeats and fills space and thus determination of the contents of the unit cell is equivalent to finding the structure of the whole material.

Diffraction is a probe of the crystal structure of a material. William Lawrence and William Henry Bragg were able to determine a relationship between the spacing of atomic planes and the angle of diffraction peaks (Equation 1.1). This arises from constructive interference of the reflected light between two planes separated by a distance *d*. (Figure 1.1) In any particular compound there are many such planes, which arises to a variety of diffraction peaks.

$$\lambda = 2d \sin\theta \tag{1.1}$$

Figure 1.1: Schematic Diagram of Bragg's law.

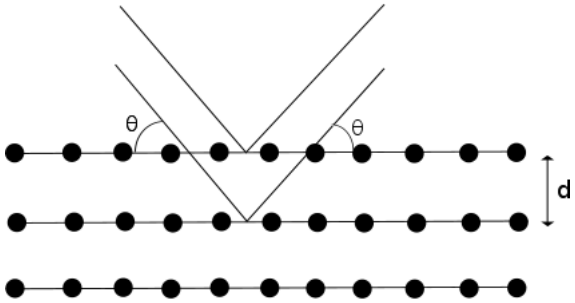

An alternate formulation was developed by von Laue, which is based off scattering off individual atoms rather than planes. Consider two identical atoms, separated by $\vec{x}$, which are diffracting x-rays with initial wave vector $\vec{k}$ which scatter to wave vector $\vec{k'}$. (Figure 1.2) The path length difference between these two rays will be given by $\vec{x} \cdot (\hat{k} - \hat{k'})$, where $\vec{x}$ is the displacement between the two atoms. In order to have constructive interference, this path length difference must be an integer number of wavelengths and thus $\vec{x} \cdot (\vec{k} - \vec{k'}) = 2\pi m$.

This can be extended by considering a crystal made up of a unit cell with one atom. Each of these units cells are then separated by a lattice vector, $\vec{R}$, and each must constructively interfere in order to get a diffraction peak. Thus the diffraction condition can be written as $e^{i\vec{R}\cdot\vec{K}} = 1$, where $\vec{K} = \vec{k} - \vec{k'}$.

The von Laue formulation is especially useful since it is easily extendable to a unit cell consisting of more than one atom. Consider a unit cell consisting

Figure 1.2: Schematic Diagram of two atomic scatters.

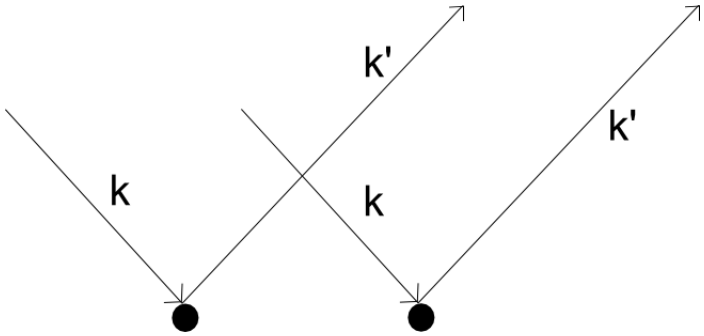

of atoms at positions $\vec{d_i}$ in the unit cell and thus the amplitude of diffraction will be proportional to the moduli of:

$$S_{\vec{K}} = \sum_j \mathrm{e}^{i\vec{K}\cdot\vec{d_j}}, \tag{1.2}$$

which is called the geometrical structure factor. This structure factor can be generalized to a unit cell consisting of different types of atoms by the introduction of an atomic form factor, $f_j(\vec{K})$, which results in Equation 1.3. Thus, the diffraction pattern of a compound is related to the discrete Fourier transform of the crystal structure.

$$S_{\vec{K}} = \sum_j f_j(\vec{K})\mathrm{e}^{i\vec{K}\cdot\vec{d_j}}, \tag{1.3}$$

where the atomic form factor is given by:

$$f_j(\vec{K}) = -\frac{1}{e}\int \mathrm{d}\vec{r}\ \mathrm{e}^{i\vec{K}\cdot\vec{r}}\rho_j(\vec{r}). \tag{1.4}$$

In an experiment, the quantity actually measured is the moduli of the structure factor, $|S_{\vec{K}}|^2$. Thus it is not possible to directly calculate the struc-

ture via a Fourier transformation as the phases are not known. This situation is known as the phase problem in crystallography and in single crystal x-ray diffraction it is has been basically solved through the use of direct methods [1].

Single crystal x-ray diffraction is a powerful and widely used technique and the basis for the enormous growth in knowledge of structural chemistry that has occurred in the past generation. However, there are circumstances for which suitable single crystals are not routinely available. In particular, solvates and polymorphs are frequently unavailable as single crystals because of the nonequilibrium nature of their preparation. Growth of suitable single crystals may also be difficult with low solubility compounds, which might not be amenable to controlled crystal growth of single crystals from solution. Additionally it is important to undertake structural studies at the conditions of interest (e.g. near the magnetic ordering temperature). If a phase transition occurs between room temperature and these conditions, it is not uncommon for the single crystal to fragment or heavily twin.

Powder diffraction, instead of using a single crystal, takes the opposite limit and is based a sample being made of a large number of crystallites forming an ensemble of different orientations. This means that a powder pattern contains much less information than a single crystal data set because random orientation of the crystallites that compose powder cause the three-dimensional (3D) reciprocal lattice to collapse onto a single dimension. Consequently, multiple Bragg peaks can overlap in a powder pattern and thus cannot be measured independently.

Structure solution from powder diffraction can be considered in six steps:

sample preparation, data collection, determination of the unit cell or indexing, Pawley fit, preliminary structure determination, and Rietveld refinement. Each of these steps will be discussed in detail in the following sections.

1.1 Sample Preparation

As used in this research, a powder is ideally a polycrystalline mass made of approximately 1 μm crystallites, each of typically 10^6 - 10^9 unit cells. [2] The size of crystallites is important in order to guarantee good powder averaging and having large crystallites in the sample can result in strange and unusable peak shapes, as such often a sample is lightly ground before measurement. An example of this is shown in Figure 1.3, where different graininess of the sample resulted in widely different diffraction patterns.

Additionally, it is preferable that the sample be relatively free of micros-

Figure 1.3: An example of large crystallite size resulting in strange peak shape. The sample is $Cu(pyz)_2HF_2$ ClO_4. [3] a) A very grainy sample. Diffraction pattern is unusable. b) Sample was lightly round which greatly improved the pattern, however some small evidence of graininess can be observed. c) Sample was spun in a capillary in order to improve powder averaging, resulting in relatively smooth continuous peaks.

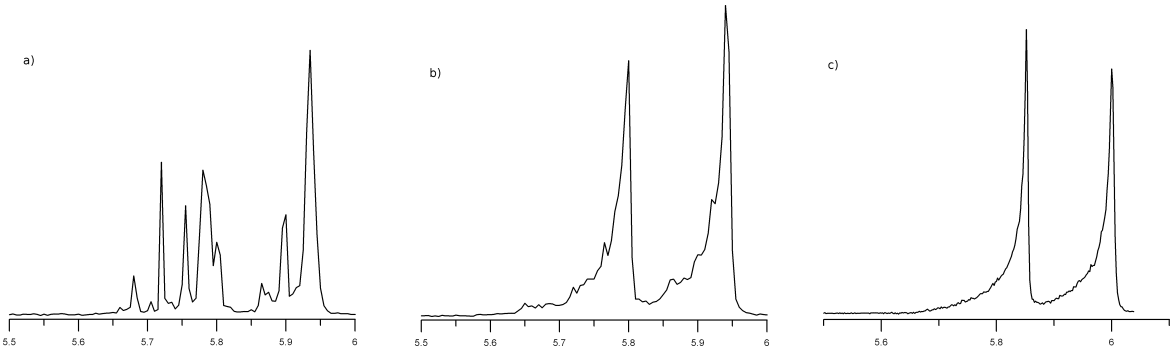

Figure 1.4: Different preparations of Fe $(C_4(CN)_8)_{1/2}$TCNE [4] that highlight sample to sample variations. Differences in quality arose from air exposure and solvent content.

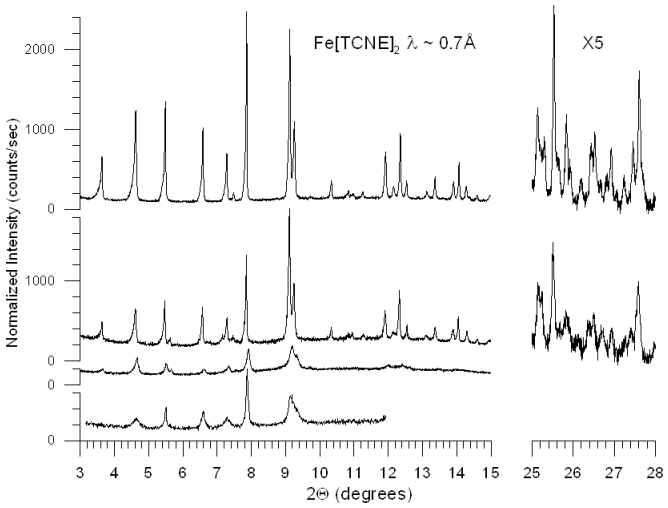

train in order to be able to accurately resolve peaks. An important effect of this is that not all samples of a material are of the same quality and often many versions of the same material may need to be measured. A particularly strong example of this phenomenon is "$Fe[TCNE]_2$" or Fe $(C_4(CN)_8)_{1/2}$TCNE, [4] which had a wide variation of quality between samples. (Figure 1.4)

1.2 Data Collection

Figure 1.5: Schematic illustrating the experimental setup at beamline X16C at the NSLS for a high resolution powder diffraction measurement.

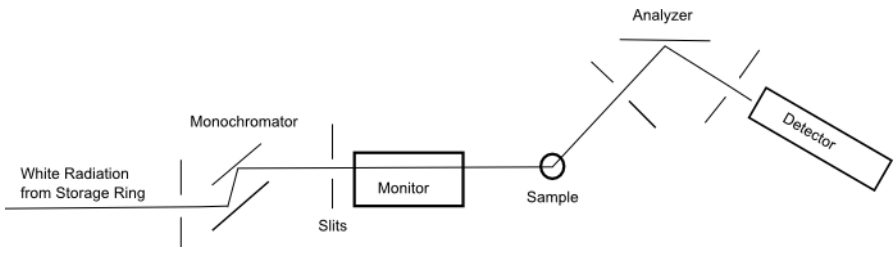

Figure 1.6: Picture of the diffractometer and experimental setup at beamline X16C.

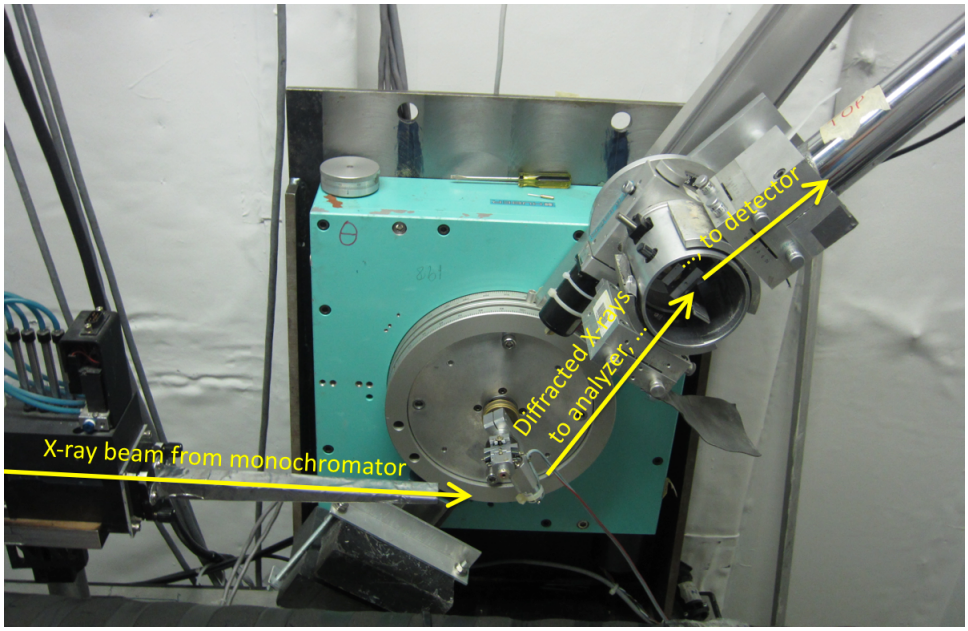

A number of factors must be considered in the measurement of a powder diffraction pattern, much of which are dependant on the material to be studied. The first of which is the wavelength that the diffraction pattern will be measured at. The wavelength must be chosen to take into account the composition of the sample, in order to deal with possible absorption issues. Secondly, the geometry of the sample, capillary or flat plate, must be decided upon. A flat plate measurement will allow for more of the sample to be measured, but increase the probability for preferred orientation effects as well as introduces the need for illuminated volume corrections. A capillary measurement reduced preferred orientation and the ability to spin the capillary will help with powder averaging. Furthermore, it is possible to cause radiation damage to the sample, which would cause variations in the diffraction pattern

over time. As such, diffraction patterns at different times should be compared. It is possible to avoid radiation damage by moving the sample across the x-ray beam; however this may introduce variations of the diffraction pattern due to spatial differences in the sample. A large number of other parameters must be considered and as such it is vital to not think of powder diffraction as a black box.

All diffraction patterns in this dissertation were measured at the National Synchrotron Light Source (NSLS) at either beamline X16C or X12A. Both beamlines had a similar experimental setup. From the storage ring, highly collimated white radiation is produced by synchrotron radiation and defined into a beam by a series of white beam slits. A Si(111) channel-cut monochromator is used to select a particular wavelength. Generally experiments were performed at $\sim$0.7 Å as we have found that this balances well between flux and reduction of absorption from the sample. This monochromatic beam is then further defined by slits and monitored by an ion chamber. After diffracting from the sample, the x-rays are analyzed by a Ge(111) single-reflection crystal and detected using a NaI scintillation counter. As the flux from the storage varies in time, the detector signal is normalized by the monitor counts. (Figures 1.5 and 1.6)

1.3 Unit Cell Determination or Indexing

The first step in analyzing a powder diffraction pattern is the determination of a unit cell, also known as indexing. The unit cell will be defined by dimensions: a, b, c, α, β and γ, where α, β and γ are the angles between b and

c, c and a, and a and b. By accurately determining peak positions, d-spacings can be determined with the use of Bragg's Law. The goal of indexing is to find a function f:$\mathbb{Z}^3 \to \mathbb{R}$ with the form of

$$\frac{1}{d^2} = Ah^2 + Bk^2 + Cl^2 + Dkl + Ehl + Fhk \tag{1.5}$$

where h, k and l are the Miller indices of a particular peak. Thus indexing can be restated as finding a set of A,B,C,D,E and F that correspond to the observed d-spacings and from these parameters the unit cell can be determined. [5] A space group can be assigned by systematic absences in the given peak list and further confirmed by a Pawley fit and finalizing the structure solution.

There are many ways to determine such a function. The simplest such way is guessing that the first peak corresponds to a particular peak, for instance (100), and repeat such guessing for a number of peaks and from which the cell can be determined. However this method fails to work in any complex cell. More sophisticated methods include zone finding [6] and iterative use of singular value decomposition [7]. In general, most of these methods will produce multiple possible cells, however in most situations there will be one "best" cell to attempt first. There is no guarantee that this best cell is the correct one and it must be validated by a successful structure solution.

In addition to the dimensions of the unit cell, the symmetries elements or space group of the unit cell must be determined. The space group will consist of a series of symmetry operations and special positions. Special positions arise from when a symmetry operation maps a point onto itself. An example of such a special position would be a point on a mirror symmetry since that point

would be invariant under the mirror. In all there are 230 three-dimensional space groups, divided into eight classes: Cubic (all cell lengths are equal and all angles are 90°), Tetragonal (one unique cell length), Trigonal, Hexagonal (two unique cell lengths and γ is 120 °), Orthorhombic (three unique cell lengths), Monoclinic (three unique cell lengths and one angle is variable) and Triclinic. [8] Each particular space group corresponds to a series of reflection conditions or extinctions. For example in $P2_1$, reflections corresponding to $0k0$ with k odd are extinct (i.e. have zero intensity). Thus once the cell is determined, it is useful to look for patterns in the observed or unobserved peaks. This pattern (or space group choice) can be further confirmed by performing a Pawley fit, as will be described in the next section.

1.4 The Pawley Method

The Pawley method [9] is a method of whole pattern fitting, in which each peak intensity is considered an independent parameter and a least square approach is used to fit the measured diffraction pattern. Given a correct unit cell and a plausible peak shape model, the Pawley fit corresponds well with the measured pattern. As the first few peaks are generally well isolated, refined values for the unit cell and peak shape profile can be obtained. High order reflections are usually not well isolated and as such there is a correlation between their fit intensity; this correlation can also be useful and is utilized in a number of methods of structure determination. [10]

Additionally, this fitting procedure has been found to be particularly useful

in three regards:

1. Validation of a potential indexing or unit cell choice as a poor fit generally means an incorrect indexing

2. Identification of systematic absences in order to choose a space group as *hkl*s with zero intensity are easily identified in such a fit

3. The extraction of integrated intensities to be used in other methods (e.g. charge flipping)

1.5 Structure Determination

While many approaches and techniques exist for preliminary structure determination, [11, 12] simulated annealing and charge flipping are currently prevailing as two of the most successful and all compounds presented in this dissertation have been solved with one or both of these two methods.

1.5.1 Simulated Annealing

In most situations, there is more information known than just the atomic composition of the compound of interest, often including knowledge about the atomic bonding and molecular structure. Simulated annealing [13] takes advantage of this prior information in a global optimization process in which molecules are treated as rigid bodies. As such, it is important to keep the size of the search space manageable, so parameters such as bond lengths, lattice parameters, etc. are held constant. This allows for the reduction of the parameters needed to determine the structure from three per atom to six per

molecule (plus additional parameters for necessary internal degrees of freedom). As information about the molecular structure and other such details of the material is important, synthesis details of each compound in this dissertation will be included.

Under such a calculation, the molecules are placed at a random position, orientation and torsion angles of the rotatable bonds, which form a configuration space for the search. From this a powder pattern is calculated and a comparison is made with the experimental pattern with a corresponding goodness of fit, with the goal of minimizing this fit parameter. TOPAS Academic[14], the program that was utilized in this dissertation to implement simulated annealing, uses the weighted pattern R-factor,

$$R_{wp} = \sqrt{\frac{\sum_m w_m (Y_{o,m} - Y_{c,m})^2}{\sum_m w_m Y_{o,m}^2}}, \tag{1.6}$$

where m indexes the 2θ values in the powder diffraction pattern, and $Y_{o,m}$, $Y_{c,m}$, and w_m are the observed data, calculated model data and statistical weight of the m^{th} point in the pattern. A random step is then taken in this configuration space and a new goodness of fit is calculated. Depending on the complexity of the problem there may be a number of local minima. If only steps that improved the goodness of fit were taken, it would be very likely to get stuck in a local minimum corresponding to an incorrect solution. Thus it is necessary to sometimes take a step that may degrade the goodness of fit. The strategy of accepting or rejecting steps is as follows: if the new goodness of fit is better, then the step is accepted; if not, the step is taken with a probability equal to $\mathrm{e}^{\frac{-\Delta E}{T_{SA}}}$, where ΔE is the change in the goodness of fit parameter and

T_{SA} is the effective temperature, a parameter of the simulated annealing. With a sufficient effective temperature, the trial solution will be kicked out of local minima and thus be more likely to approach the global minima corresponding to the correct structure solution. This temperature will be varied over time (a cooling schedule) in order to settle on the global minima.

1.5.2 Charge Flipping

Charge flipping [15] takes the opposite approach of simulated annealing. Rather than building in as much prior knowledge as possible, charge flipping only assumes positivity (i.e. the charge density is positive everywhere) and that the correct structure factors should have magnitude that match with the measured pattern. The basic process of this algorithm oscillates between imposing these conditions in real space and reciprocal space.

First, the structure factor magnitudes are calculated from the integrated intensities from the Pawley fit. The starting phases, $\phi(\vec{h})$, are chosen randomly with the constraint that $\phi(-\vec{h}) = -\phi(\vec{h})$. These structure factors and phases, F, are then Fourier transformed into charge density, ρ. At this point the first contraint, positivity is applied. This is done by adjusting the charge density as follows:

$$\rho' = \begin{cases} \rho & \text{for } \rho > -\delta \\ -\rho & \text{for } \rho < -\delta \end{cases} \tag{1.7}$$

A small non-zero δ is necessary to allow for truncation errors of the Fourier transform due to finite resolution of the data. This new charge density ρ' is

then Fourier transformed back into reciprocal space to create new structure factor magnitudes and phases, G. The structure factor magnitudes are now set to be the measured magnitudes, while the new phases are kept. This process is then iterated (Equation 1.8) till convergence and a charge density map is produced.

$$\begin{array}{ccc} \rho & \xrightarrow{\text{positivity}} & \rho' \\ \mathrm{FFT}^{-1} \uparrow & & \downarrow \mathrm{FFT} \\ F & \leftarrow & G \end{array} \tag{1.8}$$

This method can be extremely useful as it is possible to discover unexpected features. As a downside, it often results in useless and sometimes even incorrect density maps and as such any such map needs further validation by a finalized and refined structure. The interpretation of the density map produced is nontrivial and sometimes only partial features can be recognized. As such, charge flipping is generally only part of the structural solution process and is often useful to help build a model for simulated annealing.

1.6 Rietveld Refinement

The final step of the structural solution process is Rietveld refinement. In this step, previously restrainted parameters (such as bond lengths and angles, thermal factors, peak shape) are released and allowed to vary. This process was developed by Rietveld in 1969 [16] and is based on fitting the whole diffraction pattern rather than just the integrated intensities. It is a least squares approach to refine the candidate structure in order to make the calculated

pattern as close to the measured pattern as possible. Specifically, it is the minimization of:

$$M = \sum_i W_i (y_i^{obs} - \frac{1}{c} y_i^{calc})^2 \tag{1.9}$$

where W_i is the statistical weight of each point; c is a scale factor; y_i^obs and y_i^{calc} are the measured and calculated intensity of point i, respectively. The calculated pattern can be determined from the current candidate structure from:

$$y_i^{\text{calc}} = \sum_k m_k L_k |F_k|^2 G(\Delta\theta_{jk}) + y_i^{\text{back}} \tag{1.10}$$

where s is a scale factor, L_k the Lorentz-polarization factor for reflection k, F_k the structure factor, m_k the multiplicity factor, $\Delta\theta_{ik} = 2\theta_i - 2\theta_k$ where $2\theta_k$ is the calculated position of reflection k, $G(\Delta\theta_{ik})$ is the shape function of the reflection, and y_i^{back} is the background contribution.

It is important to release as many as parameters as possible, as strange behavior of a parameter can be vital to a correct structural determination. Specifically, if a parameter gets larger or smaller than expected, it may mean that the candidate structure is incorrect in some manner. For example, in a compound containing an NO_2 group if the N-O bond gets very small, it may indicate that it is not actually an NO_2 group but perhaps a chlorine atom, as was the case in Co-SalenCl_2 (Chapter 5.1). Other possible errors may lead to returning to any of the previous steps to create a new indexing or candidate solution. If the refinement produces reasonable values and is stable upon small variations, the structure is considered finalized.

Chapter 2

The Power of Powder Diffraction

In this chapter of the dissertation, a number of structures will be presented which highlight the utility and ability of powder diffraction for structural determination across a wide range of materials: polymorphism, cocrystals, metal-organic frameworks, and magnetic compounds. Additionally each of these structures illustrate the state of art capabilities of powder diffraction as the structural determination was quite difficult, whether due to a large number of degree of freedoms or subtle disorders. Furthermore without the use of powder diffraction, none of these structures would be known.

2.1 Polymorphism: 3,4-Dinitrobenzoic Acid

The phenomenon of polymorphism, whereby a compound can crystallize into two or more distinct crystal structures, is both an intriguing problem in

Figure 2.1: Schematic Drawing of 3,4-Dinitrobenzoic Acid

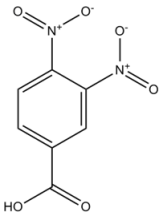

fundamental structural science, and a serious potential issue in the manufacture of materials whose physical properties may depend upon polymorphic form. [17] The crystal structure of a given sample may depend on such environmental parameters as temperature and pressure, as well as the history of the sample. There are numerous examples of metastable polymorphs which transform irreversibly into lower energy states, but it is not generally possible to guarantee that a given state is indeed the most stable. This highlights the importance not only to understand which polymorphic forms a given substance may have, but also the kinetic barriers that may govern transformations among them.

Polymorphism in 3,4-Dinitrobenzoic acid (Fig. 2.1) was originally investigated by Kuhnert-Brandsttter and Sollinger [18] with hot-stage microscopy, differential scanning calorimetry, and infared spectroscopy. In this original investigation, four forms were described: III formed upon crystallization from solvents at ambient temperature, II appeared when the sample is heated to 90-100 °C, I formed at 115-130 °C, and IV was sporadically observed, with a melting point of 122 °C. However, form IV could not be prepared reproducibly. It was found that transformations between III and II are reversible, but once formed, I did not revert to II or III. Form I melts at 164 °C. Zeller et al. has recently investigated this system as well and determined the structure of Form

III. [19] However there has been no crystallographic study reported of forms I and II of 3,4-Dinitrobenzoic acid.

The structure of form III is unexpectedly complex with four molecules in the asymmetric unit, Z' = 4, and this motivated an experiment to discover the structures of the other crystal forms to see if they were comparably complex. We believe that this complexity arises from the inability of the nitro groups to lay in the plane of the molecule, as they are close enough to interfere. In 2,4-, [20] 2,5- [21] and 3,5-Dinitrobenzoic Acid [22], the nitro groups do not interfere with each other and the resulting crystals structures are much less complicated (Z'=1).

3,4-Dinitrobenzoic acid was purchased from Acros Organics. Our collaborators at Ben-Gurion University of the Negev, Inna Barsky and Joel Bernstein, grew a single crystal of Form III and determined the structure through single crystal techniques. Single crystals were successfully obtained in the form of needles by slow evaporation from chloroform solution at room temperature. However they were not able to isolate a single crystal of the other forms. This led to an investigation of the system using powder diffraction in which we solved structures of Forms I and II. The single crystal Form III results are included here for comparison. [19]

2.1.1 Powder Diffraction

High resolution synchrotron X-ray powder diffraction patterns were collected at the X16C beamline at the National Synchrotron Light Source at

Figure 2.2: Rietveld fit of Form I. The points are the data, the solid line is the calculated pattern from the refinement and the difference between the two is shown below the main plot.

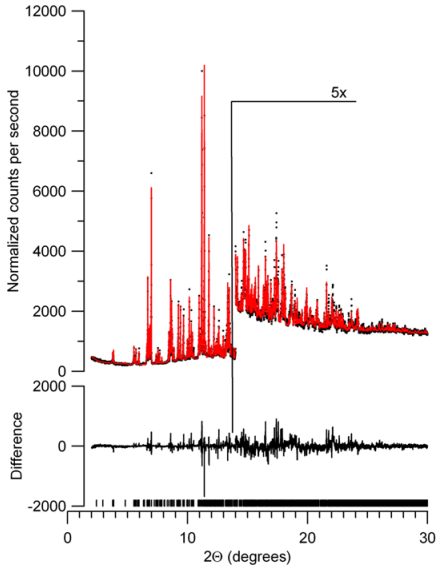

Brookhaven National Laboratory. The sample was flame sealed in a thin walled glass capillary of nominal diameter 1.0 mm, which was chosen since it is less fragile than a capillary of 1.5 mm and thus less likely to break upon heating. Heating was performed with in-house equipment and the temperature was monitored by a thermocouple positioned near to the sample.

Preliminary data was obtained with the sample and furnace rocking back and forth several degrees at each step in 2θ, but that gave unsatisfactory peak shapes due to grain growth in the sample leading to poor statistical averaging. Data taken from a capillary spinning at a few revolutions per second inside the sample heater was of much higher quality.

In order to achieve the middle temperature phase (form II), the sample was slowly heated past the first transition to 100 °C. However it was not possible to index this powder pattern, which indicated that it was not a single phase.

Figure 2.3: Rietveld fit of the mixture of 82.6% Form II and 17.4% Form I. It was not possible to isolate Form II. The points are the data, the solid line is the calculated pattern from the refinement and the difference between the two is shown below the main plot.

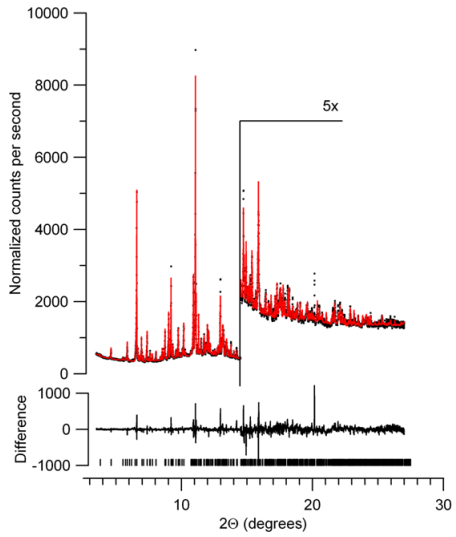

When cooled back to room temperature, the sample reverted back to form III and another phase, which was initially suspected to be form I. This indicates that the transition from form III to form II is reversible. Further heating of the sample to 135 °C caused the sample to transform into a single phase (form I), which remained after cooling back to room temperature.

As discussed below, the crystal structure of form I was determined from this room temperature sample. Interpolation of the form I lattice parameters between ambient temperature and 135 °C gave us a starting point to identify the form I peaks in the data set collected at 100 °C (Table 2.1), and subsequently index and solve the structure of form II. Form I remained stable for 3 months after measurement. This indicates that the transition from form II to I is irreversible.

The powder diffraction patterns of Form I and II were indexed using

Table 2.1: Unit cells of Form I at different temperatures

	Room T	100 °C	135 °C
a (Å)	7.4286(2)	7.4291(2)	7.4301(2)
b (Å)	13.8253(4)	13.9244(4)	13.9896(4)
c (Å)	16.8321(5)	16.9844(5)	17.0688(4)
α (°)	87.465(3)	87.459(3)	87.440(3)
β (°)	81.340(2)	81.215(2)	81.123(2)
γ (°)	80.157(2)	80.061(2)	80.034(2)
Volume (Å^3)	1688.3(2)	1709.9(2)	1726.2(2)

TOPAS Academic[14] to the cells listed in Table 2.2. In Form II, absence of peaks, $h0l$ with $h+l$ odd, suggested that the space group was $P2_1/n$. The fact that the volumes of all three forms were comparable suggested that they all had the same number of molecules in the unit cell. This would indicate for Form I and II, Z'=4 and Z'=2 inequivalent molecules respectively. Simulated annealing, implemented in TOPAS Academic, was used to solve the structure of both of these forms. Four independent molecules, each with three torsions, is a difficult problem for simulated annealing as that number of molecules implies 36 parameters to search over.

The result from simulated annealing was mostly reasonable but further modification of the positioning of the chemical groups on the rings was needed. After that modification a structure of reasonable packing and chemical significance was attained. Further refinements were done using TOPAS Academic using rigid bodies and then refining bond angles and lengths. H atoms were placed by geometric constraints and their position was not refined. Furthermore, all bonds of similar type were constrained to be equal and refined jointly and all angles around the aromatic ring were fixed to 120 degrees. The final

Table 2.2: Crystallographic Details of all three forms of 3,4-Dintrobenzoic Acid

	Form I	Form II	Form III
Space group	P-1	$P2_1/c$	P-1
a (Å)	7.4286(2)	7.5279(2)	7.4644(18)
b (Å)	13.8253(4)	17.3085(5)	13.274(3)
c (Å)	16.8321(5)	13.4644(4)	17.124(4)
α (°)	87.465(3)	90	89.480(4)
β (°)	81.340(2)	99.270(3)	88.248(5)
γ (°)	80.157(2)	90	84.593(5)
Volume (Å^3)	1683.5(2)	1731.5(2)	1688.3(2)
Z	8	8	8
Z'	4	2	4
Density (g/cm^3)	1.669		1.666
Density at 100°C (g/cm^3)		1.620	1.640
Temperature (°C)	25	100	25
R_{wp}	6.872	5.082	
R_{exp}	2.482	1.948	

refinements are shown in Figures 2.2 and 2.3. In the refinement of Form II, it was necessary to include the structure of Form I and perform a multi-phase Rietveld refinement, which resulted in the determination that the sample was formed of 82.6% Form II and 17.4% Form I. Crystallographic details are included in Table 2.2.

Atomic positions of forms I and II are tabulated in Appendix B.1.

2.1.2 Crystal Structures of 3,4-Dinitrobenzoic acid

All three of the structures consist of 3,4-Dinitrobenzoic acid dimers which are hydrogen bonded through their carboxylic acids. However, these dimers have a different orientation relative to each other and are not symmetry equivalent. When viewed along the a-axis (Figure 2.4), the three structures appear similar and are formed of dimer bilayers packed in herring bone

pattern. In order to understand the difference between these structures, two levels of comparison must be made: between the layers in the bilayer and between the bilayers themselves. In the first level of comparison (Figure 2.5), it can be observed that the layers slip relative to each other, but the layers inside a particular bilayer keep the same relative orientation. In Forms II and III, the bilayers are offset from each other. In the transition from II to I, one of the bilayers remains offset while the other bilayer is eclipsed. The next level of comparison involved the orientation of the different bilayers (Figure 2.6). In forms II and III, the different bilayers are orientated in the same direction. However in form I, one of the bilayers is rotated relative to the other bilayer and the two bilayers are orientated in opposite directions.

These differences in structure between the forms elucidate the sequence

Figure 2.4: View along a-axis. a: Form I b: Form II c: Form III

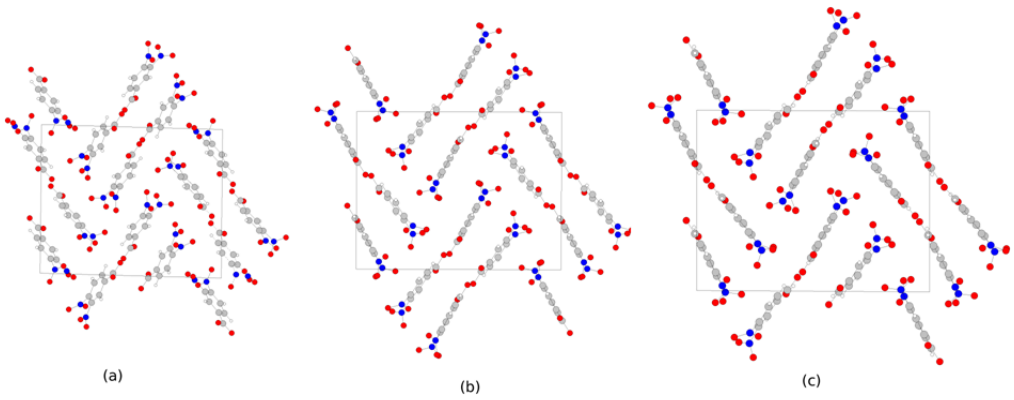

of transformation. The transition between form III and II consists of only sliding in the different bilayers. This motion of the molecules suggests that the kinetic barrier between these forms is relatively small and thus the sample can reversibly transform between these two states. However in the case of the transition between form II and I, the rotation of one bilayer relative to the

Figure 2.5: View perpendicular to the pair of dimers. Solid atoms are in the foreground. Hollow atoms are in the background. a: Form I; b: Form II; c: Form III. Forms I and III have two unique dimer pairs and thus two views are shown.

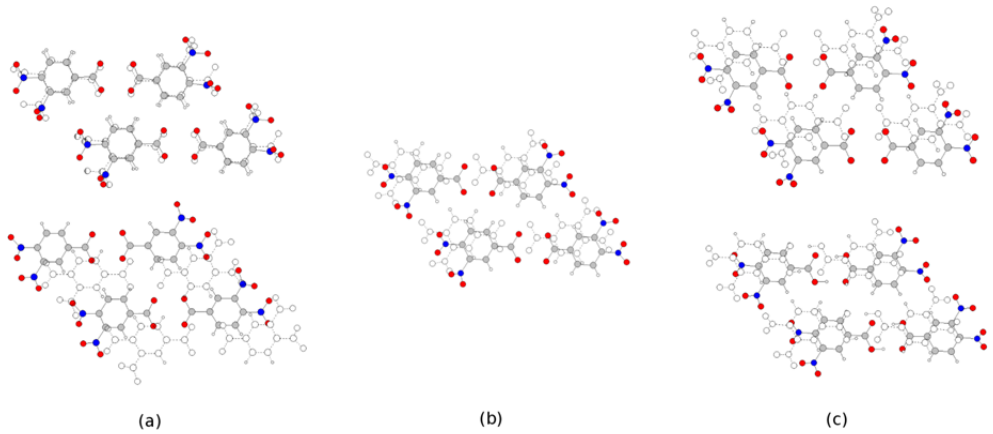

other has a large kinetic barrier, and thus the sample cannot transform directly from form III to I. Instead, form II acts as a metastable intermediate state that allows a transition from form III to form I, the energetically favored state.

Figure 2.6: View between the pair of bilayers. Solid atoms are from one bilayer. Hollow atoms are from the other bilayer. a: Form I; b: Form II; c: Form III.

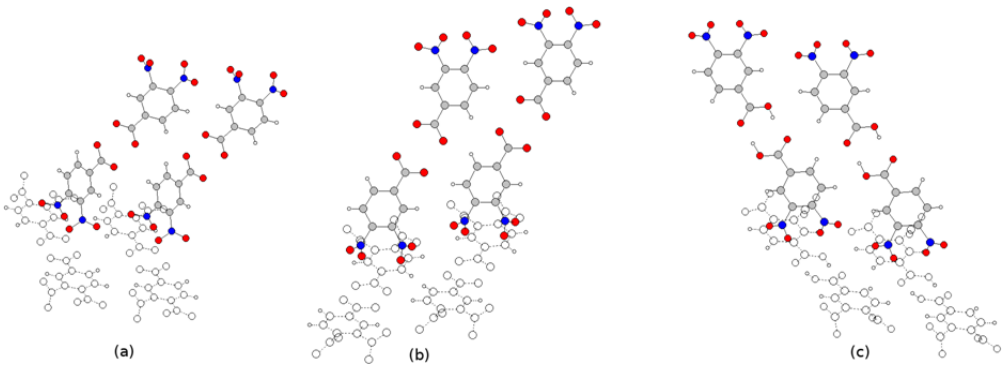

2.2 Cocrystals: *m*-Hydroxybenzoic Acid and Acridine (3:2)

While there is disagreement between leaders of the field over the exact definition [23–25], cocrystals may be defined as crystals that consist of two different organic molecules which are connected by hydrogen bonds. The current focus on these compounds is on the purposeful arrangement of these molecules into forming a hydrogen bonding network. This network will be constructed utilizing the idea that the best hydrogen donor will bond with the best hydrogen acceptor, the second best with the second best and so forth. It would then be possible to build up a particular crystal structure, i.e. crystal engineering. [26] One difficulty with this approach it is not always known how to rank different donors or acceptors. As such, there has been a large amount of research in creating different cocrystals in order to purposely construct such networks and further probe such rankings. There is additional interest in the pharmaceutical industry as different cocrystal may have different properties and open up new patentable areas. [27]

An additional complication arises when there are multiple donors or

Figure 2.7: Schematic Drawings of *m*-Hydroxybenzoic Acid and Acridine

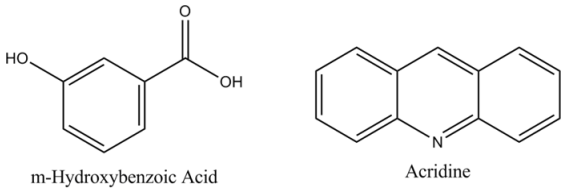

acceptors of similar ranking, as this competition is a possible source of polymorphism.[28] In order to further examine this class of polymorphism and the competition between different donors and acceptors, our collaborator, Daniel Admsond, created a series of cocrystals of Acridine and *m*-Hydroxybenzoic acid of different stoichiometries. Acridine was chosen since it has a strong hydrogen acceptor and is known to be polymorphic, with seven forms known currently. [29] With two hydrogen donors, *m*-Hydroxybenzoic acid will highlight the competition between different hydrogen bonding motifs.

A number of cocrystals were successfully created with different stoichiometries. Single crystals of two different 1:1 cocrystals and a 1:2 cocrystal were grown by using different solvents and characterized by single crystal diffraction. However, single crystals of a 3:2 stoichiometry could not be grown and as such only a powder was available.

2.2.1 Sample Preparation

The sample was prepared by our collaborator, Daniel Adsmond, at Ferris State University. It was made by slow evaporation of 1:1 solution of *m*-Hydroxybenzoic acid and Acridine in a 1:4 mixture of Acetone/Chlorobenzene.

2.2.2 Powder X-ray Diffraction

Figure 2.8: Rietveld fit of the 3:2 *m*-Hydroxybenzoic Acid and Acridine cocrystal. The points are the data, the solid line is the calculated pattern from the refinement and the difference between the two is shown below the main plot.

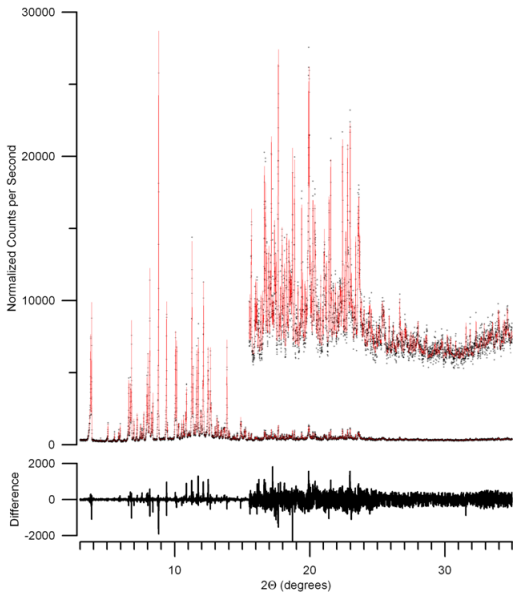

High resolution synchrotron X-ray powder diffraction patterns were collected at the X16C beamline at the National Synchrotron Light Source at Brookhaven National Laboratory.

This diffraction pattern was indexed, using TOPAS Academic[14], to a monoclinic cell with lattice parameters given in Table 2.3. From the systematic absences in the pattern, a tentative space group of $P2_1$ was assigned. Using the fact that each non-hydrogen atom occupies approximately 17 Å^3, this volume suggests $\frac{1891}{2\times17} = 56$ atoms in the asymmetric unit and thus a stoichiometry of either 4:1 or 3:2 (3-hydroxybenzoic acid to acridine). Since $P2_1$ does not have any special positions, this indicates 5 independent molecules

Table 2.3: Crystallographic details for *m*-Hydroxybenzoic Acid and Acridine (3:2)

Space group	$P2_1$
a (Å)	12.3776(4)
b (Å)	21.1632(6)
c (Å)	7.5011(2)
$\beta(^\circ)$	105.683(3)
V (Å^3)	1891.76
Z	2
$\lambda(\mathring{A})$	0.69990(3)
R_{wp}	7.28
R_{exp}	2.95

and thus at least 30 degrees of freedom to determine.

Both possible stoichiometries were modeled with rigid bodies and used in simulated annealing. During this process, the position of the hydroxy group was modified by hand in order to help guide the simulated annealing to the correct solution. Only the 3:2 stoichiometry gave a reasonable fit to the data and produced a preliminary structure. The position of the acridine was determined however the orientation (i.e. where the nitrogen atom was) needed to be modified in order to give a reasonable bonding arrangement of OH-N rather than OH-C. This candidate structure was then successfully Rietveld refined to a R_{wp} of 7.278% (Figure 2.8). Atomic positions are tabulated in Appendix B.2.

Figure 2.9: The *m*-Hydroxybenzoic acid ring that forms the building block of the structure of 3:2 *m*-Hydroxybenzoic Acid and Acridine cocrystal. Hydrogen bonds are shown as dashed blue and red lines.

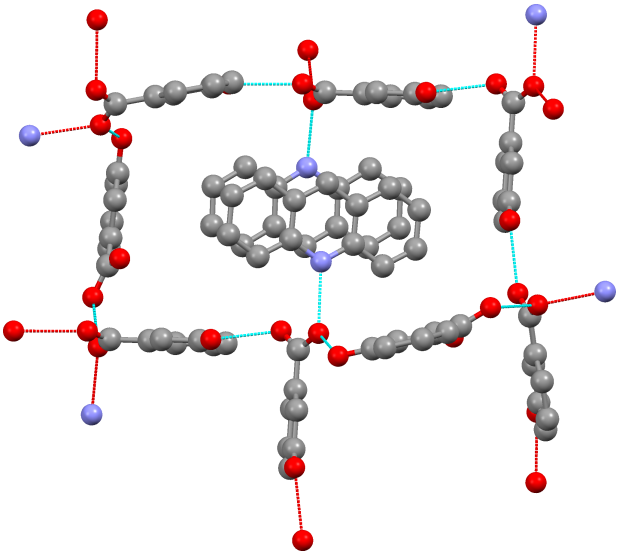

Figure 2.10: The buckled plane that is formed by edge-sharing rings that composes the structure of the 3:2 *m*-Hydroxybenzoic Acid and Acridine cocrystal. Hydrogen bonds are shown as dashed blue and red lines.

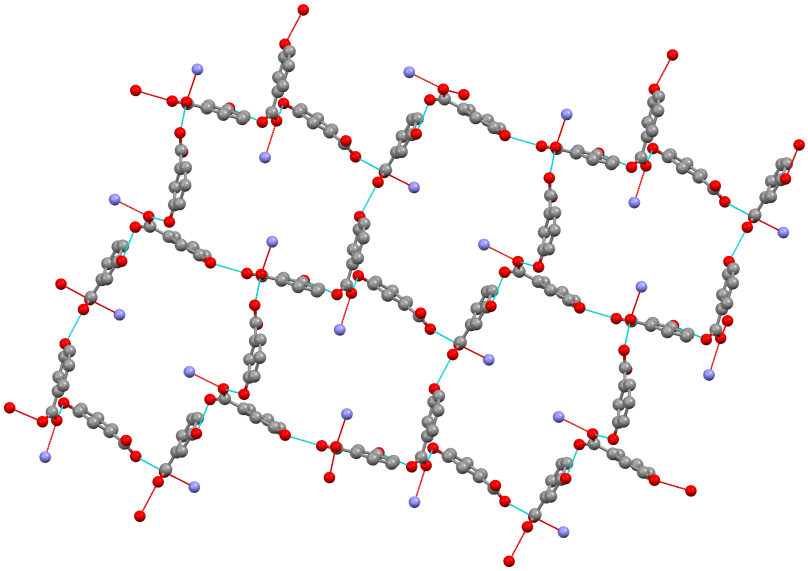

2.2.3 Crystal structure of m-Hydroxybenzoic Acid and Acridine (3:2)

The structure consists of three symmetry inequivalent m-Hydroxybenzoic acids and two Acridine molecules. While the hydrogens are not observed directly, hydrogen bonds can be inferred by the donor-acceptor distances and the structure can be understood by considering the network that results from this hydrogen bonding. Eight of the Hydroxybenzoic acids hydrogen bond in order to form a ring, which has two Acridine molecules occupying the center. (Figure 2.9) These rings are connected edgewise to form a buckled plane. (Figure 2.10) These planes are terminated by Acridine molecules and the average interplanar distance is ~ 7.5 Å.

2.3 Metal Organic Frameworks: $Cd_{0.5}[Cp^*Ru(\eta^6\text{-isophthalate})]$

A common problem encountered with single crystals is their inability to remain intact during a phase transformation. In this section, phase transformation upon dehydration of a metal-organic framework will be investigated. Metal-organic frameworks are systems that consist of metals coordinate by organic ligands to form frameworks with large void spaces. They are of particular interest as the void spaces can be used for hydrogen storage [30] or carbon dioxide sequestration. [31] As such, it is of vital importance to understand the structural behavior of these systems upon loading and unloading of these void spaces. The following section will investigate phase transformations upon de-

hydration of the metal organic framework, $Cd_{0.5}$[Cp*Ru(η^6-isophthalate)]. The ligand Cp*Ru(η^6-isophthalate) is shown in Figure 2.11.

Figure 2.11: Schematic showing the ligand Cp*Ru(η^6-isophthalate)

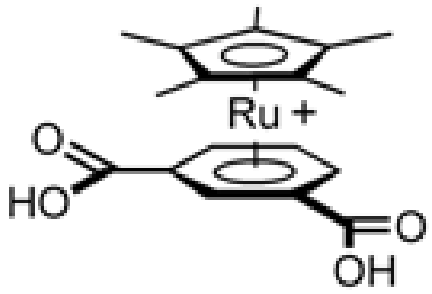

2.3.1 Sample Preparation and Single Crystal Diffraction

The fully hydrated $Cd_{0.5}$[Cp*Ru(η^6-isophthalate)] was prepared by our collaborators, Robert Fairchild and K. Travis Hollmann, at Georgetown University. When 1:1 DMF:H_2O solutions of Cp*Ru(η^6-isophthalate)Cl (8 mM) and $Cd(NO_3)_2$ (16 mM) were combined and heated at 45°C for several days, pale yellow crystals were generated. Single crystal X-ray diffraction was performed and a composition of $Cd_{0.5}$[Cp*Ru(η^6-isophthalate)] $3H_2O$ was found. [32] The fully hydrated compound is included for comparison with the other hydration states.

2.3.2 Gas Sorption Analysis

In order to investigate the hydration properties of $Cd_{0.5}$[Cp*Ru(η^6-isophthalate)], H_2O gas sorption was performed after desolvation at 120 °C

Figure 2.12: Sorption isotherms for $Cd_{0.5}(Cp^*Ru(\eta^6\text{-isophthalate}))$ after desolvation under reduced pressure at 120 °C with H_2O adsorption (closed circle) and H_2O desorption (open circle). Figure is reprinted from Robert Fairchild's Thesis. [32]

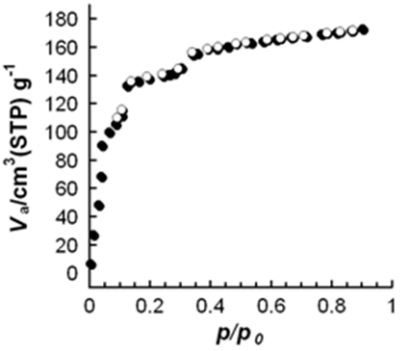

(Figure 2.12) by Robert Fairchild with the help of Takashi Uemura, Daisuke Tanaka, and Hirotoshi Sakamoto at Kyoto University, Japan. The H_2O sorption isotherm exhibits type I behavior, [33] which is indicative of adsorption of the water into pores which are not much larger than the molecular diameter of the water. Additionally, the isotherm shows at least one plateau indicating the possibility of an intermediate hydration state.

2.3.3 Synchrotron X-Ray Powder Diffraction

The dehyrated and partial hydrate phase were prepared by heating the fully hydrated phase under vacuum and measuring variations in the vacuum pressure, that would arise from release of water molecules from the compound. High resolution synchrotron X-ray powder diffraction patterns were collected at the X16C beamline at the National Synchrotron Light Source at Brookhaven National Laboratory.

Table 2.4: Crystal Data of the Three Hydration states of $Cd_{0.5}$[Cp*Ru(η^6-isophthalate)]

	Hydrated	Partial Hydration	Dehydrated
Space group	$P2_12_12$	$P2_1$	Cc
a (Å)	14.1363(8)	16.1925(5)	25.8232(7)
b (Å)	14.5997(8)	15.2904(5)	20.7513(4)
c (Å)	9.5699(5)	16.3424(5)	16.1005(5)
β (°)	90	118.225(4)	126.537(4)
Volume (Å^3)	1975.09	3565.11	6932.12
Z	4	8	16
Z'	1	4	4
Density (g/cm^3)	1.70	1.73	1.75
R_{wp}		8.577	5.155
R_{exp}		5.623	2.165

Dehydrated Phase

This diffraction pattern was indexed, using TOPAS Academic[14], to a monoclinic cell with possible space groups Cc or $C2/c$. (Table 2.4) The fact that the hydrated phase was in a non-centrosymmetric space group $P2_12_12$ suggested to attempt structure solution in Cc first. The volume of the dehydrated phase, 6932.12 Å^3, suggested that there were 16 formula units in the cell and thus 4 symmetry inequivalent units, particularly 2 Cd ions and 4 Cp*Ru(η^6-isophthalate) ligands. This produces a large number of degrees of freedom, specifically three for each Cd ion and 6+1 per ligand (the additional degree of freedom is from a torsion of the Cp* relative to the η^6-isophthalate), resulting in 34 degrees of freedom. This is quite a task for simulated annealing or any method of structural determination. There is an additional piece of information known that is that the ligand must end up coordinating with the metal and additionally must form a layered structure, similar to the fully

Figure 2.13: Rietveld fit of the fully dehydrated $Cd_{0.5}$[Cp*Ru(η^6-isophthalate)]. The points are the data, the solid line is the calculated pattern from the refinement and the difference between the two is shown below the main plot.

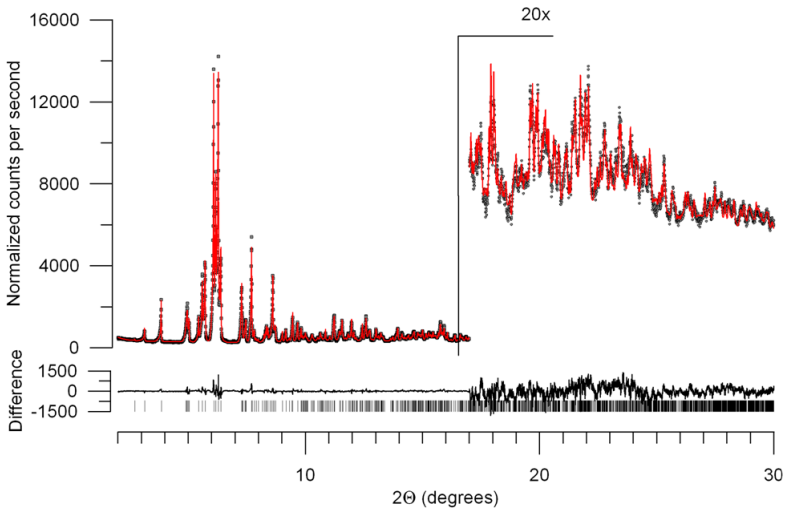

hydrated phase.

Simulated annealing was performed and the intermediate structures were monitored. When a ligand appeared to be correctly coordinated to the metal, the metal and ligand were fixed and simulated annealing was continued. Additionally, if needed, the ligand would be rotated by hand in order to properly coordinate to additional metals. The process was continued with releasing and fixing metals and ligands, for approximately a week, until a preliminary structure was determined.

This preliminary structure was then successfully Rietveld refined, where similar bond lengths and angles (e.g. Ru-C, C-C, etc.) fixed and refined jointly. (Figure 2.13) It is of importance to note that this structure does not contain any additional symmetries that would allow a representation in $C2/c$. [34]

Partial Hydrate Phase

Figure 2.14: Rietveld fit of the partially dehydrated $Cd_{0.5}$[Cp*Ru(η^6-isophthalate)] . Sample consists of a mixture of the fully hydrated and partially dehydrated forms. The points are the data, the solid line is the calculated pattern from the refinement and the difference between the two is shown below the main plot.

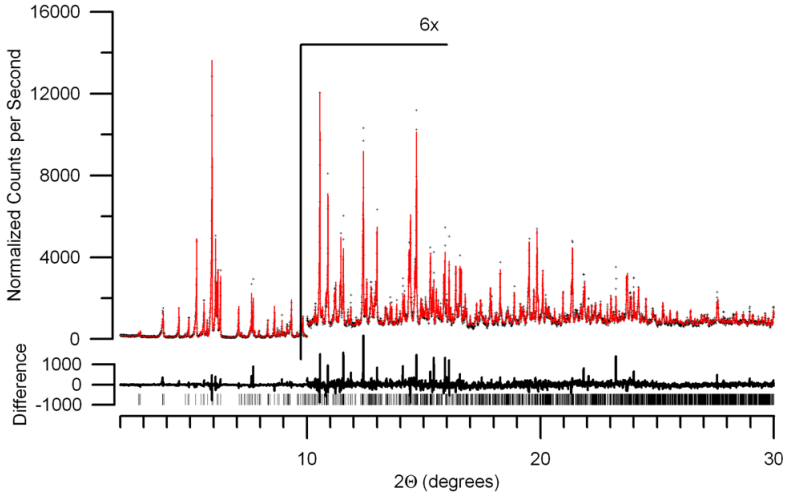

The diffraction pattern could not be indexed by including all peaks. By inspection, it became clear that there was an amount of fully hydrated phase present. Disregarding those peaks, the diffraction pattern was indexed, using TOPAS Academic[14], to a monoclinic cell with space group $P2_1$. Once again, the volume of this phase suggested four symmetry inequivalent units. The structure was solved with simulated annealing following a similar procedure as outlined for the dehydrated phase. This preliminary structure was then successfully Rietveld refined, where similar bond lengths and angles (e.g. Ru-C, C-C, etc.) were fixed and refined jointly. (Figure 2.14)

Atomic positions of all three hydration states are tabulated in Appendix B.3.

Figure 2.15: Crystal structure of different hydration states of $Cd_{0.5}$[Cp*Ru(η^6-isophthalate)] a) fully hydrated b) partial hydrate c) fully dehydrated. Left is a view perpendicular to the 2D layers. Right is a view along the layer. The blue dashed line is the corresponding unit cell.

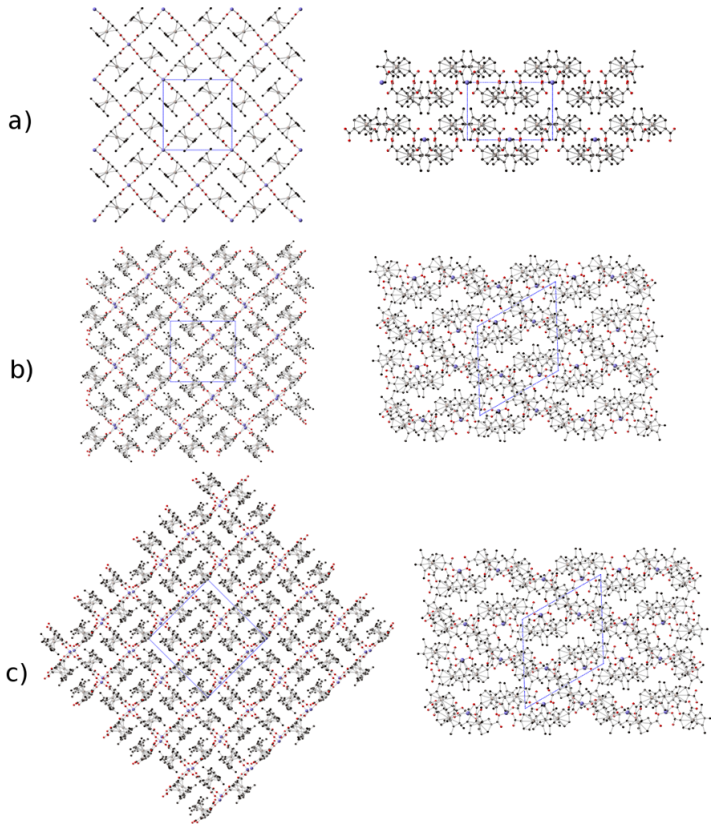

2.3.4 Crystal Structure of the Different Hydration States of $Cd_{0.5}$[Cp*Ru(η^6-isophthalate)]

All three hydration states consist of 2D layered structures (Figure 2.15). Upon dehydration, the Cp*Ru(η^6-isophthalate) ligands rotate in order to reduce void space. Additionally this distortion causes changes in the coordination of the Cd ion; specifically the ligand goes from chelating (both oxygens in the hydroxy group coordinated to the Cd ion) to monodentate (only one oxygen coordinate to the Cd ion).

2.4 Disordered Magnetic Compounds: $K_4V(NCS)_6$

Structural disorder in a compound can lead to difficulty in the determination of the structure. This arises from the fact that a list of atomic positions is not sufficient to understand the structure. Rather, the atomic positions must be interpreted into a picture that fits with chemical information. $K_4V(NCS)_6$ presents a rather extreme example of this, which presented a large effort in order to determine and interpret the structure.

2.4.1 Synthesis

$K_4V(NCS)_6$ was synthesized by our collaborators, Endrit Shurdha and Joel Miller, at the University of Utah. VSO_4 (300 mg, 2.04 mmol) was suspended in 20 mL of acetone. KSCN (397 mg, 4.08 mmol) was also dissolved in 5 mL of acetone and added quickly to the yellow vanadium sulfate mixture. An immediate tan precipitate forms and the solution turns dark orange. The solution was stirred overnight. The brown mixture was filtered through Celite to remove the precipitate. The solution was taken to dryness and redissolved in acetone (Yield 200 mg, 53%).

2.4.2 Structure Determination of $K_4V(NCS)_6$

High resolution synchrotron X-ray powder diffraction patterns were collected at the X16C beamline at the National Synchrotron Light Source at Brookhaven National Laboratory. Using TOPAS-Academic [14], the powder

Figure 2.16: The charge density map of $K_4V(NCS)_6$ produced by charge flipping, as visualized in VESTA [35]

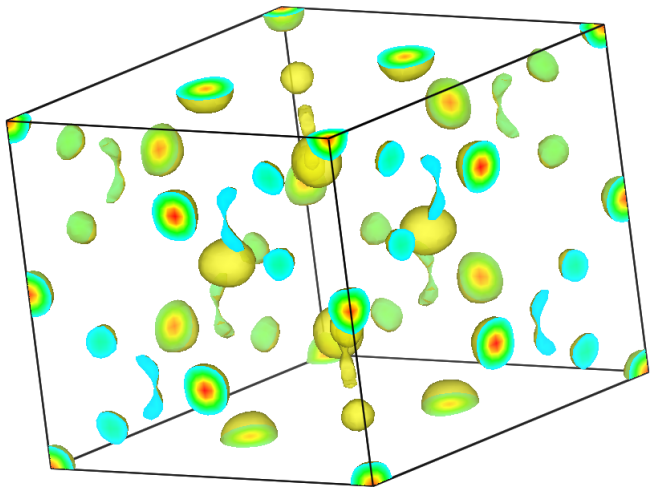

diffraction pattern was successfully indexed to a hexagonal cell (Table 2.5).

It is often useful to gain information from other techniques and sources, as this will help with the building of sufficient and correct models for the structural solution. In this case, there was additional information from the IR absorption spectroscopy, which was performed by our collaborators, Endrit Shurdha and Joel Miller. Free NCS^- has exhibits a ν_{NCS} at 2054 cm^{-1}, and two δ_{NCS} bending modes at 486 and 471 cm^{-1}. Upon binding to a metal ion the δ_{NCS} doublet typically becomes a singlet and shifts to lower frequency (480 cm^{-1}) for M-N, and lower for M-S bond (420 cm^{-1})].[36] When thiocyanate bridges two metal centers ($\mu_{1,3}$-NCS^-) two δ_{NCS} absorptions for both M-N and M-S are present. Absorptions assignable to terminal, nonbridging ν_{CN} (2115 cm^{-1}), noncoordinated ν_{CO} (1705 cm^{-1}), and δ_{NCS} for M-N (479 cm^{-1}) are present, but a low frequency δ_{NCS} for assignable to the M-S absorption is not present. Hence, $[V^{II}(NCS)_6]^{4-}$ is proposed to be present.

Figure 2.17: A view of the preliminary structure of $K_4V(NCS)_6$ produced from charge flipping.

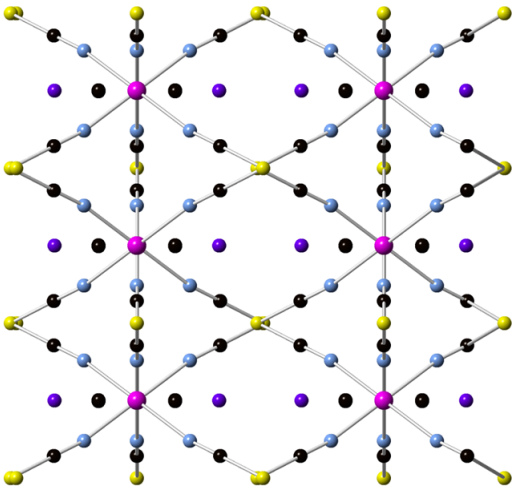

Figure 2.18: A zoomed in view on the NCS motif, showing that implausible bonding in the preliminary structure produced from charge flipping.

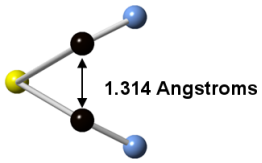

Charge flipping, as implemented in Superflip [37], was performed. (Figure 2.16) Using the density map that was provided by charge flipping, it was possible to identify the highest density atomic sites; One of these sites was 6-coordinated and the other was 2-coordinated. Since V^{II} prefers to be 6-coordinated, it was possible to identify the vanadium and sulfur sites. Furthermore, it was possible to place potential places for the K, C and N. However this potential structure has a fundamental problem, as the C-C distance would be 1.314 Å, which would create an impossible bonding geometry. (Figures 2.17 and 2.18) Additionally, the ∠C-S-C angle would be 48.15°, which is also implausible. As mentioned in the first chapter of this dissertation, implausibility

Figure 2.19: The honeycomb lattice formed by the K and S atoms. (a) view along the c-axis (b) view along the a-axis.

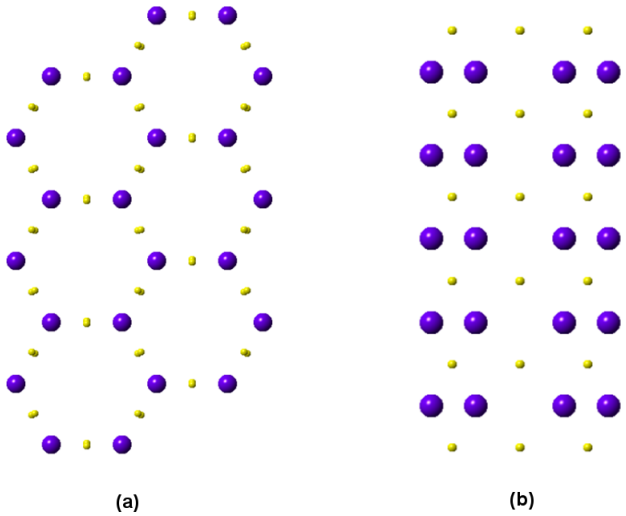

in the preliminary structures often means that there was incorrect prior information built into the structure solution process. In charge flipping, the only prior information used is the lattice, which indicated the possibility that the indexing needed to be repeated. However, this belief impeded understanding the truth of what was going on and the determination of the actual structure. Indexing was repeated many times and no reasonable alternate lattices were produced.

After a long period of time, it was realized that the cause of this implausibly close carbon atoms is from disorder, or rather that each carbon, nitrogen and vanadium is half occupied and thus the two carbon atoms are not actually that close to each other. This disorder can be understood by constructing the two hypothetical order phases and then considering the actual structure as a superposition of these two hypothetical phases.

The first step of building up the ordered structure is only considering the

Figure 2.20: A diagram illustrating the two different ways $V(NC)_6$ can be connected into the KS-honeycomb lattice resulting in the two hypothetical ordered phases.

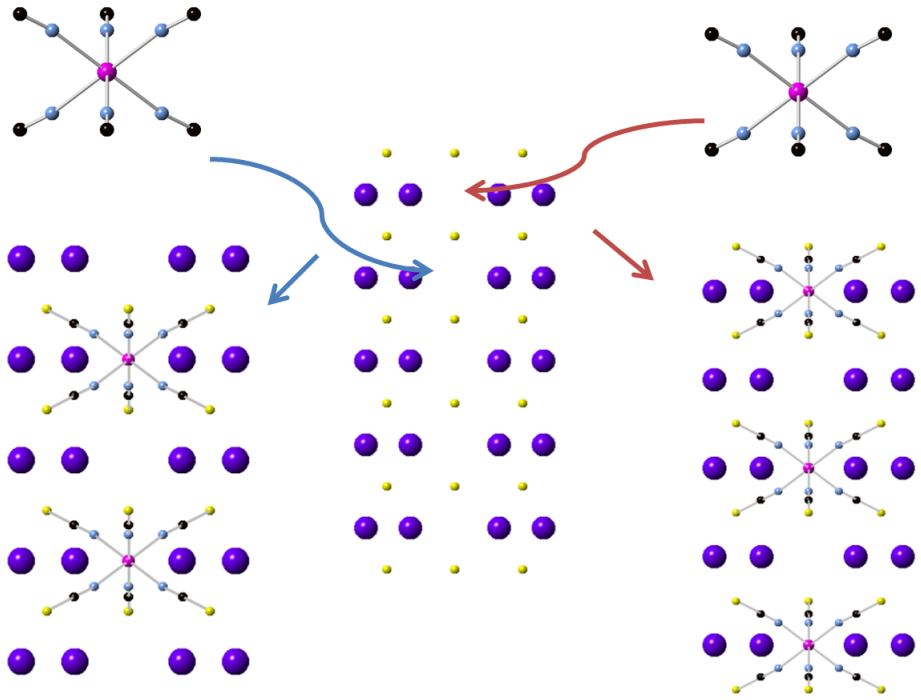

K and S atoms in the preliminary structure, which form a honeycomb lattice. (Figure 2.19). As mentioned previously, IR adsorption spectroscopy leads us to believe $[V^{II}(NCS)_6]^{4-}$ is present. In order to create $[V^{II}(NCS)_6]^{4-}$, $V(NC)_6$ needs to be connected to the S atom. There are two ways to place the V atom at 0,0,0 or 0,0,$\frac{1}{2}$ as demonstrated in Figure 2.20. In between each $[V^{II}(NCS)_6]$ is a disordered acetone; the disorder of the acetone arises from mismatch between the acetone molecule and the symmetry of the site. The actual structure exists as a superposition of the two ordered phases (Figure 2.21). Additionally, a Ni version of this compound has been made that is isostructural. Atomic positions are tabulated in Appendix B.4.

This compound presented a unique challenge as the disorder created a

Figure 2.21: Left and right show ordered $V(NCS)_6$ chains. Center shows the superposition of the two ordered version into the true disorder structure with red atoms representing the choice of order demonstrated on the right and blue atoms representing the choice on the left. Acetone has not been shown for clarity.

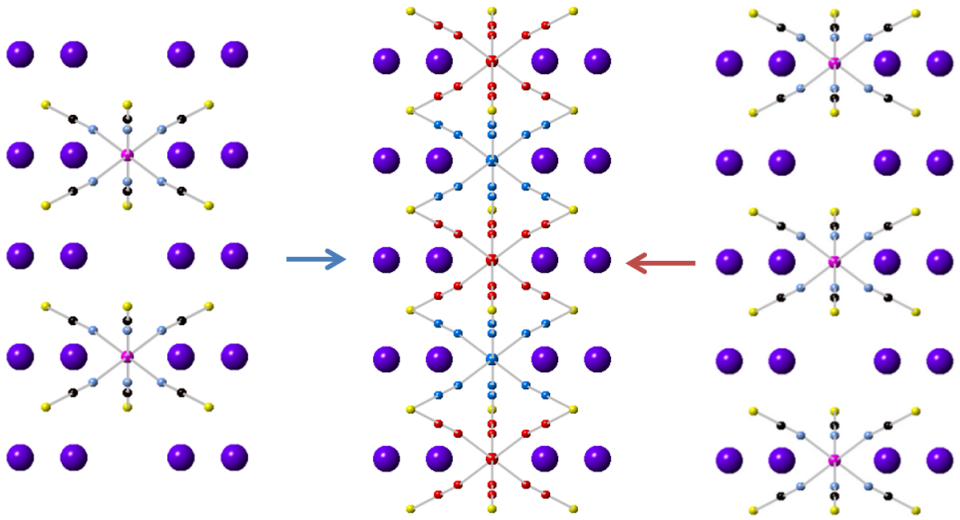

situation where the interpretation of the results of charge flipping was exceptionally difficult. More so, it illustrates that atomic positions are not sufficient to have structural understanding of a compound, but rather a deeper understanding which matches with a plausible chemical structure is necessary.

Figure 2.22: View along the c-axis of the structure of $K_4V(NCS)_6$. Acetone has not been shown for clarity.

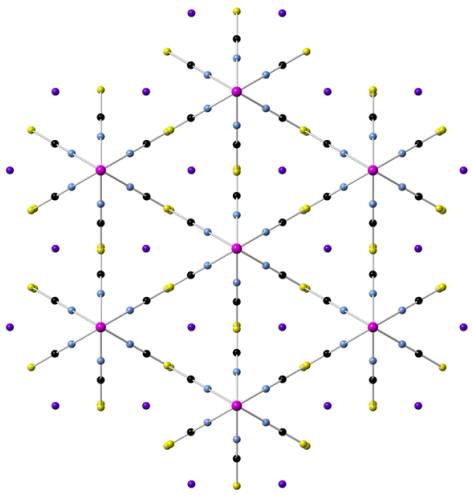

Table 2.5: Crystallographic details for $K_4V(NCS)_6$)

Space group	$P6_3/mcm$
a (Å)	8.4583(3)
b (Å)	8.4583(3)
c (Å)	9.1933(3)
$\alpha(^\circ)$	90
$\beta(^\circ)$	90
$\gamma(^\circ)$	120
V (Å^3)	569.60
$\lambda(\AA)$	0.69730(3)
R_{wp}	6.39
R_{exp}	2.52

Chapter 3

Coordination Compounds Containing Pyrazine

Coordination polymers are materials that utilize an organic ligand in order to connect metal ions into a framework, which can have a one-, two-, or three-dimensional topology of covalent bonds. The choice of an appropriate ligand allows control over the separation and coordination of metal ions depending on the symmetry of the ligand used. This ordering will in turn have a direct effect on the physical properties of the compound. Particularly, there is a large interest in the magnetic behavior of these materials, as these ligands will assist in spin exchange between the metal ions.

This chapter of the dissertation will focus on coordination polymers that use pyrazine as the ligand. Pyrazine will often form $M^{II}(pyz)_2^{2+}$ layers, where M is a transition metal and pyz=pyrazine, and as such will allow some rational design of the desired compound. (Figure 3.1) Additionally, as the pyrazine is a small molecule, this will allow for shorter metal-metal contacts and thus a

Figure 3.1: A schematic drawing of a $M^{II}(pyz)_2^{2+}$ layer

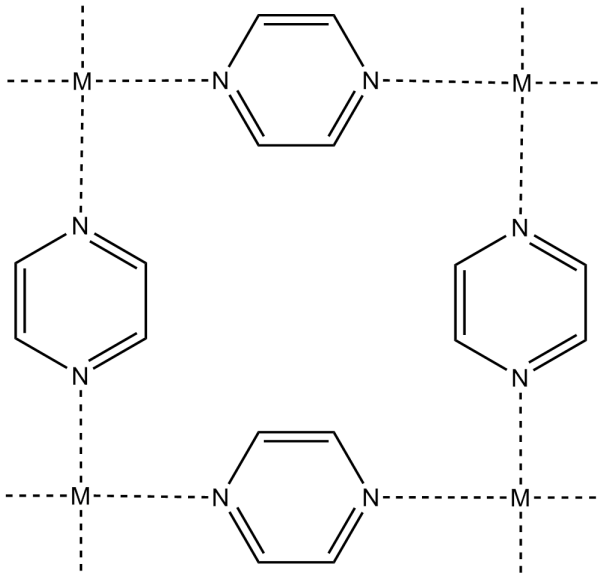

stronger magnetic coupling compared to larger ligands.

3.1 $[Ni(HF_2)(pyz)_2]X$ (X= SbF_6 or PF_6)

The HF_2^- ion has one of the strongest known hydrogen bonds with an experimentally measured bond enthalpy of 163 kJ/mol. [38] One possible approach to probe the ability of the HF_2^- ion to act as a magnetic exchange mediator between paramagnetic metal ions is to use utilize the HF_2^- ion to connect $M^{II}(pyz)_2^{2+}$ layers. The first attempt along these lines was from the creation of the coordination polymer, $Cu(HF_2)(pyz)_2]BF_4$. [39] Its structure consists of six-coordinated Cu atoms, which are linked in two dimensions by pyrazines to form a 2D framework in the a-b plane. The bifluoride ion bridges these layers along the c-axis to yield a three-dimensional network with BF_4^- ions occupying the interstitial space. The magnetic susceptibility of this compound was found to fit well with a spin-1/2 Heisenberg square lattice antiferromagnet. This 2-D magnetism arises from the the Cu-pyz-Cu bonding network made up of the Cu $d_{x^2-y^2}$ orbitals and pyrazine lone-pair p_z orbitals. There was only a weak interaction between these 2D square lattices, since the F $2p_z$ orbital does not overlap with the orbital of Cu. Similar compounds were made with different counter ions (SbF_6[40] and PF_6[41]) and exhibit similar magnetic behavior.

Unfortunately, these systems were not a successful probe of the bifluoride as a mediator of spin exchange; rather what was desired was a system that allows the σ-orbitals of the HF_2^- to overlap with an appropriate metal magnetic orbital. A candidate metal for such a system is Ni^{II}, since it has two magnetically active orbitals, $d_{x^2-y^2}$ and d_{z^2}. If Ni^{II} was to form a 3D solid similar to the above-mentioned $[Cu(HF_2)(pyz)_2]X$ systems, both the pyrazine and bifluoride spin exchange pathways would be important to the magnetism

of the system. In this section of the dissertation, two such compounds will be presented which contain the desired combination of Ni-FHF-Ni and Ni-pyz-Ni spin mediation.

3.1.1 Synthesis

The following synthesis was performed by our collaborator, Jamie Manson, at Eastern Washington University. All chemicals were ACS reagent grade and used as received from commercial sources. Following a general procedure, pale blue powders of $[Ni(HF_2)(pyz)_2]PF_6$ (**3.1**)and $Ni(HF_2)(pyz)_2]SbF_6$ (**3.2**) were isolated in high yield (>80%) upon slow evaporation of the solvent for several days. The products were thoroughly washed with small amounts of H_2O, then Et_2O, and dried in vacuo for 6 h. **3.1** was prepared by mixing a 5-mL aqueous suspension of $NiCO_3$ (0.4003 g, 3.37 mmol) with 2 equiv of HPF_6 (60% by weight in H_2O). The resulting $Ni(PF_6)_2$ solution was stirred and added to a 3-mL aqueous solution containing NH_4HF_2 (0.1923 g, 3.37 mmol) and pyrazine (0.5401 g, 6.74 mmol) to yield a green solution. This solution was then allowed to evaporate at room temperature in order to produce a pale blue powder.

For **3.2**, NiF_24H_2O (0.6010 g, 3.56 mmol) was dissolved in 5 mL of aqueous HF (48% by weight in H_2O) and slowly mixed with a 3-mL aqueous HF solution that contained NH_4HF_2 (0.2030 g, 3.56 mmol), pyrazine (0.5705 g, 7.11 mmol), and $NaSbF_6$ (0.9211 g, 3.56 mmol) to afford a green solution. This solution was then allowed to evaporate at room temperature in order to produce a pale blue powder.

3.1.2 Synchrotron X-Ray Powder Diffraction

High-resolution powder diffraction patterns were collected on beamline X16C located at the National Synchrotron Light Source, Brookhaven National Laboratory. Measurements were made at 17 and 298 K. The sample was brought to 17 K by an in-house cryostat. The capillary was either rocked by a few degrees or spun at several Hz during data collection to improve particle statistics. TOPAS-Academic[14] was used to index both **3.1** and **3.2**. The space groups $C2/c$ and $P4/nmm$ were hypothesized for **3.1** and **3.2**, respectively, by checking the systematic absences of Pawley whole pattern fits. No impurities appeared to be present in either pattern. Details of the unit cell are provided in Table 3.1 and Table 3.2.

The crystal structure of **3.2** was determined by charge flipping, as implemented in Superflip [37]. The density map provided by charge flipping was sufficient to locate all non-hydrogen atoms and create a preliminary structure. The data from this sample was of sufficient quality that there was not a need to place restriction on bond lengths and angles and thus this preliminary structure was refined as independent atoms. (Figure 3.2B) Atomic positions are tabulated in Appendix B.5.

The powder pattern of **3.1** was not of sufficient quality for charge flipping (i.e. the sample does not diffract to a low enough d-spacing/high enough angle), so instead model building and simulated annealing had to be performed. The first clue, in determining the structure of **3.1**, is that both the a and b unit cell lengths of **3.1** and **3.2** are very similar. In **3.2**, $[Ni^{II}(pyz)_2]^{2+}$ layers are formed in the a-b plane and thus the similarity

suggests that **3.1** also has $[Ni^{II}(pyz)_2]^{2+}$ layers. If the suggested formula of $[Ni(HF_2)(pyz)_2]PF_6$ is correct, the volume of the unit cell only allows for four Ni atoms per unit cell. Since $C2/c$ has a general position with multiplicity eight, this implies that the Ni must be on a special position. Placing a nickel atom on an inversion site (Wycoff site b), nearest Ni-Ni distances can be measured and this provides the next clue into determining the structure. Examining the structure of **3.2** (Table 3.2), it can be seen that the Ni-FHF-Ni and Ni-pyz-Ni distances are on the order of 6.4 and 7 Angstroms, respectively. From these distances, it is now possible to place the pyrazine and FHF^- molecules and create the 3-D framework of the structure. The final step is placing the counterion, PF_6^-, in the large interstitial space remaining. This preliminary structure was successfully Rietveld refined (Figure 3.2A), which confirmed this as a finalized structure. In this refinement, bond lengths and angles of a similar nature (i.e. aromatic, N-C, P-F bonds) were refined jointly to a single value. Atomic positions are tabulated in Appendix B.5.

3.1.3 Structure of $[Ni(HF_2)(pyz)_2]PF_6$

The atomic labeling scheme is shown in Figure 3.3A. $[Ni(HF_2)(pyz)_2]PF_6$ (**3.1**) has monoclinic ($C2/c$) symmetry at room temperature, in contrast to the Cu analog which is tetragonal ($P4/nmm$). The Ni^{II} ion is on an inversion center while P1, F2, F4, and H5 are on 2-fold rotation axes. One unique Ni site exists which is coordinated to four pyrazines, with two unique N atoms, at an average distance of 2.15 Å, which extend into a $[Ni^{II}(pyz)_2]^{2+}$ planes.

Table 3.1: Crystallographic details for $[Ni(HF_2)(pyz)_2]PF_6$ (**3.1**).

Temperature(K)	17	298
Empirical Formula	$C_8H_9N_4F_8PNi$	$C_8H_9N_4F_8PNi$
Formula Weight (g/mol)	402.85	402.85
Space Group	$C2/c$	$C2/c$
a (Å)	9.9322(3)	9.9481(3)
b (Å)	9.9066(3)	9.9421(3)
c (Å)	12.4803(5)	12.5953(4)
β (°)	80.531(3)	81.610(3)
V (Å^3)	1211.26(7)	1232.4(7)
Z	4	4
ρ_{calc}(g/cm^3)	2.209	2.171
λ	0.7000(2)	0.6993(2)
R_{wp}	6.065	6.485
R_{exp}	4.111	4.930

Table 3.2: Crystallographic details for $[Ni(HF_2)(pyz)_2]SbF_6$ (**3.2**).

Temperature (K)	17	298
Empirical Formula	$C_8H_9N_4F_8SbNi$	$C_8H_9N_4F_8SbNi$
Formula Weight (g/mol)	493.64	493.64
Space Group	$P4/nmm$	$P4/nmm$
a (Å)	9.8965(3)	9.9359(3)
b (Å)	9.8965(3)	9.9359(3)
c (Å)	6.4329(2)	6.4471(2)
V (Å^3)	630.04(3)	636.47(3)
Z	2	2
ρ_{calc}(g/cm^3)	2.603	2.577
λ	0.7000(2)	0.6993(2)
R_{wp}	8.850	7.351
R_{exp}	4.092	3.715

Figure 3.2: Synchrotron X-ray powder diffraction data obtained at 298 K for: (A) $[Ni(HF_2)(pyz)_2]PF_6$ (**3.1**) and (B) $[Ni(HF_2)(pyz)_2]SbF_6$ (**3.2**). Black symbols and red lines represent the experimental data and Rietveld fit, respectively. The solid black line at the bottom of each graph is the difference between the observed and calculated patterns.

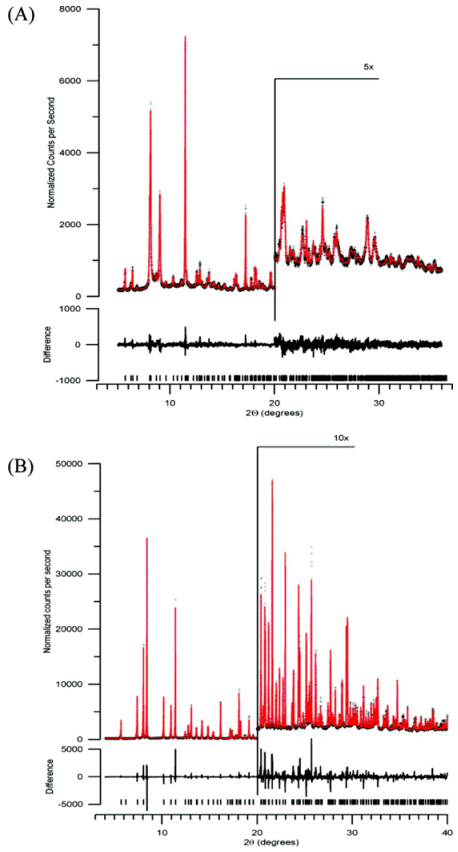

(Figure 3.4A) The octahedral coordination is completed by the FHF molecule along the axial positions with Ni1-F5 bond lengths of 2.02 Å. Symmetry about the Ni(II) center requires that N1-Ni1-N1, N2-Ni1-N2, and F5-Ni1-F5 bond angles be 180°. The NiN_4F_2 coordination displays a slight rhombic distortion, with N1-Ni1-N2, N1-Ni1-F5, and N2-Ni1-F5 bond angles of 90.6, 89.4, and 93.3°, respectively. The Ni-FHF-Ni angle in **3.1** is significantly bent at an angle of 157°, due to sliding of the $Ni(pyz)_2$ planes. The PF_6 ions occupy

Figure 3.3: Asymmetric units and atom labeling schemes for (A) $[Ni(HF_2)(pyz)_2]PF_6$ (**3.1**) and (B) $[Ni(HF_2)(pyz)_2]SbF_6$ (**3.2**).

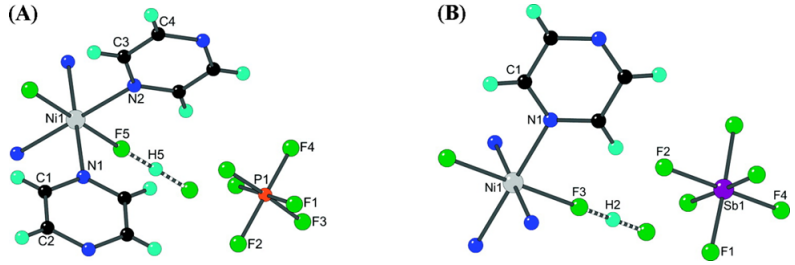

Figure 3.4: View of the $[Ni(pyz)_2]^{2+}$ layers observed in (A) $[Ni(HF_2)(pyz)_2]PF_6$ (**3.1**) and (B) $[Ni(HF_2)(pyz)_2]SbF_6$ (**3.2**) normal to the layer direction. Counterions and pyrazine H atoms have been omitted for clarity.

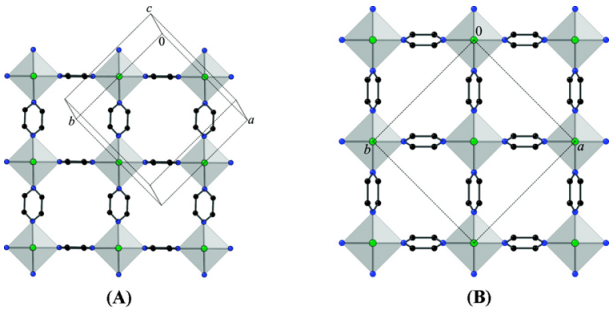

the interstitial space of the framework as shown in Figure 3.5A. Along two of the three unit cell axis, the PF_6^- molecules are aligned uniformly and share the same orientation; however, they alternately stagger along the *c*-axis. The octahedral PF_6 ion is somewhat distorted and contains four different P-F bond lengths that range between 1.56 and 1.63 Å. The F-P-F bond angles are also distorted.

3.1.4 Structure of $[Ni(HF_2)(pyz)_2]SbF_6$

Figure 3.3B provides the atom labeling scheme for **3.2**. Compound **3.2** is isomorphic with $[Cu(HF_2)(pyz)_2]SbF_6$ [40] with the Ni and H2 atoms oc-

Figure 3.5: Polyhedral representations of the 3D coordination polymers: (A) $[Ni(HF_2)(pyz)_2]PF_6$ (**3.1**) and (B) $[Ni(HF_2)(pyz)_2]SbF_6$ (**3.2**). NiN_4F_2 and XF_6^- octahedra are colored gray and orange (X = P) or purple (X = Sb), respectively. Pyrazine H atoms are not shown.

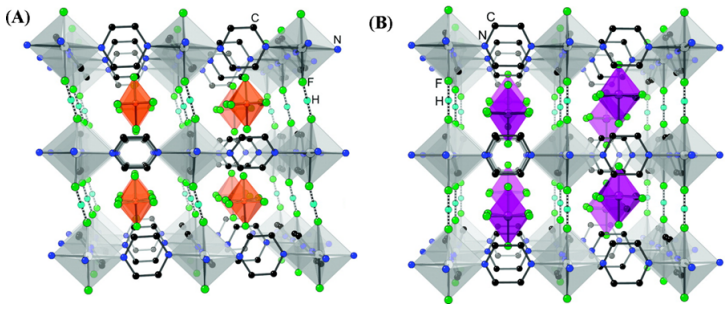

cupying $\bar{4}2m$ symmetry sites while Sb1, F2, and F4 have 4mm symmetry. The NiN_4F_2 octahedra consists of four equivalent N atoms in the equatorial plane [Ni1-N1 = 2.12 Å] and two axial F3 at a slightly shorter distance of 2.10 Å. The difference between the Ni-F and Ni-N bond lengths is 1.1% and is a weaker distortion of the NiN_4F_2 octahedron as compared to a 14.1% difference observed in $[Cu(HF_2)(pyz)_2]SbF_6$. [40] The NiN_4F_2 octahedron in **3.2** is axially compressed whereas an elongation was observed in $[Cu(HF_2)(pyz)_2]SbF_6$. The difference between the axial and equatorial bond lengths is 7%, which is much smaller than that found in **3.1**. The extended structure of **3.2** is that of a 3D coordination polymer where Ni atoms are linked in two dimensions by pyrazine ligands to form 2D $[Ni^{II}(pyz)_2]^{2+}$ square layers in the *ab*-plane (Figure 3.4B). Bifluoride ligands bridge the layers together along the *c*-axis to form a network as shown in Figure 3.5B. The Ni-pyz-Ni and Ni-FHF-Ni distances are 7.03 and 6.45 Å, respectively. The SbF_6^- counterions in **3.2** occupy the interstitial spaces within the framework.

Table 3.3: Selected bond lengths (Å) and bond angles (°) for $[Ni(HF_2)(pyz)_2]PF_6$ (**3.1**).

Bond length or angle	T = 17 K	T = 298 K
Ni1-F5	1.984(4)	2.024(4)
Ni1-N1	2.1860(5)	2.150(4)
Ni1-N2	2.2007(4)	2.152(4)
P1-F1	1.641(5)	1.587(6)
P1-F2	1.747(9)	1.625(8)
P1-F4	1.600(9)	1.615(5)
C1-N1	1.366(2)	1.357(2)
C1-C2	1.399(3)	1.347(3)
Ni1-F5-H5	152	157
F5-Ni1-N1	87.6(3)	90.6(2)
F5-Ni1-N2	93.6(2)	93.3(3)
N1-Ni1-N1	180	180
N1-Ni1-N2	90.6(2)	89.4(2)
F5-Ni1-F5	180	180
F1-P1-F2	91.2(2)	89.5(2)
F1-P1-F3	83.7(2)	86.7(3)
F2-P1-F3	89.3(2)	88.7(2)
N1-C1-C2	117.4(1)	120.7(2)
C3-N2-C4	125.1(6)7	118.5(3)

Table 3.4: Selected bond lengths (Å) and bond angles (°) for $[Ni(HF_2)(pyz)_2]SbF_6$ (**3.2**).

Bond length or angle	T = 17 K	T = 298 K
Ni1-F3	2.066(5)	2.099(3)
Ni1-N1	2.097(3)	2.123(2)
F3-H2	1.150	1.130
Sb1-F1	1.891(3)	1.897(2)
Sb1-F2	1.866(7)	1.890(5)
Sb1-F4	1.881(7)	1.845(5)
C1-N1	1.339(4)	1.331(3)
C1-C1A	1.402(4)	1.403(5)
Ni1-F3-H2	180	180
F3-Ni1-N1	90	90
F3-Ni1-F3A	180	180
N1-Ni1-N1	180	180
F1-Sb-F2	89.1(1)	88.9(1)
F1-Sb-F4	90.9(1)	91.2(1)
F2-Sb-F4	180	180
N1-C1-C1A	121.6(3)	121.1(2)
C1-N1-C1A	116.8(3)	117.8(2)

3.1.5 Magnetic Susceptibility of $[Ni(HF_2)(pyz)_2]PF_6$ and $[Ni(HF_2)(pyz)_2]SbF_6$

Measurements of the magnetic susceptibility were performed by our collaborators, Jamie Manson and Paul Goddard. [42] Figure 3.6 shows the magnetic susceptibility, χ, versus temperature for **3.1**. χ reaches a maximum at 7.4 K, which suggests antiferromagnetism. [43] χT and $1/\chi$, Figure 3.7 also indicate antiferromagnetism. $1/\chi$ was well fit by the Curie-Weiss equation with Landé g-factor and Weiss constant (θ) of 2.043(1) and -12.5(1) K, respectively. The negative θ value is also indicative of antiferromagnetism.

Figure 3.6: Magnetic susceptibility, χ for $Ni(HF_2)(pyz)_2]PF_6$ (**3.1**).[42]

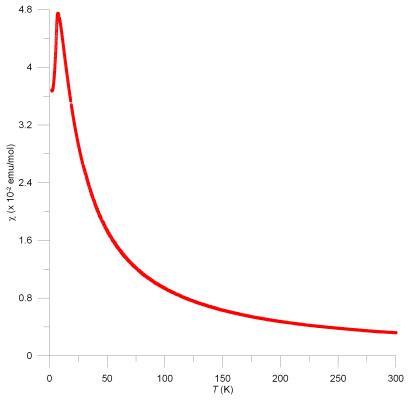

3.2 reaches a maximum at 15 K, which is a much larger temperature than observed for **3.1**. $1/\chi$ vs T (Figure 3.9) was fit to the Curie-Weiss equation with parameters Landé g-factor and a Weiss constant (θ) with values of 2.081(1) and -21.42(2) K, respectively. Similarly with **3.1**, the negative value of the Weiss constant indicates antiferromagnetic interaction between the Ni^{II} ions. Comparing the magnetic plots for **3.1** and **3.2**, it can easily be seen that

Figure 3.7: χ T and $1/\chi$ for **3.1**. The green line is a fit of $1/\chi$ to the Curie-Weiss equation. [42]

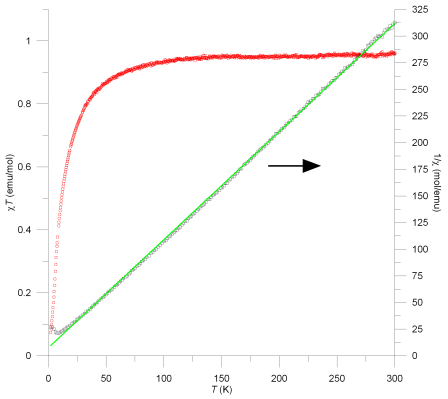

Figure 3.8: Magnetic susceptibility data (red open circles) for polycrystalline $Ni(HF_2)(pyz)_2]SbF_6$ (**3.2**).[42]

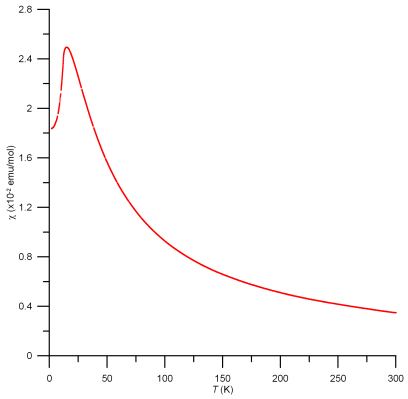

3.2 is similar magnetically to **3.1**, but exhibits a stronger antiferromagnetic interaction.

This difference in coupling can be understood by the difference in the structures of **3.1** and **3.2**, specifically the bent Ni-FHF-Ni angle present in **3.1**. As illustrated in Figure 3.10, the Ni-FHF-Ni spin exchange path consists of stronger σ-overlap between the Ni d_{z^2} and the F sp orbitals of FHF^- for the linear Ni-HFH-Ni in **3.2** than for the bent Ni-HFH-Ni in **3.1** such that the Ni-FHF-Ni spin exchange should be stronger for **3.2**.

Figure 3.9: χ T and $1/\chi$ vs T plots for **3.2**. The green line is a fit of $1/\chi$ to the Curie-Weiss equation. [42]

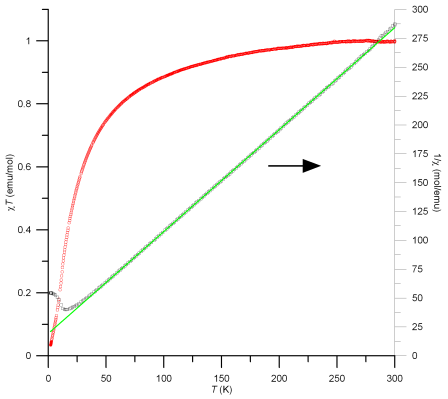

Figure 3.10: Schematic diagrams illustrating the orbitals involved in the Ni-FHF-Ni and Ni-pyz-Ni spin exchange paths of **3.1** and **3.2**. This figure is reprinted from Ref [42].

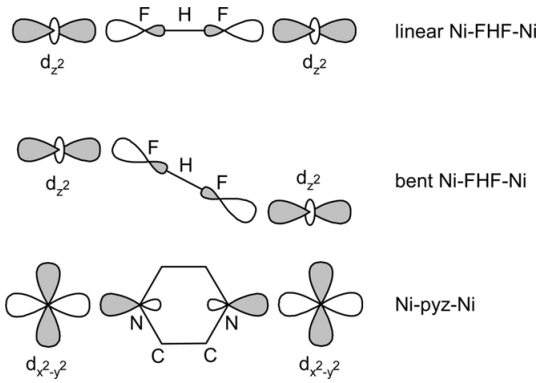

3.2 Polymorphism in $[Ni(HF_2)(pyz)_2]$ PF_6

When our collaborator, Jamie Manson, attempted to a find a new synthesis route in order to have the ability to scale up the synthesis for neutron measurements, a second polymorph of $[Ni(HF_2)(pyz)_2]$ PF_6 was discovered. The primary structural difference between α- and β-PF_6 polymorphs is Ni-FHF-Ni angle. This allows further examination of the geometric influence of HF_2^- on the magnetism of the system.

3.2.1 Synthesis

The following synthesis was performed by our collaborators, Kimberly Carreiro and Jamie Manson, at Eastern Washington University. In a typical synthesis of β-PF_6(**3.3**), NiF_24H_2O (6.02 mmol, 1.0165 g) was dissolved in 5 mL of 48% HF(aq) and added to a 5-mL HF(aq) solution containing KPF_6 (6.02 mmol, 1.1087 g), NH_4HF_2 (6.03 mmol, 0.3439 g) and pyrazine (12.2 mmol, 0.9783 g) which resulted in a clear green solution. Upon slow evaporation at room temperature for a few weeks, a pale blue powder was obtained in high yield (>75 %). The solid was collected via vacuum filtration, dried in vacuo, washed with H_2O, filtered, and finally vacuum dried for ∼3 hrs.

3.2.2 Structure Determination

High-resolution synchrotron X-ray powder diffraction patterns were collected at several temperatures on the X12A and X16C beamlines at the National Synchrotron Light Source at Brookhaven National Laboratory. Indexing of the 295 K diffraction pattern resulted in a tetragonal lattice. Using **3.2** as a preliminary structural model, the structure of **3.3** was successfully refined. (Figure 3.11) Atomic positions are tabulated in Appendix B.5.

3.2.3 Crystal Structure of β-$[Ni(HF_2)(pyz)_2]PF_6$

Table 3.5 compares various structural parameters for both polymorphs. **3.3** has a tetragonal space group $P4/nmm$ with a unit cell comparable to those of $[Ni(HF_2)(pyz)_2]SbF_6$ **3.2**. Similar to **3.1** and **3.2**, Ni^{II} ions are cooridinated by four pyrazines to form 2D $[Ni^{II}(pyz)_2]^{2+}$ square layers. Bifluoride ions join

Figure 3.11: Synchrotron X-ray powder diffraction data obtained at room temperature of β-[Ni(HF_2)(pyz)$_2$]PF_6 (**3.3**). Black symbols and red lines represent the experimental data and Rietveld fit, respectively. The solid black line at the bottom of each graph is the difference between the observed and calculated patterns.

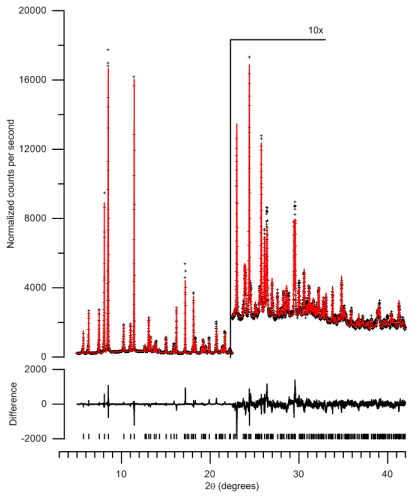

the planes together along the c-axis to form a 3D network. The intralayer Ni-pyz-Ni and interchain Ni-FHF-Ni separations are nearly identical between the α and β-phases. The PF_6^- anions occupy interstitial spaces within the framework. Importantly, the Ni-F-H bond angle is 180° in β-PF_6 which differs greatly from the the 157° angle in **3.1**.

3.2.4 Phase Transition of β-[Ni(HF_2)(pyz)$_2$]PF_6

Upon cooling, β-PF6 undergoes a phase transformation near 200 K with a large range of coexistance between the high and low temperature phases. (Figure 3.13) The resulting pattern (Figure 3.14) has not yet been indexed and from this we speculate that this low-T phase may be incommensurate and perhaps characterized by some stacking disorder. Upon warming, the sample

Figure 3.12: Crystal structure of β-[Ni(HF_2)(pyz)$_2$]PF_6 (**3.3**) (T = 295 K). Gray, blue, green, black, orange, and cyan spheres represent Ni, N, F, C, P, and H2 atoms, respectively. Pyrazine hydrogen atoms have been omitted for clarity. Dashed cylinders delineate H2-F3 hydrogen bonds.

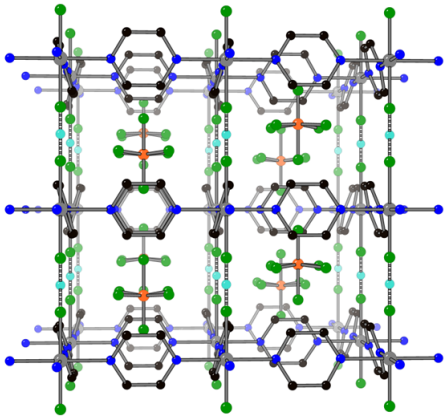

Figure 3.13: A selected region of the diffraction patterns of **3.3** at different temperatures: 295K (Black), 245 K (Blue), 215K (Green), 180K (Cyan), 140K (Magenta), 90K (Yellow)

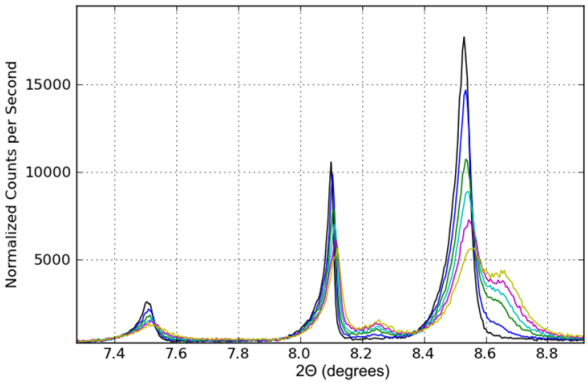

reverts back to the high temperature phase. This suggests that the Ni-FHF-Ni segment may still be linear in the low temperature phase. Future experiments that will take advantage of Pair Distribution Function analysis, [44] which is sensitive to local structural features, are planned in order to determine if the local structure does not change upon cooling. It is currently believed that the

Table 3.5: Comparison of key structural (T = 295 K) for α- (**3.1**) and β-$[Ni(HF_2)(pyz)_2]PF_6$ (**3.3**).

Polymorph	α	β
Crystal system	monoclinic	tetragonal
Space group	$C2/c$	$P4/nmm$
a (Å)	9.9481(3)	9.9197(3)
b (Å)	9.9421(3)	9.9197(3)
c (Å)	12.5953(4)	6.3434(2)
β (°)	81.610(3)	90
V (Å^3)	1232.4(7)	624.19(3)
Z	4	2
Ni-F (Å)	2.024(4)	2.067(3)
Ni-N (Å)	2.151(4)	2.111(2)
FF (Å)	2.38	2.22
FHF (°)	180	180
Ni-FH (°)	157	180
Pyrazine tilt angle (°)	53.1, 88.5	72.6

Figure 3.14: Powder diffraction pattern of **3.3** at 80K.

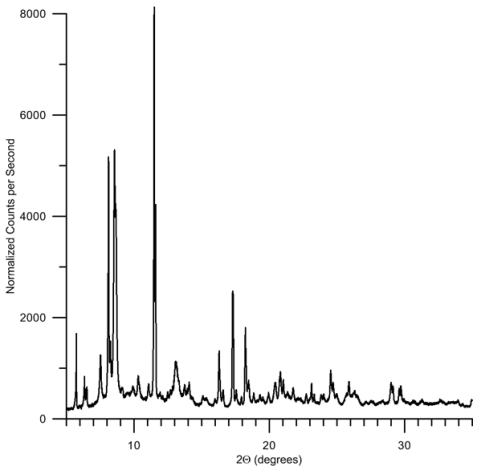

network of covalent bonds does not vary, as this phase transition is reversible. Additionally the ability to determine Ni-Ni distances may lead to insight into the nature of the stacking faults.

3.2.5 Magnetic Behavior of β-$[Ni(HF_2)(pyz)_2]PF_6$

Measurements of the magnetic susceptibility were performed by our collaborators, Jamie Manson and Paul Goddard. [45]

Figure 3.15: Comparison of χ vs T data for both polymorphic forms of $[Ni(HF_2)(pyz)_2]PF_6$. This figure is reprinted from Ref [45].

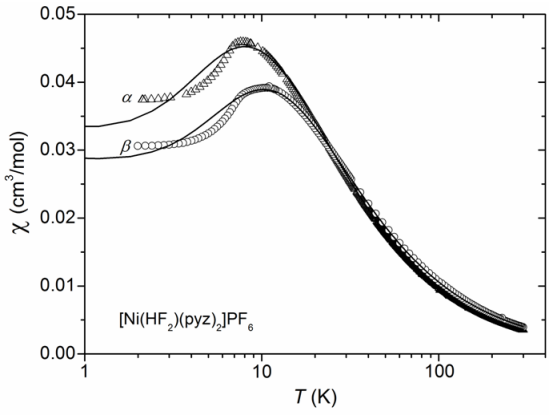

Similar to **3.1** and **3.2**, the shape of maximum at 10.1 K is indicative of antiferromagnetic interactions. T_{max} of 10.1 K is substanially higher than the temperature observed for **3.1** (Figure 3.15). This difference between the magnetic coupling between **3.1** and **3.3**, similarly to the difference between **3.1** and **3.2**, can be understood by difference in the Ni-FHF-Ni angle and as such the understanding of the structure was critical in the interpretation of the magnetic data.

3.3 $NiF(pyz)_{1.5}(H_2O)_2$ TaF_6: An attempt at $[Ni(HF_2)(pyz)_2]TaF_6$

A common way to alter a structure is to replace the counterion with a smaller or larger counterion which can result in different distortions of the framework, which can be used to probe different features, such HF_2^- ability to mediate spin exchange. A simple example of this is the replacement of SbF_6 for the smaller PF_6 in **3.1**, which resulted in the distortion of the framework from tetragonal to monoclinic. In this section, we will discuss the replacement of SbF_6 for the larger TaF_6. However, a possible issue with this replacement with a larger counterion is that the framework cannot distort sufficiently and instead forms an unexpected new structure.

3.3.1 Synthesis

The following synthesis was performed by our collaborators, Hope Tran and Jamie Manson, at Eastern Washington University. NiF_2 (0.350 g) was dissolved in 5 mL of 50% aqueous-HF in a plastic beaker. A second solution containing NH_4HF_2 (0.118 g), TaF_5 (0.572 g), and pyrazine (0.332 g) was prepared from 5 mL of 50% aqueous-HF and the NiF_2 solution slowly added while stirring. A pale green solution was obtained. The reaction mixture was covered with parafilm, small holes poked in the top, and the solvent allowed to slowly evaporate at room temperature. A light blue microcrystalline solid precipitated upon slow evaporation of the solvent for several weeks. The solid was collected via suction filtration yielding 64 mg of product (**3.4**).

3.3.2 Structure Determination

A powder of **3.4** was individually flame-sealed in thin-walled glass capillary tubes and high-resolution powder diffraction patterns collected on beamline X16C located at the National Synchrotron Light Source, Brookhaven National Laboratory. TOPAS-Academic was used to index **3.4**. By checking for systematic absences of a Pawley fit, the space group of $C2$ or $C2/m$ was assigned. Details of the unit cell are provided in Table 3.6. From the dimensions of the unit cell and the dissimilarity with the unit cells of **3.1** and **3.2**, it seemed unlikely that the composition of the sample was $[Ni(HF_2)(pyz)_2]$ TaF_6 and as such solving of this structure of this compound presented a particular difficulty. Some information can be gained from the space group as molecular frameworks that form in $C2$ or $C2/m$ tend to be two dimensional rather than three dimensional; however this is a tendency and not a requirement.[46]

Charge flipping, as implemented in Superflip [37], was performed on **3.4**. The density map, provided by charge flipping, was not sufficient to identify the structure, however it was possible to identify the heavy atoms (i.e. Ni and Ta). (Figure 3.16) There appeared to be two unique heavy atoms and it was possible to assign one site to Ni and the other to Ta from the differences in charge density of the two sites.

After assigning the Ni atom to the position indicated from the charge density map, nearest Ni-Ni distances can be measured and this provides

Figure 3.16: The charge density map of **3.4**, produced by charge flipping in Superflip [37], as visualized in VESTA. [35] Isosurface levels have been turned up to isolate only the heavy atoms. The smaller charge was assigned to Ni and the larger to Ta.

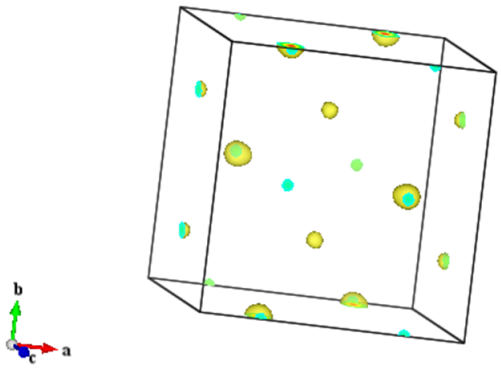

the next clue into determining the structure. As mentioned previously, Ni-FHF-Ni and Ni-pyz-Ni distances are on the order of 6.4 and 7 Angstroms, respectively. From this two separate pyrazine molecules can be placed which then form a 2-D $Ni(pyz)_2^{2+}$ framework. However there are no Ni-Ni distances corresponding to the usual Ni-FHF-Ni distance, which implies the lack of FHF^- in the compound. After placing the pyrazine molecules, the Ni atom is only 3 coordinated, which is highly unlikely. Since Ni^{II} is most often 6 coordinated and from the 2-fold symmetry of the Ni^{II} site, two additional unique atoms (one on the 2-fold axis and one a general position) need to be added in order to complete the coordination. These atoms are placed as oxygen atoms with variable occupancy. At this stage, specific identification of the atom (i.e. whether it is O, F, etc.) is not necessary and will be determined during the later stages of refinement and from charge balance. The final step is the completion of the counterion, TaF_6. This was initially done by placing six fluorine atoms around the Ta with partial occupancy.

This method allows for the F atoms to lie on special or general positions and takes in account the possibility of rotational disorder of the counter ion. From this starting model, simulated annealing was performed in order to determine the rotation of the pyrazines and counterion and occupancies of the various dummy atoms. The additional F atoms, that are unneeded due to symmetry, are then removed from the preliminary structure in order to simplify the model. It is now possible to identify the unknown atoms coordinating to the Ni^{II}. From charge balance (i.e. the unit cell must have no net charge), the three atoms must have a net charge of -1 and each atom has an atomic weight roughly the same as an oxygen, thus the unknown atoms must be two water molecules and a fluorine or perhaps a hydroxy anion. Elemental analysis will be necessary to verify between the fluorine and hydroxy anion.

This preliminary structure was then successfully Rietveld refined (Figure 3.17), which confirmed this structure. In this refinement, bond lengths and angles of a similar nature (i.e. aromatic, N-C, Ta-F bonds) were refined jointly to a single value. Additionally it was necessary to model rotational disorder in the TaF_6 counter ion; this was done by allowing the F atoms to have anisotropic thermal parameters and thus smear out the charge as would occur under a rotation disorder. Atomic positions are tabulated in Appendix B.6.

Figure 3.17: Synchrotron X-ray powder diffraction data obtained at room temperature for **3.4**. Black symbols and red lines represent the experimental data and Rietveld fit, respectively. The solid black line at the bottom of each graph is the difference between the observed and calculated patterns.

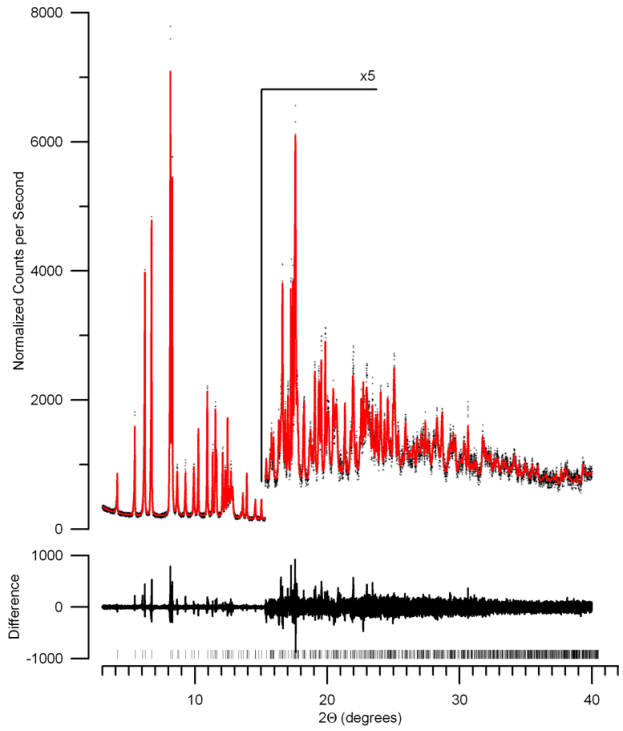

3.3.3 Crystal Structure of $NiF(pyz)_{1.5}(H_2O)_2$ TaF_6

Figure 3.18 provides the atom labeling scheme for **3.4**. The Ni^{II} ion and F7 are on a 2-fold axis while the two unique pyrazines are centered on Wycoff sites with inversion and 2/m symmetry. The Ni^{II} is coordinated to three pyrazines, with two unique N atoms, at an average distance of 2.10 Å. The octahedral coordination is completed by two water molecules and a fluorine ion, with Ni-O and Ni-F distances of 2.16 and 2.01 Å, respectively. The structure is formed by $NiF(pyz)_{1.5}$ layers, which are similar to $Ni(pyz)_2$ planes with one half of a pyrazine replaced by a fluorine. These layers are terminated by waters,

Table 3.6: Crystallographic details for $NiF(pyz)_{1.5}(H_2O)_2$ TaF_6 (**3.4**).

Empirical Formula	$C_6H_{10}O_2N_3F_7TaNi$
Space group	$C2/m$
a (Å)	15.6402(5)
b (Å)	14.6714(4)
c (Å)	7.2347(2)
$\beta(^\circ)$	55.421(2)
V (Å^3)	1366.9(7)
Z	4
$\lambda(\mathring{A})$	0.7002(2)
R_{wp}	7.74
R_{exp}	4.01

which are axially coordinated to the Ni^{II} ion. (Figure 3.19) Additionally, one of the pyrazines has a non-linear ligation to the Ni atom with Ni-N-N angle of 167.71°. The TaF_6 ions occupy the interstitial space between the layers as shown in Figure 3.20. The TaF_6 counterions are rotationally disordered, which is not uncommon for counterions in these types of materials. This structure is quite different than the expected compound of $[Ni(HF_2)(pyz)_2]$ TaF_6 and this knowledge will enable interpretation of the magnetism (which has yet to be collected). This compound highlights the ability of powder diffraction to determine compounds of unknown composition.

Figure 3.18: Asymmetric units and atom labeling schemes for $NiF(pyz)_{1.5}(H_2O)_2$ TaF_6 (**3.4**). Hydrogen atoms have been omitted for clarity.

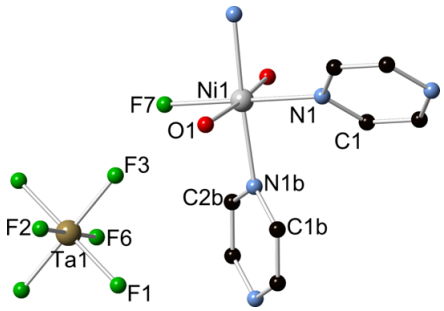

Figure 3.19: View of the layers observed in **3.4**, normal to the layer direction. Counterions have been omitted for clarity. Ni, C, N, F and O atoms are in grey, black, blue, green and red respectively.

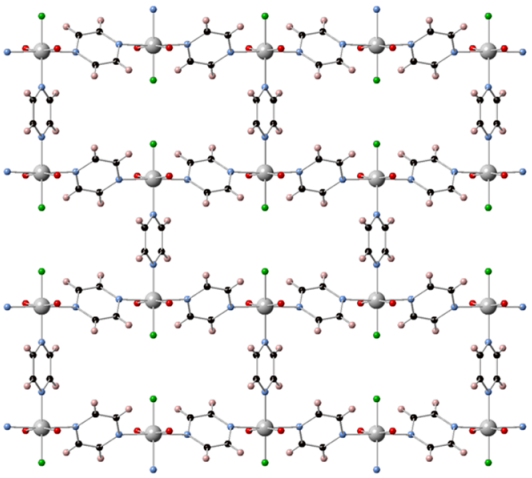

Figure 3.20: View of the structure of **3.4** along the layers.

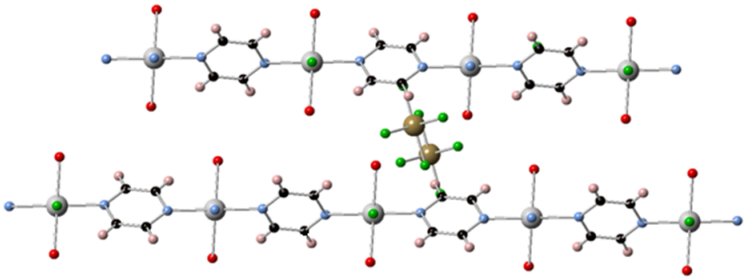

3.4 An Unknown Composition with Impurities: $Ni_2F_2(pyz)_3(H_2O)_4(BF_4)_2$

Unlike with single crystals, a powder sample is not guaranteed to be a single phase. These additional phases are often labeled impurities if they compose a minority of the compound. This introduces further difficulty into the process of structure solution as it becomes difficult to identify which

peaks correspond to which phase, especially so if the phases are of lower symmetry. This situation is further complicated if neither phase is known. The following section will present a particular case of the situation of a material of unknown composition with impurities, $Ni_2F_2(pyz)_3(H_2O)_4(BF_4)_2$. Knowledge of the structure will allow further targeted synthesis efforts in order to isolate the phase of interest. Isolation of a single phase is necessary since in a sample with impurities, it is difficult to assign which properties (i.e. magnetic behavior) are intrinsic in which phase.

3.4.1 Synthesis

The following synthesis was performed by our collaborators, Jordan Corbey and Jamie Manson, at Eastern Washington University. $Ni(BF_4)_2 \cdot 6H_2O$ (0.3529 g) was dissolved in 2 mL of H_2O. Pyrazine (0.5808 g) and pyridine-N-oxide (0.2282 g) were dissolved together in 6 mL solution containing 50/50 H_2O/EtOH. The two solutions were slowly mixed together to afford a teal colored solution. The reaction mixture was covered with parafilm, small holes poked in the top, and the solvent allowed to slowly evaporate at room temperature. A pale blue microcrystalline solid precipitated upon slow evaporation of the solvent for several weeks. The solid was collected via suction filtration yielding 35 mg of product, **3.5**.

3.4.2 Structure Determination

A powder of **3.5** was individually flame-sealed in thin-walled glass capillary tubes and high-resolution powder diffraction patterns collected on beamline X16C located at the National Synchrotron Light Source, Brookhaven National Laboratory.

TOPAS-Academic was used to index **3.5**. If the first twenty peaks were used in the indexing algorithm, a satisfactory unit cell is not produced, which suggests the possibility of multiple phases. By selecting different subsets of these peaks and much trial and error, an indexing of I-orthorhombic (Table 3.7) was achieved; however additional peaks could not be indexed. The identification of systematic absences in the pattern, in order to pick a particular space group, is difficult as these absences are easily masked by the impurity peaks. This leaves a large number of space groups to attempt, specifically: $I222$, $Imm2$, $Immm$, $I2_12_12_1$, $Im2m$, $I2mm$, $Im2a$, $Imma$, $I2mb$, $Immb$, $Ima2$, $Imam$, $I2cm$, $Imcm$, $I2cb$, $Imcb$, $Ibm2$, $Ibmm$, $Ic2m$, $Icmm$, $Ic2a$, $Icma$, $Iba2$ and $Ibam$. Fortunately in coordination compounds, some of the space groups ($Immm$, $Imma$, $Immb$, $Imam$, $Imcm$, $Imcb$, $Ibmm$, $Icmm$, $Icma$ and $Ibam$) are more common than the others. [46]

The fact that both the b and c unit cell dimensions are both approximately 14 Å, which is approximately twice the Ni-pyz-Ni distance of 7 Å, suggests the possibility of $Ni(pyz)_2$ planes in the bc-plane. However the shorter a cell length of 11.2361(3) Å suggests that these planes do not connect to form a 3-D framework.

The highest symmetry site that a pyrazine molecule can occupy is 2/m and

requiring a Wycoff site with this symmetry removes *Immm* from the list of possible space groups. For *Imma* and related space groups, the possible Wycoff sites with 2/m symmetry are 0, 0, 0; 0, 0, 1/2; 1/4, 1/4, 1/4 and 1/4, 1/4, 3/4. For any of these, the nearest site of similar multiplicity that a Ni^{II} ion could reside is at a distance of 11.46 Å. This distance is too large for a Ni-pyz coordination, which preliminarily eliminates these space groups and thus leaves *Imcb*, *Icma* and *Ibam* as possibilities. For the remaining space groups, if a pyrazine is placed at a Wycoff site of symmetry 2/m, the nearest Ni sites are located a quarter of a particular cell axis away (which cell axis depends on which space group; *a* for *Imcb*, *b* for *Icma*, *c* for *Ibam*). In order to fit the Ni-pyz-Ni chain, this distance has to be on the order of 3.5 Å and thus eliminates *Imcb*, which would have a corresponding distance of 2.81 Å, as a possibility.

From this point, model building will have to progress in both *Icma* and *Ibam*, of which the latter will be considered first. The $Ni(pyz)_2$ plane can be completed by adding two more unique pyrazines to the unit cell at 1/2, 1/2, 1/2 and 1/2, 1/4, 1/4. At this point there are two unique Ni atoms; each of these Ni ions is 4-coordinated by the pyrazine molecules. In order to complete the octahedral coordination of the nickel, two more atoms must be placed axially along the line defined by x,0,1/4. However this creates an issue, as the Ni-Ni distance along the *a* axis is 5.618 Å and this would lead to the two added atoms to be within approximately 1.6 Å of each other. (Figure 3.21)

The simplest way to correct this impossibility is to remove one of the pyrazines, as well as the dummy atom that was added to complete the

Figure 3.21: View of the preliminary structure of **3.5** that highlights the incapability of the $Ni(pyz)_2$ planes to fit in the cell as the two fluorine atoms become too close together, ~1.6 Å.

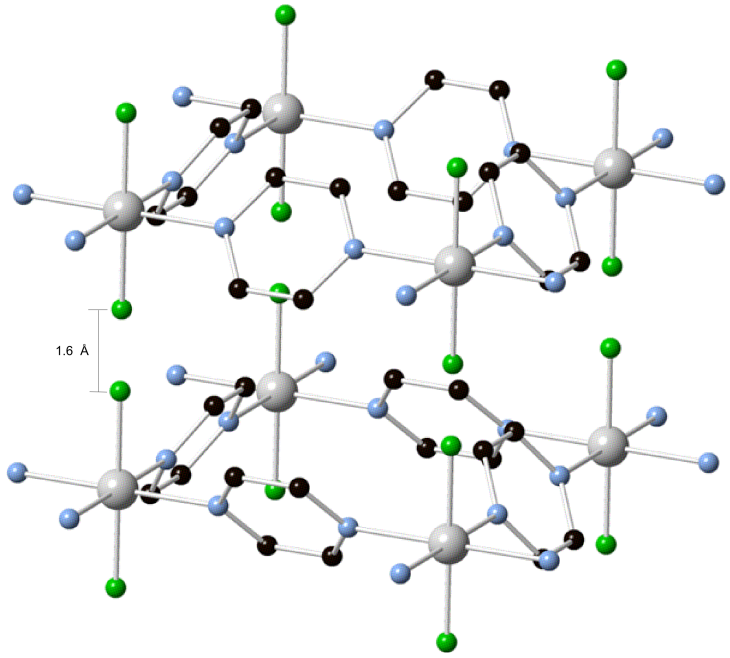

octahedral coordination of one of the nickels, and replace this with a dummy atom, with variable occupancy, in a general position around the Ni atom. This will allow both the Ni ions to be octahedrally coordinated without the atoms getting to close to each other. Finally, the interstitial space between the layers needs to be filled and the most likely candidate for this is a BF_4^- ion. This starting model can be used in simulated annealing and results in a reasonable fit of the pattern. Furthermore from the variable occupancies, the dummy atoms can be assigned to either oxygen (i.e. water) or fluorine atoms and in order to determine which it is necessary to take charge balance into account (i.e. the net charge in the unit cell is zero). Currently, the net charge as currently assigned is +16 (from both Ni atoms) - 8 (from BF_4^- ion) = +8,

Table 3.7: Crystallographic details for $Ni_2F_2(pyz)_3(H_2O)_4(BF_4)_2$ (**3.5**).

Empirical Formula	$B_2C_{12}H_{20}O_4N_6F_{10}Ni2$
Space group	*Ibam*
a (Å)	11.2361(3)
b (Å)	14.1613(4)
c (Å)	14.0986(4)
V (Å^3)	2243.4(8)
Z	4
λ(Å)	0.69989(3)
R_{wp}	9.84
R_{exp}	5.36

which implies that the atom on a special position , which is of multiplicity 8, is a fluorine ion and the other is a water molecule. However, this leads to a question on how a fluorine ion was introduced into the compound, as there was no such ion in the reactants. We currently theorize that the BF_4^- reacted with the glass to produce SiF_6 and released some F^- ions, which were then captured by the Ni^{II}.

This preliminary structure was then successfully Rietveld refined (Figure 3.22), which confirmed this as the correct structure. In this refinement, bond lengths and angles of a similar nature (i.e. aromatic, N-C, B-F bonds) were refined jointly to a single value. Atomic positions are tabulated in Appendix B.7.

3.4.3 Crystal Structure of $Ni_2F_2(pyz)_3(H_2O)_4(BF_4)_2$

Figure 3.23 provides the atom labeling scheme for **3.5**. The structures consists of two unique Ni^{II} ions on Wycoff sites with symmetry 222. Each of these ions are octahedral coordinated with one Ni^{II} coordinated to four

Figure 3.22: Synchrotron X-ray powder diffraction data obtained at room temperature for **3.5**. Black symbols and red lines represent the experimental data and Rietveld fit, respectively. The solid black line at the bottom of each graph is the difference between the observed and calculated patterns. The size of the difference curve arises from the large amount of impurity phases.

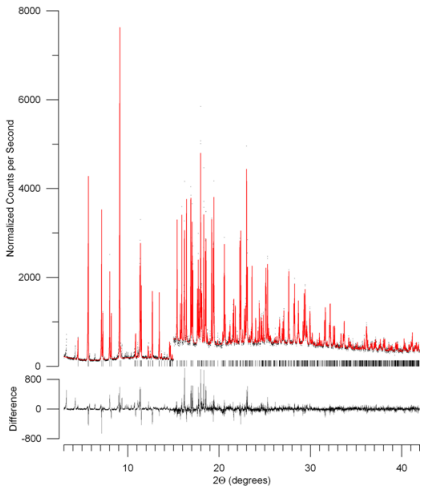

pyrazines and two flourines, while the other is coordinated to two pyrazines and four water molecules, with average Ni-N, Ni-O and Ni-F distances of 2.15, 2.10 and 1.98 Å, respectively. The structure is formed by Ni1-pyz-Ni2-pyz-Ni1 chains that are connected at the Ni2 site by Ni2-pyz-Ni2 chains, which forms 2-D layers. (Figure 3.24) These layers are terminated by F atoms on the Ni2 site and waters on the Ni1 site. BF_4^- ions occupy the interstitial space between the layers (Figure 3.25) The structure is very different than anything that was expected to result from the synthesis. Knowledge of the structure is now driving targeted efforts in isolating this material.

Figure 3.23: Asymmetric units and atom labeling schemes for $Ni_2F_2(pyz)_3(H_2O)_4(BF_4)_2$ (**3.5**). Hydrogen atoms have been omitted for clarity.

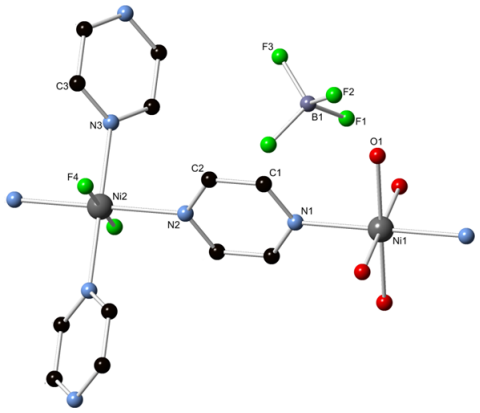

Figure 3.24: View of the layers observed in **3.5**, normal to the layer direction. Counterions have been omitted for clarity. Ni, C, N, F and O atoms are in grey, black, blue, green and red respectively.

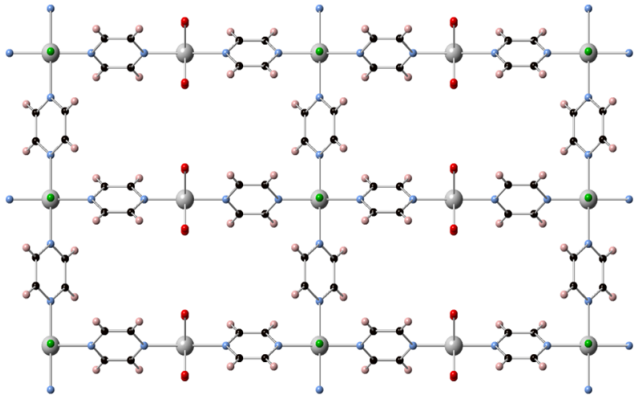

Figure 3.25: View of the structure of **3.5** along the layers.

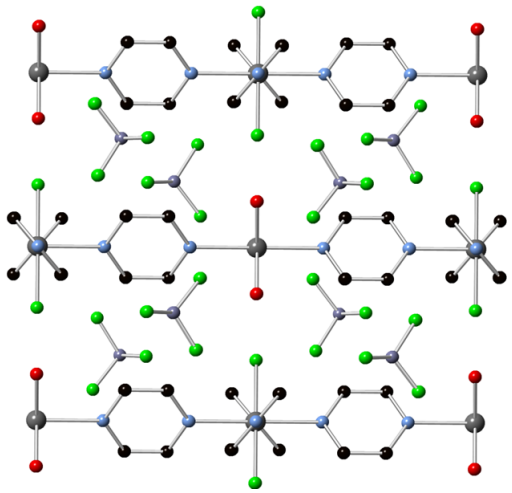

Chapter 4

Prussian Blue Related Compounds

4.1 Introduction

Prussian Blue, with idealized composition of $Fe_7(CN)_{18}$, is another example of a coordination compound in which a cyanide (CN^-) is utilized as the ligand. The idealized Prussian Blue adopts an *fcc* structure with $Fe(CN)_6$ connecting to another Fe to form a 3D network. (Figure 4.1) The actual Prussian Blue structure [47] is quite complicated and contains Fe vacancies (in order to balance charge) and disordered water molecules in the interstitial space. One-fourth of the $Fe(CN)_6$ sites are vacant and are instead filled with water molecules, which coordinate to the Fe ion. Additionally there is a "soluble" version of Prussian Blue, which includes a K^+, that has a chemical formula of $KFe[Fe(CN)_6]$. The replacement of the iron for different transition metals has led to a number of compounds that have the idealized Prussian blue struc-

ture and exhibit ferrimagnetic ordering.[48, 49] This motivated further work studying different replacements of the transition metal and counter ion.

Figure 4.1: A schematic of the idealized *fcc* Prussian Blue structure. [50]

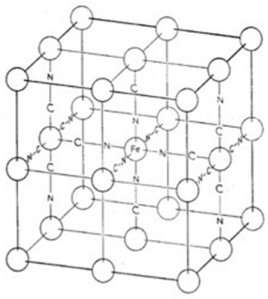

4.2 $Na_2Mn[Mn(CN)_6]$ $2H_2O$ and $Na_2Mn[Mn(CN)_6]$

More specifically, this interest suggested the replacement of Fe with Mn since the more ionic Mn^{II} [51] can allow for a smaller Mn-CN-Mn angle. Previous work in our group determined the structures of $A_2Mn[Mn(CN)_6$ (A= Rb or K) which adopted anomalous non-*fcc* structures. [52] Additionally the structure of $Cs_2Mn[Mn(CN)_6$ had the idealized Prussian Blue *fcc* structure. The magnetic ordering temperature, T_c, for this family of compounds increased as the MnNC angle decreased. In order to further extend this correlation, the sodium analogue, $Na_2Mn[Mn(CN)_6]$, was sought.

4.2.1 Synthesis

The following synthesis processes were performed by our collaborators, Christopher Kareis and Joel Miller, at University of Utah. In order to syn-

thesize **4.1**, to a 5 mL aqueous solution of $Mn(O_2CMe)_2$ (250 mg, 1.44 mmol) was added a 5 mL aqueous solution of NaCN (356 mg, 7.26 mmol). A gray precipitate immediately formed that turned yellow then blue within 15 min. After 4 h of stirring, the blue powder was collected by filtration, washed with 5 3 mL of water and 5 mL of Et_2O, and dried under vacuum at room temperature for 1 h.

In a typical synthesis of **4.2**, 100 mg of **4.1** was placed into a vial within a vacuum oven at room temperature. The temperature was increased by 10 °C every 30 min until reaching 110 °C, and then held at 110 °C for 8 h. During this time, the color of the solid went from the dark blue characteristic of **4.1** to a dark green characteristic of $A_2Mn[Mn(CN)_6]$ (A = K, Rb).

4.2.2 Structural Determination of $Na_2Mn[Mn(CN)_6$ $2H_2O$

4.1 was successfully indexed, with the use of TOPAS-Academic [14], and from the Pawley fit a space group of $P2_1/n$ was tentatively assigned. Details of the unit cell are included in Table 4.1. The unit cell for **4.1** is very similar to the cell for $K_2Mn[Mn(CN)_6$, which suggested that the structures are similar as well. Using the structure of $K_2Mn[Mn(CN)_6$ [52] as an initial model, it is possible to Rietveld refine this model by allowing rotations of the $Mn(CN)_6$ octahedra, however this structure does not produce a satisfactory fit of the data. (Figure 4.2) This model fits the large peaks well but does not fit the smaller peaks satisfactorily, which suggests that the model is deficient in some manner.

Figure 4.2: Fit of the synchrotron powder diffraction data for **4.1** using a model of a structure similar to $K_2Mn[Mn(CN)_6]$. The enlarged section highlights the problem with this initial model

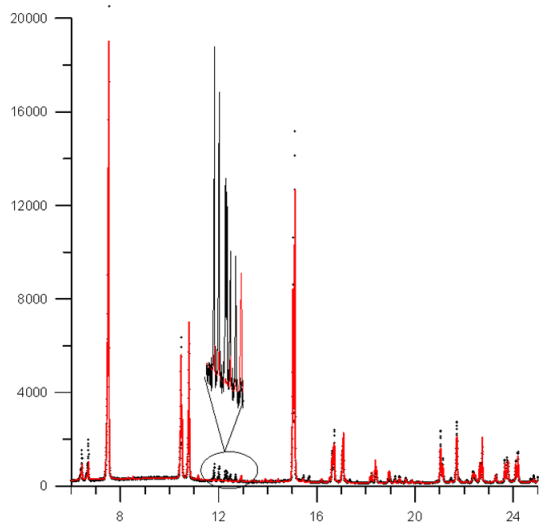

The simplest change that can be made to the model is the inclusion of an additional atom to fill the interstitial space. A dummy atom (an oxygen with variable occupancy) was placed and simulated annealing was performed in which the $Mn(CN)_6$ octahedra were allowed to rotate and both the Na and oxygen were moved in the interstitial space. This resulted in a reasonable fit to the diffraction pattern and the occupancy of the dummy atom allowed us to assign it as a water molecule. From this preliminary solution, the structure was successfully refined. (Figure 4.3a) The orientation of the cyano group was not clearly distinguished from the fit and the atoms were assigned from the nearest Mn distance, since the Mn-C distance should be shorter than the Mn-N distance. Atomic positions are tabulated in Appendix B.8.

Figure 4.3: High-resolution synchrotron powder diffraction data (dots) and Rietveld fit (line) of the data for $Na_2Mn[Mn(CN)_6]$ $2H_2O$, **4.1** (a), and $Na_2Mn[Mn(CN)_6]$, **4.2** (b). The lower traces for each plot are the differences, measured - calculated, plotted to the same vertical scale

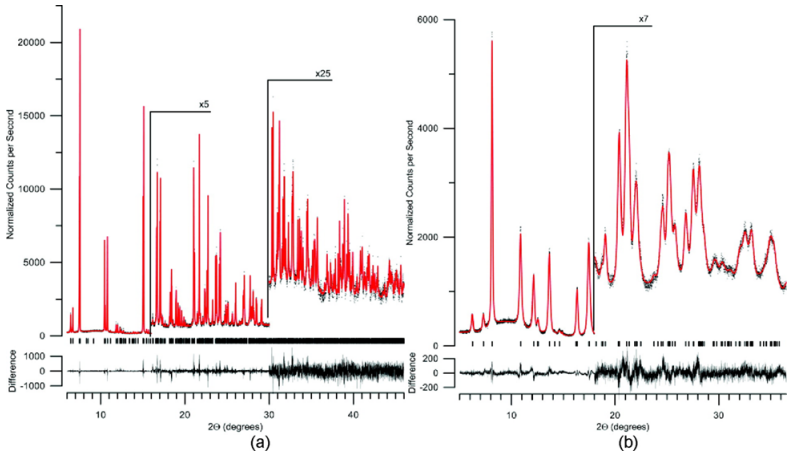

4.2.3 Structural Determination of $Na_2Mn[Mn(CN)_6$

4.2 was successfully indexed, with the use of TOPAS-Academic [14], and a space group of $R\overline{3}$ was tentatively assigned. Details of the unit cell are included in Table 4.1. Unlike with **4.1**, there is no apparent similarity between this unit cell and the cell for $K_2Mn[Mn(CN)_6$. If a composition of $Na_2Mn[Mn(CN)_6]$ is supposed, the number of formula units per cell can be calculated by dividing the cell volume by 17 $Å^3$ per atom, $\frac{730.17}{17\times16} = 2.68 \approx 3$. This suggests that Mn^{II} atoms are on sites of symmetry $\overline{3}$ (Wycoff sites a and b) and thus the cyano group is on a general position coordinated around one of the Mn atom. Finally, the counterion, Na^+, must be placed on a site of multiplicity 6 (Wycoff site c). This model was used in simulated annealing in order to find the correct placement of the counterion and cyano group. From this initial structure solution, the structure was successfully refined. (Figure 4.3b) Once again, the orientation of the cyano group was not clearly

Table 4.1: Summary of crystallographic parameters for $Na_2Mn[Mn(CN)_6]$ $2H_2O$ (**4.1**), and $Na_2Mn[Mn(CN)_6]$ (**4.2**).

	$Na_2Mn[Mn(CN)_6]$ $2H_2O$, **4.1**	$Na_2Mn[Mn(CN)_6]$, **4.2**
	Monoclinic	Hexagonal
MW, g/mol	171.99	155.99
a, Å	10.66744(32)	6.6166(3)
b, Å	7.60223(23)	6.6166(3)
c, Å	7.40713(22)	19.2585(9)
α, °	90	90
β, °	92.4379(28)	90
γ, °	90	120
V, Å^3	600.148(31)	730.17(9)
Z	4	6
Space group	$P2_1/n$	$R\bar{3}$
ρ_{calc}, g/cm^3	1.903	2.128
R_{wp}	7.88	3.99
R_{exp}	4.60	3.13

distinguished and the atoms were assigned from the nearest Mn distance, since the Mn-C distance should be shorter than the Mn-N distance. Atomic positions are tabulated in Appendix B.8.

4.2.4 Crystal Structure of $Na_2Mn[Mn(CN)_6]$ $2H_2O$

The structure of $Na_2Mn^{II}[Mn^{II}(CN)_6]$ $2H_2O$ (**4.1**) is made of $Mn^{II}(CN)_6$ which are coordinated to another Mn^{II} ion, with average Mn-C distances of 1.926(6) Å(Figure 4.4a) and average Mn-N bond lengths of 2.264(4) Å(Figure 4.4b). These values are comparable with the Mn^{II}-C and Mn^{II}-N distances observed in $Na_4[Mn(CN)_6]10H_2O$,[53, 54], $NaMn[Cr(CN)_6]$, [55] $K_2Mn[Mn(CN)_6]$ and $Rb_2Mn[Mn(CN)_6]$[52].

These difference in bond lengths was used to assign the C-bound to a

Figure 4.4: $Mn(CNMn)_6$ (a,c) and $Mn(NCMn)_6$ (b,d) octahedral coordination for **4.1**(a,b) and **4.2**(c,d), respectively. [Low-spin (S = 1/2) Mn^{II} is orange; high-spin (S = 5/2) Mn^{II} is maroon; C is black; and N is light blue.]

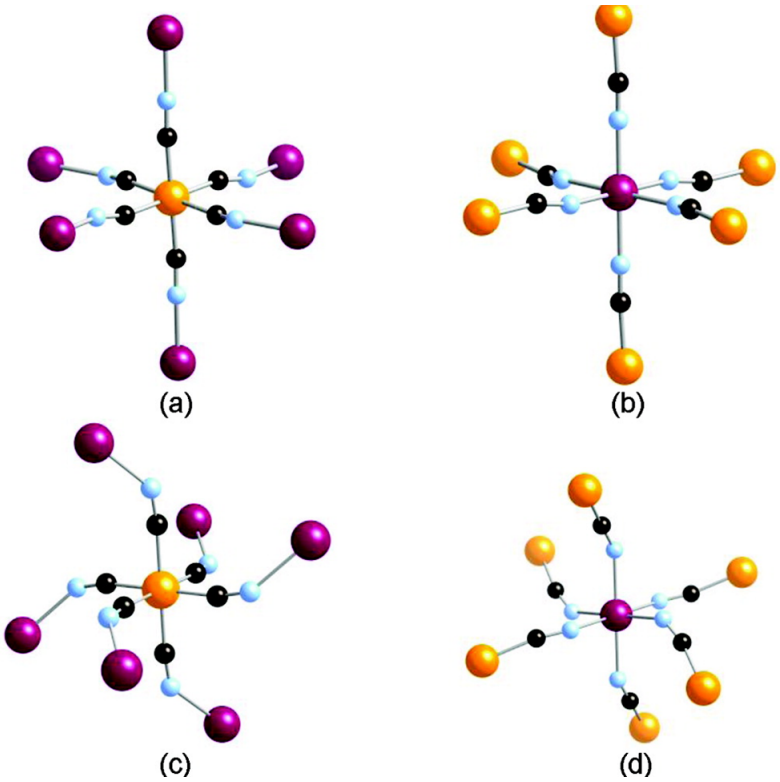

low-spin Mn^{II} and N-bound to a high-spin Mn^{II}. The Mn-C-N angles of 174.6(7)°, 176.0(8)°, and 177.7(7)° are near 180° as expected for $Mn^{II}(CN)_6$. The Mn-N-C angles of 162.2(5)°, 162.6(6)°, and 171.0(7)° are substantially non-linear, which continues the trend that was observed for $A_2Mn[Mn(CN)_6]$ (A = K, Rb) [52], which had Mn-N-C angles of 148.8° and 153.3°, respectively. Each cyano group bridges a two Mn^{II} ions to form a 3-D framework. (Figure 4.5a) Na^+ and water occupy the interstitial spaces of the framework.

Each Na^+ counterion is loosely coordinated to two water molecules with Na-O distances of 2.43 and 2.57 Å. The Na^+ and water form a chain that fills

Figure 4.5: View normal to the *bc* plane of the 3-D network lattice for **4.1** (a) and **4.2** (b), showing MnC_6 surrounded by four MnN_6 octahedra (and vice versa) twisting with respect to each other (Na^+ and H_2O for **4.1** are not shown for clarity). [Low-spin (S = 1/2) Mn^{II} is orange; high-spin (S = 5/2) Mn^{II} is maroon; C is black; and N is light blue.]

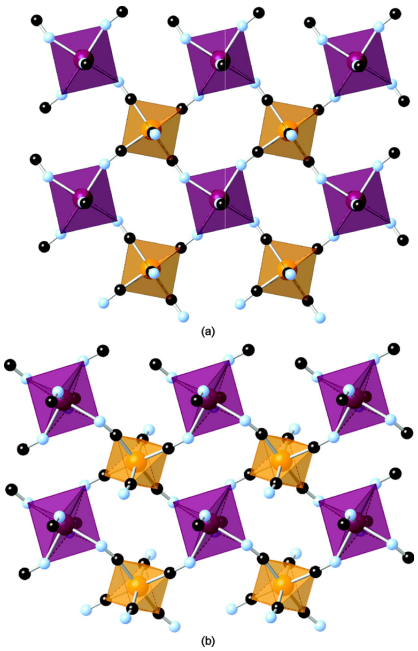

the interstitial space of the $Mn^{II}[Mn^{II}(CN)_6]$ framework, Figure 4.6.

4.2.5 Crystal Structure of $Na_2Mn[Mn(CN)_6]$

Similar to **4.1**, the structure of $Na_2Mn[Mn(CN)6]$ (**4.2**) is composed of $Mn^{II}(CN)_6$ which are coordinated to another Mn^{II} ion, with average Mn-C distances of 1.926(6) Å(Figure 4.4c) and average Mn-N bond lengths of 2.264(4) Å(Figure 4.4d). Similar to **4.1**, the difference in bond lengths was used to assign the low-spin and high-spin Mn^{II}. The Mn-C-N and Mn-N-C angles are 167.0(4)° and 142.4(4)°, respectively, and both deviate from substantially from

Figure 4.6: 1-D Na H_2O chains (gray) that interpenetrate the 3-D Mn[Mn(CN)6] framework (black) for **4.1**.

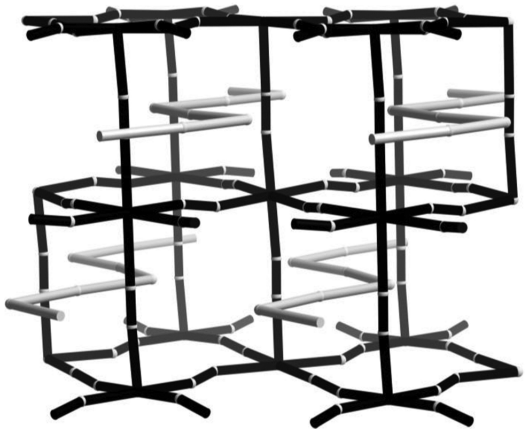

Figure 4.7: Perspective view of *fcc* $Cs_2Mn^{II}[Mn^{II}(CN)_6]$ (a), monoclinic **4.1** (b), and rhombohedral **4.2** (c). The cations are not shown for clarity. [Low-spin (S = 1/2) Mn^{II} is orange; high-spin (S = 5/2) Mn^{II} is maroon; C is black; and N is light blue.]

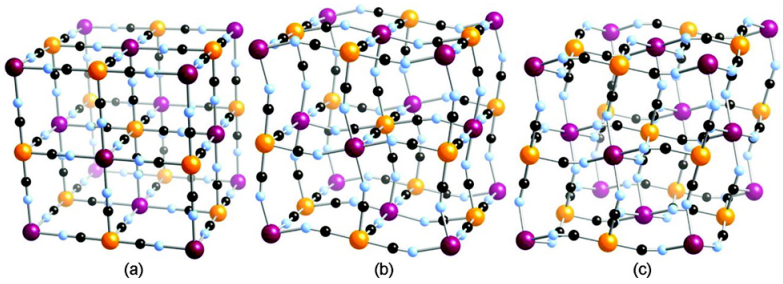

180°. Each cyanide bridges the two Mn^{II} ions to form a 3-D framework (Figure 4.5b). The Na^+ ion occupies the interstitial space in the framework. Due to the severe buckling of the framework, as evidenced by the nonlinear Mn-C-N and Mn-N-C angles, the Mn-Mn separation of 4.99 Å is substantially less than that what was observed for **4.1** and $A_2Mn[Mn(CN)_6]$ (Table 4.2). [52]

Figure 4.8: View along the *a*-axis for *fcc* $Cs_2Mn^{II}[Mn^{II}(CN)_6]$ (a), monoclinic **4.1** (b), and rhombohedral **4.2** (c) showing the location of the respective cations. [Low-spin (S = 1/2) Mn^{II} is orange; high-spin (S = 5/2) Mn^{II} is maroon; Cs is brown, O is red; Na is yellow; C is black; and N is light blue.]

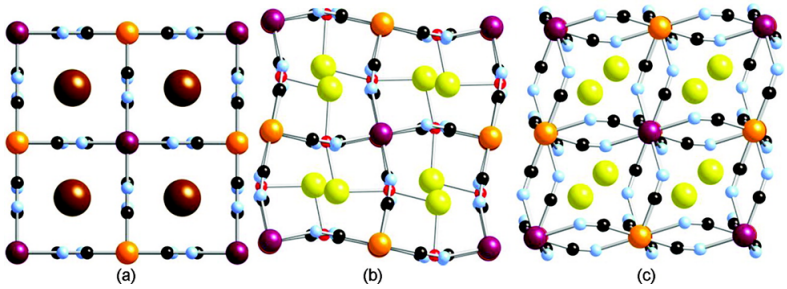

4.2.6 Comparison of the $A_2Mn^{II}[Mn^{II}(CN)_6]$ (A = Na, K, Rb, Cs) Structures

As mentioned previously, the more ionic Mn^{II} [51] allowed for a non-linear Mn-CN-Mn angle, which results in further distortions of the lattice with smaller counterion size ($Cs^+ > Rb^+ > K^+ > Na^+$) in order to minimize void space. This behavior has been observed in other materials, such as $A[(Me_3tacn)_6MnCr_6(CN)_{18}](ClO_4)_3$ (A = Na, K; Me_3tacn = N,N',N"-trimethyl-1,4,7-triazacyclononane), which has bent cyanide ligands with a Mn-N-C angle of 152.7° and 153.4°. [56]

Dehydration of **4.1** to **4.2** led to structural transformation from a monoclinic to a rhombohedral unit cell. As mentioned previously, both of these structures differ from the idealized *fcc* Prussian blue structure, as was the case for the monoclinic $A_2Mn^{II}[Mn^{II}(CN)_6]$ (A = K, Rb). [52] The biggest differences between these compounds are the Mn-N-C angles that deviate significantly from linearity, Table 4.2. This nonlinearity buckles the structure

Table 4.2: Comparison of structural features of $A_2Mn^{II}[Mn^{II}(CN)_6]$ (A = Na, K, Rb, Cs).

Compound	∠MnCN,°	∠MnNC,°	Mn-Mn, Å
4.1	176.1	165.3	5.33
4.2	167.0	142.4	4.99
$K_2Mn^{II}[Mn^{II}(CN)_6]$ [52]	173.2	148.8	5.09
$Rb_2Mn^{II}[Mn^{II}(CN)_6]$ [52]	177.2	153.3	5.19
$Cs_2Mn^{II}[Mn^{II}(CN)_6]$ [52]	180	180	5.30

lowering the symmetry from cubic, as observed for $Cs_2Mn^{II}[Mn^{II}(CN)_6]$ [52] (Figures 4.7a and 4.8a), to monoclinic for **4.1** (Figures 4.7b and 4.8b), and to rhombohedral for **4.2** (Figures 4.7c and 4.8c).

The structure of **4.1** is a consequence of the distortion to a monoclinic unit cell, as such it is structurally similar to $A_2Mn^{II}[Mn^{II}(CN)_6]$ (A = K, Rb).[52] The monoclinic **4.1** and rhombohedral **4.2** structures are shown in Figures 4.7 and 4.8, which illustrates the increasing distortion of the lattice from cubic to monoclinic to rhombohedral. The monoclinic unit cell is related to the classic Prussian blue unit cell, with cell length a, and adopts unit cell dimensions that are approximately a, $\frac{a}{\sqrt{2}}$, $\frac{a}{\sqrt{2}}$, $\beta \approx 90°$, while the rhombohedral unit cell has dimensions that are approximately $\frac{a}{\sqrt{2}}$, $\frac{a}{\sqrt{2}}$, $\sqrt{3}a$.

4.2.7 Distortion Mode Analysis

As mentioned previously and can be observed in Figures 4.7 and 4.8, both **4.1** and **4.2** are distortions of the *fcc* $Cs_2Mn^{II}[Mn^{II}(CN)_6]$. The distortions result from the relaxation of a symmetry operation of the parent $Cs_2Mn^{II}[Mn^{II}(CN)_6]$ structure. The symmetry elements that still exist will

form the space group of the new phase, thus the new phase is an isotropy subgroup of the parent space group. Each of these reductions will produce a distortion mode and since these distortion modes are orthogonal, the structure can be considered as a combination of distortion modes and their corresponding amplitudes. Each distortion mode will move a series of atoms in some joint way, such as in **4.2** where the mode GM_4^+ corresponds to an in-phase rotation about the new b-axis. While this new representation of the structure in terms of distortion modes does not reduce the degrees of freedom for the structure (i.e. the number of distortions modes is equivalent to the number of degrees of freedom of the individual atoms), in most cases only a subset of the distortion modes will have a significant amplitude. This technique has been quite successful in describing perovskites. [57]

Since each distortion mode arises from loss of symmetry of the parent structure, it is useful to create a symmetry map which shows the structure of the parent space group and its relation to the isotropy group of interest. The Bilbao crystallography server [58] was used to create such maps for **4.1** and **4.2**.(Figures 4.9 and 4.10) Each arrow on the symmetry map corresponds to one distortion mode and thus **4.1** and **4.2** can be classified by 20 and 4 distortions modes, respectively.

ISODISTORT [59] was used to perform the distortion mode analysis with the *fcc* $Cs_2Mn^{II}[Mn^{II}(CN)_6]$ [52] used as the parent (undistorted) structure. It is needed to disregard the water in **4.1** in this analysis as there is no corresponding position in the parent structure.

For **4.1**, there are a large number of allowed distortion modes, however only four of which are important: X_3^+, X_5^+, GM_4^+ and GM_5^+. X_5^+ corresponds to

Figure 4.9: Symmetry map showing the distortion route to **4.1**

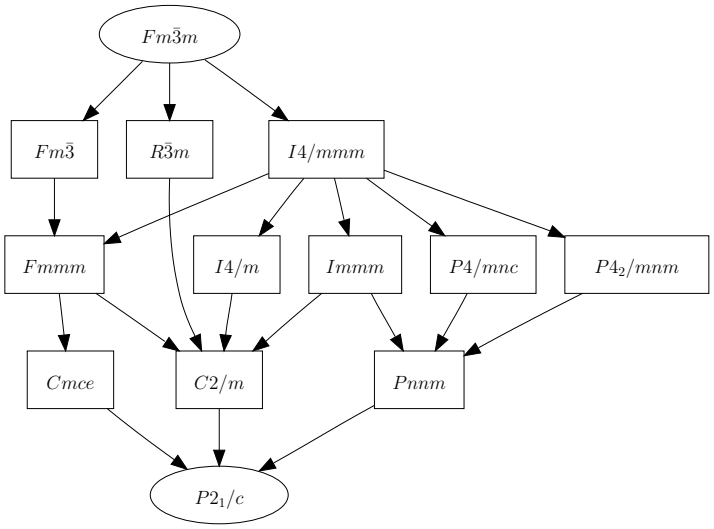

Figure 4.10: Symmetry map showing the distortion route to **4.2**

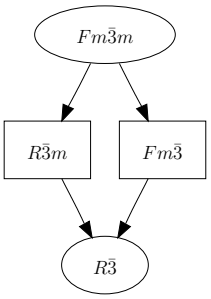

translation of the counterion Na^+ along the b-axis, while GM_5^+ correspond to translation along the c-axis. GM_4^+ corresponds to an in-phase rotation of the $Mn^{II}(CN)_6$ around the new b-axis, while X_3^+ corresponds to an out of phase rotation around the new a-axis. This results in a reduction of the number of necessary parameters from 24 (three for each C, N, O and Na) to nine (GM_4^+ and X_3^+ for N and C; X_5^+ and GM_5^+ for Na; three for position of the water which was not in the parent structure).

For **4.2**, there are 4 allowed distortion modes: GM_1^+, GM_2^+, GM_4^+ and

GM_5^+. Only two particular modes have a significant amplitude: GM_4^+ and GM_5^+. GM_4^+ corresponds to in-phase rotation of the $Mn^{II}(CN)_6$ around the new c-axis. GM_5^+ corresponds to motion of the Na^+ ion along the new c-axis. This results in a reduction of the number of necessary parameters from seven (three for C and N; one for Na) to three (GM_4^+ for N and C; GM_5^+ for Na). Thus for both **4.1** and **4.2**, distortion mode analysis is more natural approach to describing the structure.

4.2.8 Magnetism of $Na_2Mn[Mn(CN)_6]$ and $Na_2Mn[Mn(CN)_6]$ $2H_2O$

Magnetic measurements were performed by our collaborators, Christopher Kareis and Joel Miller, at University of Utah. The magnetic susceptibilities, χ, of **4.1** and **4.2** are plotted as χT and χ^{-1}, Figure 4.11. A fit of the χ^{-1} data for **4.2** to the Néel hyperbolic equation (See Appendix A for a derivation of this equation),

$$\chi^{-1} = \frac{T-\theta}{C} - \frac{\zeta}{T-\theta'} \tag{4.1}$$

(Figure 4.11) gives θ, θ', and ζ of -35 K, 48 K, and 215 mol/emuK, respectively. Due to small impurities of **4.1** in the sample of **4.2**, it was not possible to fit χ^{-1} data for **4.1**. Maxima in the χT data suggest T_c values of 21 and 57 K for **4.1** and **4.2**, respectively.

As shown previously in Table 4.2, this family of Prussian Blue analogs have increased buckling (deviation of the Mn-N-C angle from 180°) with decreasing counter ion size [142.4° (Na^+) > 148.8° (K^+) > 153.3° (Rb^+) > 165.3° (Na^+

Figure 4.11: χT (a) and χ^{-1} (b) for **4.2** ($\times$) and **4.1** ($\bullet$). The solid line in (b) represents the best fit to the Néel hyperbolic equation, eq 4.1. This figure is reprinted from [60].

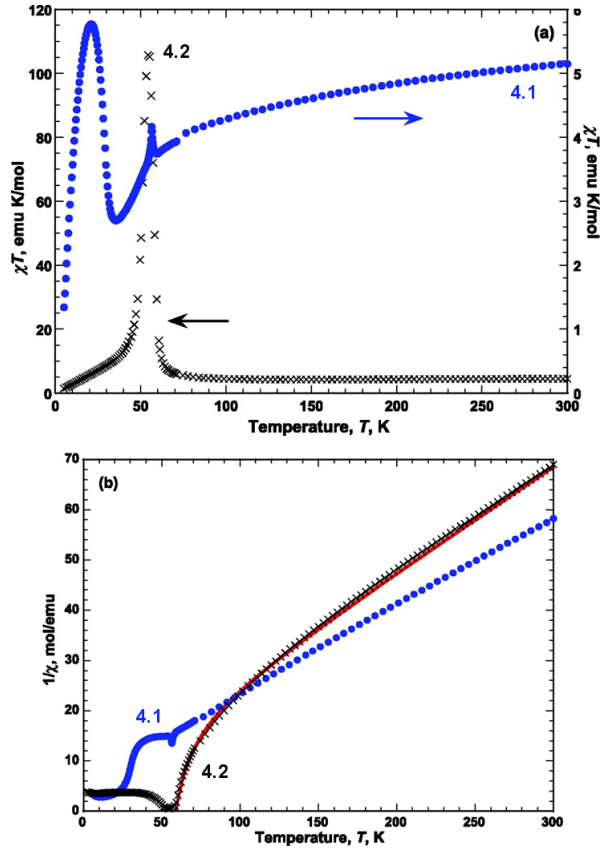

$H_2O) > 180°$ (Cs^+)]. This buckling coincides with an increase of the magnetic ordering temperature,T_c [57 K (Na^+) > 41 K (K^+) > 34.6 K (Rb^+) > 30 K (Na^+ H_2O) > 21 K (Cs^+)]. (Figure 4.12) This is a strong correlation between magnetic and structural properties. This has motivated further study of Mn^{II} and cyanide containing complexes, as will be shown in the next sections.

Figure 4.12: Correlation of increasing T_c with the Mn-N-C angle for $A_2Mn^{II}[Mn^{II}(CN)_6]$ (A = Na, K, Rb, Cs). The line is a general guide for the eye. This figure is reprinted from [60].

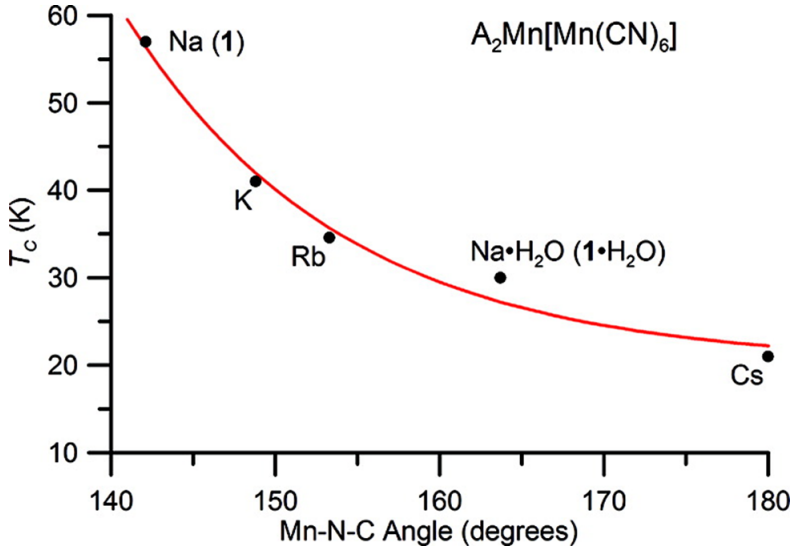

4.3 $Mn(CN)_6Mn_4(OH)_4$ $5H_2O$: An attempt at $Li_2Mn[Mn(CN)_6]$

The natural continuation in further examining the correlation between the Mn-N-C angle and T_c would be the use of yet a smaller counter ion, for instance Li^+. An attempt was made to make this compound, however a compound of a very different and unexpected structural motif was created instead, as will be discussed in the following sections.

4.3.1 Synthesis

To a 10 mL aqueous solution of $Mn(O_2CMe)_2$ (250 mg, 1.44 mmol) was added a 10 mL aqueous solution of NaCN (350 mg, 7.14 mmol). The resulting clear solution was allowed to stir for 4 days. During this time the color of the

solution turned yellow and a green precipitate formed. The green solid was collected by filtration, washed with 5 × 2 mL of H2O and 10 mL ether, and dried under vacuum at room temperature for 3 h (Yield: 95 mg, 52Alternatively the compound can be made with the use of LiCN.

4.3.2 Structural Determination

4.3 was successfully indexed, with the use of TOPAS-Academic [14], and rhombohedral cell was determined with lattice dimensions of $a = 10.2322$ Å and $c = 33.4425$ Å (Table 4.3). This is a much larger cell than reported for any of the previous Prussian Blue analogs. Additionally, the unit cell did not seem to have any similarities with any previously reported cells. This was the first hint that something unexpected was created.

The first version of this compound encountered was the sodium version as mentioned in section 4.3.1. Charge flipping, as implemented in Superflip [37] was performed on this compound and the $Mn(CN)_6$ motif could be identified. (Figure 4.13) However the cyano group was also coordinated to a feature that could not easily be identified. It is of note that Direct Methods, as implemented in EXPO2004 [61], produced similar results. This feature seemed to consist of a cube with atoms on the corners, consisting of four heavier atoms and four lighter atoms. The only candidate for the heavy atom is Mn, but it was not possible to identify the lighter atom as oxygen or sodium. The feature did not seem to make sense in regards to the synthesis and thus presented great difficulty in the interpretation of the density map. Additionally, as was

Figure 4.13: Charge density map of **4.3** produced by charge flipping, as visualized in VESTA. [35] The $Mn(CN)_6$ motif has been circled to assist with identification.

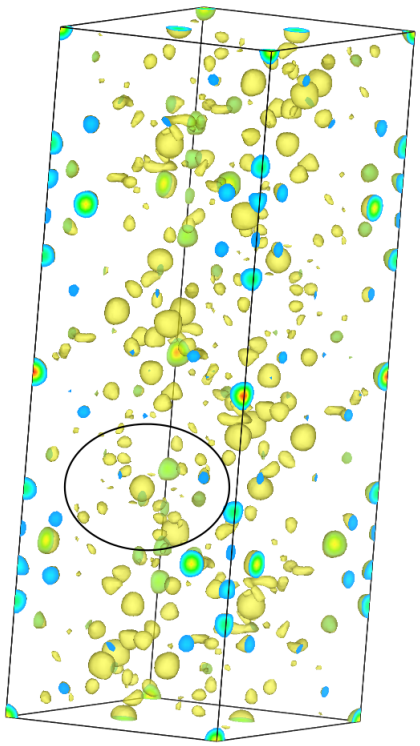

mentioned earlier, a downside to charge flipping is that the density map produced is not always correct and this led to doubt of the actual nature of this motif.

A breakthrough in solving the structure came about when an attempt to make $Li_2Mn[Mn(CN)_6$ resulted in an identical diffraction pattern. (Figure 4.14) This suggested that neither Na or Li was actually in the compound and thus the unidentified structure is most probably Mn_4X_4, X= H_2O, OH^- or O. In order to complete the coordination of the Mn atom, additional atoms

Figure 4.14: Diffraction patterns of the (a) Na^+ and (b) Li^+ versions of **4.3** in order to illustrate the strong similarities between the two patterns.

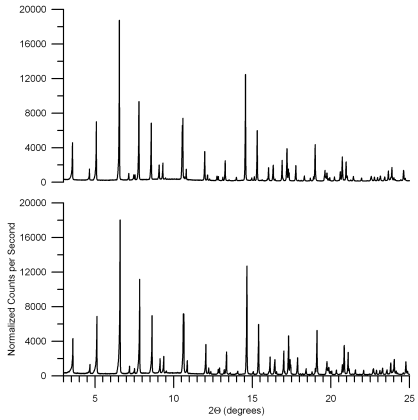

Table 4.3: Summary of crystallographic parameters for $Mn(CN)_6Mn_4(OH)_4$ $5H_2O$ (**4.3**)

Space group	$R\overline{3}$
a, Å	10.2322(4)
c, Å	33.4425(10)
α, °	90
β, °	90
γ, °	120
V, Å^3	3032.25(8)
R_{wp}	6.82
R_{exp}	4.59

with variable occupancy were added. This initial model was placed into simulated annealing and a preliminary structure was determined and the additional added atoms were identified to be water molecules. From charge balance, it was determined that the cube needed to contain OH^- and the the compound was determined to be $Mn(CN)_6Mn_4(OH)_4$ $5H_2O$. The structure was then successfully refined as free atoms, with the restraint that Mn-C and C-N bond lengths are identical in the compound. (Figure 4.15) Atomic positions are tabulated in Appendix B.9.

Figure 4.15: High-resolution synchrotron powder diffraction data (dots) and Rietveld fit (line) of the data for **4.3**. The lower trace is the differences, measured - calculated, plotted to the same vertical scale

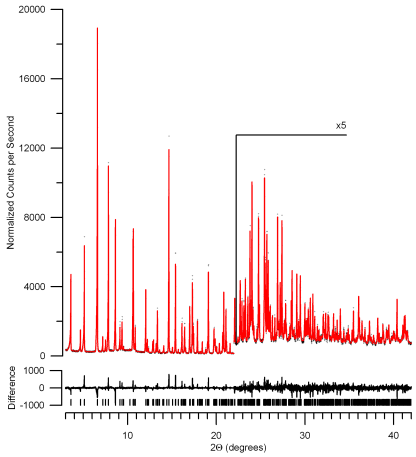

4.3.3 Crystal Structure of $Mn(CN)_6Mn_4(OH)_4$ $5H_2O$

Figure 4.16: View of the $Mn_4(OH)_4$ cube. (Mn is maroon; C is black; and N is light blue.)

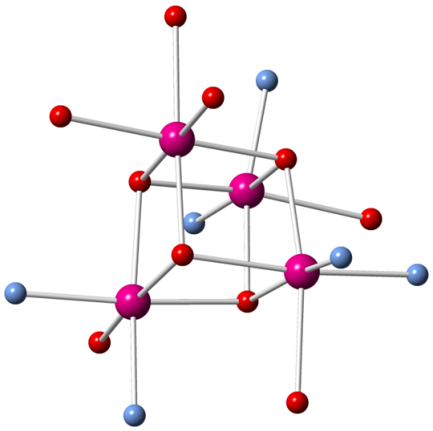

The $Mn_4(OH)_4$ cube consists of two unique Mn atoms; one of which is coordinated to three $(OH)^-$, one H_2O and each of the unique $Mn(CN)_6$, while the other Mn is coordinated to three $(OH)^-$ and three water molecules. (Figure 4.16)

Figure 4.17: View of the 3-D network lattice of **4.3**, showing $Mn(CN)_6$ surrounded by $Mn_4(OH)_4$ cubes (Mn is maroon; C is black; and N is light blue.)

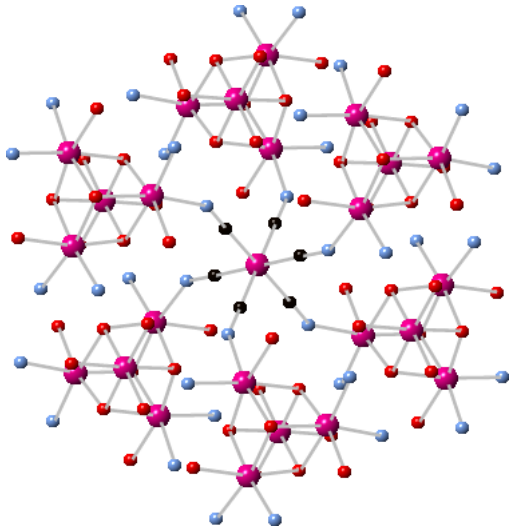

The structure consists of two unique $Mn(CN)_6$ motifs with each on a site with $\overline{3}$ symmetry. Each cyano group is additionally coordinated to a $Mn_4(OH)_4$ cube, which is further connected to other $Mn(CN)_6$ and thus extends into a three dimensional network. (Figure 4.17) The compound has two unique Mn-N-C angles of 144.37° and 162.34 °. $Mn_4(OH)_4$ has been structurally and magnetically characterized previously as a single molecule magnet [62], but this is first example of it appearing in a three dimensional connected network. This compound particularly highlights the need for structural studies, as without knowledge of the existence of $Mn_4(OH)_4$ in the compound, it would not have been possible to interpret and understand any of the physical properties of the compound.

4.3.4 Magnetism of $Mn(CN)_6Mn_4(OH)_4$ $5H_2O$

Magnetic measurements were performed by our collaborators, Christopher Kareis and Joel Miller, at University of Utah.

Figure 4.18: Magnetic susceptibility, χ, for **4.3**

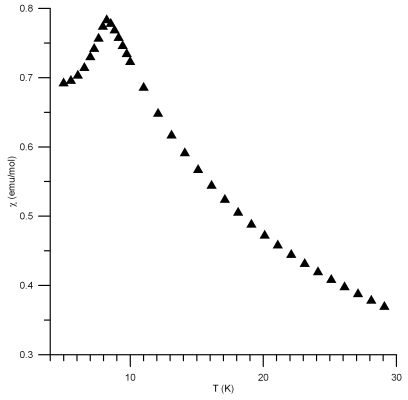

Figure 4.19: χT ($\times$) and χ^{-1} ($\bullet$) for **4.3**.

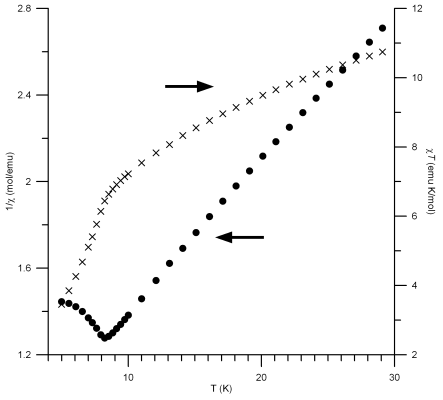

The magnetic susceptibility, χ, of $Mn(CN)_6Mn_4(OH)_4$ $5H_2O$ (**4.3**) was measured and is plotted as χ (4.18), χT and χ^{-1} (Figure 4.19). χ for **4.3** increases with decreasing temperature until it reaches a sharp maxima at 8.2 K . The peak in χ is suggestive of antiferromagnetic ordering. Above

60 K, χ^{-1} is linear and was fit to the Curie-Weiss equation resulting in a θ of $\sim$-11.5 K. Currently, there is not a complete understanding on how the structure correlates with this magnetic behavior. The primary reason for this is it is not currently clear how $Mn_4(OH)_4$ behaves magnetically in such a 3-D framework. However knowledge of the structure will be key to untangling this correlation.

4.4 Prussian Blue Analogs with Larger Cations: NMe_4^+

As the replacement of the counter ion in $A_2Mn[Mn(CN)_6$ with smaller counter ions produced distortions in the structure that led to differences in the magnetic behavior. Additionally, a strong correlation between structural parameters and the transition temperature, T_c, was found. This lead to the attempt to replace the counter ion with a larger counter ion, specifically NMe_4^+. As mentioned in the previous chapter 3.3, this can often lead to the framework distorting radically and the creation of a novel coordination environment. Additionally, this phenomenon was observed when the counter ion was replaced with NEt_4^+ [63].

4.4.1 Synthesis

The following synthesis processes were performed by our collaborators, Christopher Kareis and Joel Miller, at University of Utah. In order to synthe-

size **4.4**, $[NEt_4](CN)$ (517 mg, 5.16 mmol) was dissolved in a 5 mL of H_2O, and the solution was dropwise added to a 5 mL aqueous solution containing $Mn(O_2CMe)_2$ (255 mg, 1.47 mmol). A yellow precipitate formed that turned light green, and the mixture was stir for ∼12 hr. The light green solid was then filtered, using a medium frit, washed with H_2O (2 x 5 mL), MeOH (2 x 5 mL), and Et_2O (2 X 5 mL). The solid was then placed under vacuum, on the frit, for 2 hr and then isolated (Yield 250 mg; 98%).

4.4.2 Structural Determination

High-resolution synchrotron X-ray powder diffraction patterns was collected at the X16C beamline at the National Synchrotron Light Source at Brookhaven National Laboratory.

Indexing of the diffraction, with the use of TOPAS Academic [14], resulted in a hexagonal cell. (Table 4.4) This cell is quite different than previously reported cells for Prussian Blue materials, which suggest a different unknown composition. Of particular note is the short c axis of 5.77 Å, which suggests the possibility of Mn-CN-Mn chains along the c direction.

Charge flipping, as implemented in Superflip [37] was performed. From the charge density map, the location of heavy atoms were determined, specifically there were two unique Mn atom sites. Cyano groups were placed in order to bridge adjacent Mn ions resulting in a 6-coordinate octahedral Mn ion and a 5-coordinate trigonal bipyramidal Mn ion. The cyano groups pointed in the c direction are orientationally disordered, arising from that fact that the two atoms are symmetry equivalent. In the interstitial space remaining, a counte-

rion, NMe_4^+ was placed. From the difference in symmetry between NMe_4^+ and its environment, the counter ion is highly disordered.

However upon close examination of the fit to the diffraction pattern, there

Figure 4.20: A fit of the powder diffraction pattern with the initial model of **4.4** in order to highlight deficiencies in the model.

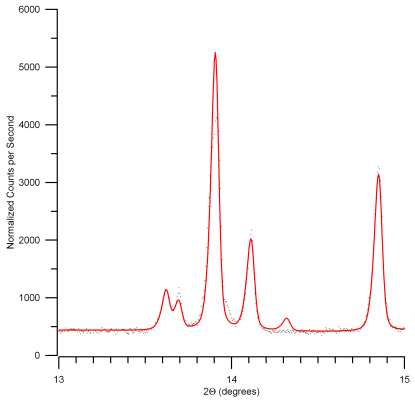

are a number of deficiencies. The most glaring of which is discrepancy between the calculated peak at 14.3° and the lack of any measured peak at that location. (Figure 4.20) Such a discrepancy is usually indicative of an incomplete structural model or in other words, the model is promising and close to correct but is deficient in some manner. The nature of this discrepancy was discovered when the Mn were allowed to have anisotropic thermal parameters, which showed a splitting of the octahedral Mn ion into a square pyramidal and octahedral coordinated Mn.

From this updated model, the structure was successfully refined with a constraint on the C-N distance in the cyano group. (Figure 4.21) Atomic positions are tabulated in Appendix B.10.

Figure 4.21: High-resolution synchrotron powder diffraction data (dots) and Rietveld fit (line) of the data for **4.4**. The lower trace is the differences, measured - calculated, plotted to the same vertical scale

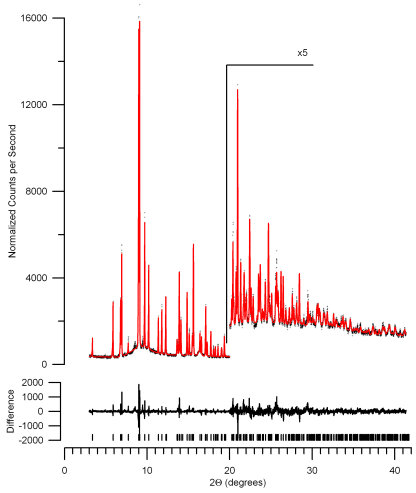

4.4.3 Crystal Structure of $Mn_5(CN)_{13}NMe_4$

4.4 is composed of layers that are bridged by cyanides. The layer consists of two unique Mn^{II} ions which are coordinated by cyanides. The first of these ions is on a site of $\overline{6}$ and is a 5-coordinated trigonal bipyramid. This coordination has not been previously seen for Mn^{II} coordinated by cyanides but has been observed in $YMnO_3$ [64]. The other Mn^{II} ion is on a site of

Table 4.4: Summary of crystallographic parameters for $Mn_5(CN)_{13}NMe_4$ (**4.4**)

Space group	$P\overline{6}2m$
a, Å	13.6090(5)
c, Å	5.7733(2)
α, °	90
β, °	90
γ, °	120
V, Å^3	926.00(2)
R_{wp}	7.10
R_{exp}	3.88

Figure 4.22: (a) Square pyramidal $Mn(CN)_5$, and (b) disordered between two orientation and can point either up or down . (c) A (square pyramidal)-(octahedral)-(square pyramidal) chain.

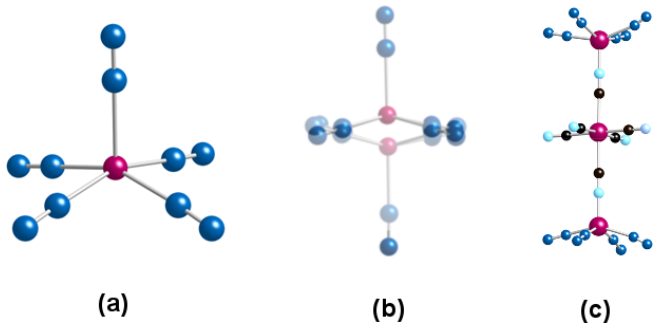

$m2m$ symmetry and is disordered between a 6-coordinated octahedral and a 5-coordinated square pyramidal in 1:2 ratio.(Figure 4.22) $Mn^{II}(CN)_5$ has not been observed previously and as with the trigonal bipyramid 5-coordinated Mn^{II} is quite rare, however this coordination has been seen for Cr^{II} in $(NEt_4)_8[Cr(CN)_5][Cr_2(CN)_9]_2MeCN$. [65] This square pyramidal feature can either point up or down and as such in this coordination the Mn^{II} will terminate this connection between layers, though the layers will still be connected by the other Mn^{II} site. This will lead to a (square pyramidal)-$(octahedral)_n$-(square pyramidal) chains.(Figure 4.22c) Due to the disordered nature of this site, the number of octahedral elements in the chain can vary, but from the occupancy of the site it can be concluded that on average there is one octahedral Mn^{II} per chain. The C and N along this chain are disordered as they are symmetry equivalent, as has been previously observed.[66–69] Each of these layers is constructred of triangular and pentagonal rings (Figure 4.23) that are made by cyanides bridging the trigonal bipyramidal and octahedral/square pyramidal Mn^{II} . This structure consists of a number of complex and unexpected features, most specifically the 5-coordinated Mn^{II},

Figure 4.23: Structure of **4.4** looking normal to the *ab* plane. The layers are connected by cyanides at the trigonal bipyramidal and disordered octahedral/square pyramidal sites. The octahedral/square pyramidal sites connect the layers, but terminate the connection at the square pyramidal.

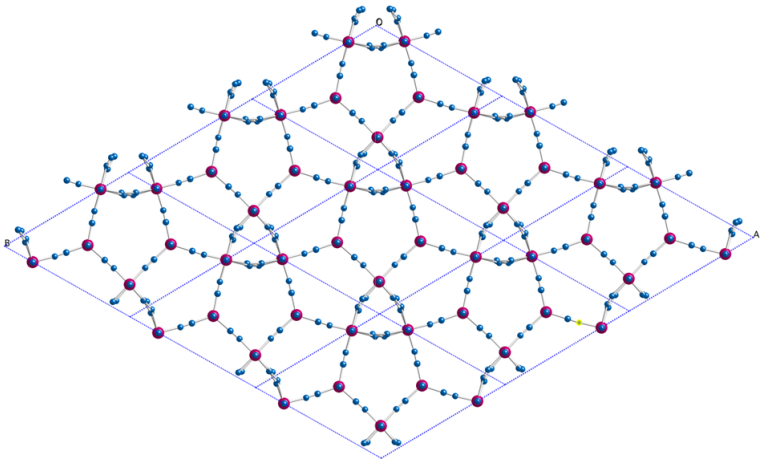

and highlights the ability of powder diffraction to determine unexpected and novel structural motifs.

4.4.4 Magnetism of $Mn_5(CN)_{13}NMe_4$

Magnetic measurements were performed by our collaborators, Christopher Kareis and Joel Miller, at University of Utah.

The magnetic susceptibility, χ, of $Mn_5(CN)_{13}NMe_4$ (**4.4**) is plotted as χ (4.24), χT and χ^{-1} (Figure 4.25). χ increases until it reaches a maximum at 12.6 K before decreasing upon further cooling, which is indicative of antiferromagnetic ordering.

Our collaborators found that at higher temperatures χT is well fit by the

Figure 4.24: Magnetic susceptibility, χ, for **4.4**

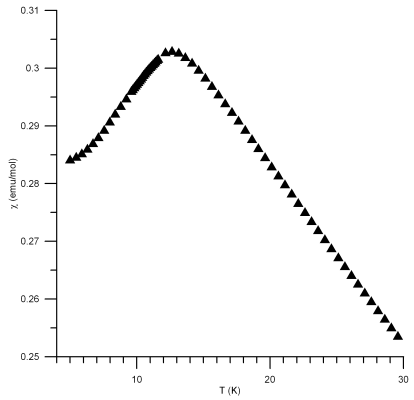

Figure 4.25: χT ($\times$) and χ^{-1} ($\bullet$) for **4.4**.

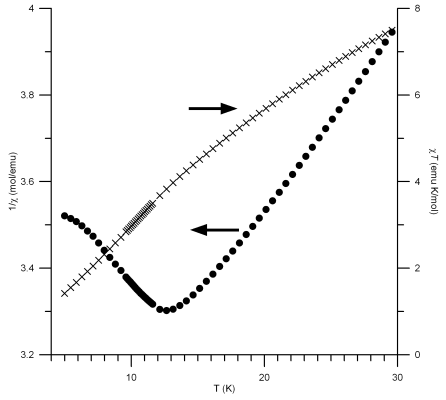

Curie-Weiss expression, $\chi \sim (T-\theta)^{-1}$, with θ = -35 K and C= 20.4 $\frac{\text{emu}}{\text{molK}}$, which correspond well with a model based on one low spin and four high spin Mn^{II} sites, which would have a g=2 value of C of 22.9 $\frac{\text{emu}}{\text{molK}}$. The fit is much poorer when all five Mn^{II} sites were assumed to be high spin (C = 31.9 $\frac{\text{emu}}{\text{molK}}$) or if two sites are low spin (C = 15.3 $\frac{\text{emu}}{\text{molK}}$). This corresponds to the octahedral site being low spin and all other Mn^{II} being high spin. Without knowledge of the structure of **4.4** interpretation of this magnetic data would not have been possible.

Chapter 5

Additional Projects

In the previous chapters of the dissertation, a number of materials have been described in detail. However those materials make up only a subset of the projects I have worked on while here at Stony Brook University. This section will include a listing and short description of the additional materials that have been structurally determined, none of which were known previously. Additionally, references on the compound correspond to their placement of publication, if any. Any compounds without a reference are currently in press.

5.1 Coordination Polymers and Magnetic Materials

A primary interest of our group is studies of materials that exhibit magnetic behavior, particularly coordination polymers. The main focus of my research has been structural characterization of these materials through the use of powder diffraction. Table 5.1 lists these compounds and the corresponding unit

cells.

Table 5.1: List of Additional Coordination Polymers and Magnetic Materials

Compound	Space Group	a (Å)	b (Å)	c (Å)	α (°)	β (°)	γ (°)
(TMEDA)Ni^{II}(benzene-1,2,4,5-tetrathiol)Ni^{II}(TMEDA) [a]	$P2_1/c$	8.272	10.656	14.656	90	105.40	90
(Bulm)Ni^{II}(benzene-1,2,4,5-tetrathiol)Ni^{II}(Bulm) [b]	$P2_1/c$	9.462	20.807	10.542	90	88.55	90
$CdBr_2$(1,2-bis(4'-pyridyl)ethylene) [70]	P-1	3.614	8.869	9.434	79.57	86.28	86.25
$NiBr_2(pyz)_2$ [c]	$I4/mmm$	7.060	7.060	11.312	90	90	90
$NiCl_2(pyz)_2$ [c]	$I4/mmm$	7.043	7.043	10.741	90	90	90
CoF_2(3-hydroxypyridine)$_4$	$Pccn$	7.402	14.689	18.320	90	90	90
$[Cu(pyz)_2(phpyo)_2](ClO_4)_2$ [c,d]	$C2/c$	34.567	9.485	9.886	90	102.76	90
$Ni(pyz)_2$(hexafluoroacetylacetonate)$_2$	$Pbca$	17.614	13.666	9.847	90	90	90
$Cu(pyz)_2(BF_4)_2$ [c]	$C2/m$	9.692	9.778	8.040	90	121.26	90
$Ni[N(CN)_2]_2$ (pyrimidine)$_2$ H_2O	$Pnma$	12.758	11.892	9.216	90	90	90
$(Ni(H_2O)_4$ $DMF_2)Br_2$ H_2O [e]	$C2/m$	21.900	7.071	5.925	90	77.06	90
$[Cu(pyz)_2$ $SiF_6]$ H_2O	$Cmmm$	6.871	16.122	8.220	90	90	90
$[Cu(pyz)_2$ $VF_6]$ (pyz) H_2O [c]	$I4/mcm$	9.708	9.708	16.423	90	90	90
Ag(Nicotinate)$_2$ [71]	$P2_1/n$	5.016	8.037	14.150	90	98.37	90
$Mn(CN)_2$ [66]	Pn-3m	6.149	6.149	6.149	90	90	90
$CoI_2(NCMe)_2$	$Cmcm$	8.689	11.380	10.671	90	90	90
$Cr(NCS)_2(NCMe)_2$	$P2_12_12_1$	9.090	9.167	12.690	90	90	90
$Fe(NCS)_2$TCNQ [f]	P-1	5.574	6.139	11.455	78.42	80.04	78.24
$Co(NCS)_2$	$C2/m$	10.560	3.725	6.166	90	105.86	90
$Fe(Cl)_2$ (2,2'-bipyridine)	P-1	8.241	8.442	8.759	110.45	105.35	94.12
$Fe(NCS)_2$ (2,2'-bipyridine)	$C2/c$	7.793	16.056	10.583	90	91.71	90
$Co(TCNE)(C_4(CN)_8)1/2$ [g]	$Cmmm$	14.234	17.253	7.291	90	90	90
$Co(C_4(CN)_8)(NCMe)_2$	$P2_1/c$	7.575	11.484	11.108	90	107.10	90
$Fe(C_4(CN)_8)(OCMe_2)_2$	$P2_1/c$	7.880	11.448	11.566	90	100.15	90
$Mn(C_4(CN)_8)(OCMe_2)_2$	$P2_1/c$	7.821	11.649	11.687	90	99.06	90
$Co(C_4(CN)_8)(OCMe_2)_2$	$P2_1/c$	7.919	11.388	11.483	90	100.56	90
$[Mn^{III}TPP][Me_2DCNQI]$ [h,i]	P-1	11.938	12.425	9.595	94.518	75.01	128.30
$FeCp^*_2$TCQMI [j,k]	$P2_1$	10.588	13.783	10.708	90	119.64	90
$FeCp^*_2$TCNQ [f,j] Room T metamagnetic phase	P-1	9.788	10.625	17.255	94.75	107.43	119.72
$CoSalenCl_2$ [l]	$P2_1/n$	12.202	8.500	18.334	90	105.40	90
KTCNE [g]	$C2/m$	12.942	7.576	15.080	90	96.540	90
RbTCNE [g]	$C2/m$	13.227	7.706	15.457	90	96.32	90
$[Co(NCS)_4][NMe_4]_2$	$C2/c$	24.643	11.307	24.933	90	94.73	90
$[Fe(NCMe)_6]SbF_6$	R-3	11.466	11.466	17.389	90	90	120
$[Mn(NCMe)_6]SbF_6$	R-3	11.391	11.391	16.760	90	90	120
$[Mn(TCNE)(NCMe)_2]PF_6$ [g]	$Cmcm$	7.142	15.878	14.994	90	90	90
$[Mn(TCNE)(NCMe)_2]SbF_6$ [g][72]	$Cmcm$	7.192	16.294	14.943	90	90	90
$[Mn(TCNE)(NCMe)_2]AsF_6$ [g]	$Cmcm$	7.159	16.036	14.972	90	90	90
$[Fe(TCNE)(NCMe)_2]SbF_6$ [g]	$Cmcm$	7.143	16.255	14.669	90	90	90

a TMEDA = Tetramethylethylenediamine
b Bulm = 1-Butylimidazole
c pyz = pyrazine
d phpyo = 4-phenyl-pyridine-N-oxide
e DMF = Dimethylformamide
f TCNQ = Tetracyanoquinodimethane
g TCNE = Tetracyanoethylene
h TPP = Tetraphenylporphinato
i Me_2DCNQI = 2,5-dimethyl-N,N'-dicyanoquinonediimine
j Cp^* = pentamethylcyclopentadienide
k TCQMI = N,7,7-tricyanoquinomethanimine
l Salen = N,N'-Ethylenebis(salicylimine)

5.2 Molecular Compounds

In magnetic materials, the organic ligand needs to be structurally characterized independently in order to understand its behavior in the magnetic compound. Additionally as mentioned previously, polymorphism (Section 2.1) is of particular interest and understanding the phase transitions in these polymorphic systems. Table 5.2 lists these compounds and the corresponding unit cells.

Table 5.2: List of Additional Molecular Compounds

Compound	Space Group	a (Å)	b (Å)	c (Å)	α (°)	β (°)	γ (°)
Propyphenazone form I[73]	Pc	10.852	7.415	8.843	90	107.49	90
Propyphenazone form II[73]	Cc	20.663	7.436	8.717	90	95.14	90
N-(3,5-dichloro-4-oxocyclohexa -2,5-dienylidene)cyanamide	$P2_1/n$	6.545	10.525	12.174	90	106.18	90
N-(3,5-di-tert-butyl-4-oxocyclohexa -2,5-dienylidene)cyanamide	$P2_1/n$	6.445	12.340	18.449	90	94.28	90
2-(4-oxocyclohexa- 2,5-dienylidene)malononitrile	$P2_1/n$	13.340	7.400	7.848	90	92.66	90
3,6-dihydro-1,2,4,5-tetrazine- 3,6-dicarboxamide	$P2_1/c$	9.119	5.063	6.695	90	88.492	90

5.3 Cocrystals

As mentioned in Section 2.2, cocrystals are a subject of much interest and research. Table 5.3 lists a number of a cocrystals that have been structurally determined with the use of powder diffraction. As these compounds generally do not diffract to high angle/low d-spacing, these compounds have been solved with simulated annealing. Unless otherwise noted the stoichiometry of the cocrystal is 1:1.

Table 5.3: A List of Additional Cocrystals

Compound	Space Group	a (Å)	b (Å)	c (Å)	α (°)	β (°)	γ (°)
Caffeine & Catechin	$P2_12_12_1$	5.034	12.559	34.143	90	90	90
Coumaric acid & Betaine	P-1	6.425	8.993	12.705	100.38	92.02	99.84
Coumaric acid & Isonicotinic acid	P-1	7.419	8.934	11.367	86.96	74.21	66.90
Gallic acid & Adenine	$P2_1/c$	7.966	6.332	24.848	90	96.21	90
Pentoxifylline & 1-hydroxy-2-napthoic acid	P-1	6.741	8.284	21.013	81.21	81.96	82.50
Pentoxifylline & Catechin	$P2_1$	13.263	5.272	19.524	90	96.11	90
4-hydroxybenzoic acid & 4-phenylpyridine [74]	$C2/c$	27.243	7.5516	19.480	90	131.101	90
3-hydroxybenzoic acid & 4-phenylpyridine (1:2) [74]	$P2_1/n$	9.3537	21.117	11.907	90	92.808	90
3-hydroxybenzoic acid & tetramethylpyrazine (2:3)[74]	$P2_1/c$	9.4644	17.734	10.9533	90	91.783	90
3-hydroxybenzoic acid & 4,4'-bipyridine[74]	P-1	8.2326	9.0509	10.4682	71.730	72.438	87.088
3-hydroxybenzoic acid & 1,2-bis(4-pyridyl)ethane[74]	P-1	8.0446	9.0984	11.307	97.187	91.531	91.106
4-hydroxybenzoic acid & 1,2-bis(4-pyridyl)ethene[74]	P-1	6.2043	7.106	18.615	92.987	94.266	103.892
3-hydroxybenzoic acid & trans-1,2-bis(4-pyridyl)ethene[74]	P-1	8.129	10.359	10.916	114.450	104.452	93.167
4-hydroxybenzoic acid & 1,2-bis(4-pyridine)ethane (2:1)[74]	$P2_1/c$	7.5869	23.943	12.5825	90	103.786	90
3-hydroxypyridine & isophthalic acid[74]	$P2_1/n$	10.060	10.954	10.371	90	99.279	90
L-ascorbic acid & nicotinic acid[74]	$P2_12_12_1$	5.394	8.173	28.390	90	90	90
N'-(propan-2-ylidene) nicotinohydrazide & 2,4-dihydroxybenzoic acid	$P2_1/a$	8.851	22.724	8.5813	90	84.24	90
Diflunisal & Hexamethylenetetramine	$P2_1/c$	10.127	16.591	12.464	90	122.04	90

5.4 Inorganic Compounds

Inorganic compounds are generally defined as compounds without C-C bonds (though the difference between inorganic and organic is not well defined). While they have not been a focus of my research, a number of such compounds have been analyzed with powder diffraction. The majority of these compounds have been accidental in nature and often have resulted in new polymorphs of the initial reactants. Table 5.4 lists these compounds and the corresponding unit cells.

Table 5.4: A list of additional Inorganic Compounds

Compound	Space Group	a (Å)	b (Å)	c (Å)	α (°)	β (°)	γ (°)
$Na_4CrO(PO_4)_2$	*Ibam*	14.462	15.392	7.086	90	90	90
CuF_2	$C2/m$	5.283	3.186	5.075	90	112.78	90
K_4FeCl_6	$R\text{-}3c$	11.970	11.970	14.803	90	90	120

Bibliography

[1] Herbert Hauptman. *Science*, 233(4760):178–183, 1986.

[2] W.I.F. David. *Structure Determination from Powder Diffraction Data*. International Union of Crystallography Monographs on Crystallography. Oxford University Press, 2002.

[3] P A Goddard, J Singleton, P Sengupta, R D McDonald, T Lancaster, S J Blundell, F L Pratt, S Cox, N Harrison, J L Manson, H I Southerland, and J A Schlueter. *New Journal of Physics*, 10(8):083025, 2008.

[4] Joel S. Miller and Peter W. Stephens. *Transactions of the American Crystallographic Association*, 2010.

[5] B.D. Cullity. *Elements of x-ray diffraction*. Addison-Wesley series in metallurgy and materials. Addison-Wesley Pub. Co., 1978.

[6] J. W. Visser. *Journal of Applied Crystallography*, 2(3):89–95, 1969.

[7] A. A. Coelho. *Journal of Applied Crystallography*, 36(1):86–95, 2003.

[8] T Hahn, editor. *International Tables for X-ray Crystallography Vol. A, Space-group Symmetry*, volume Vol. A. Kluwer Academic Publishers, 2002.

[9] G.S. Pawley. *J. Appl. Cryst.*, 14:357–361, 1981.

[10] W. I. F. David, K Shankland, J. van de Streek, E. Pidcock, W. D. S. Motherwell, and J. C. Cole. *J. Appl. Cryst.*, 39:910–915, 2006.

[11] Kenneth D. M. Harris and Eugene Y. Cheung. *Chem. Soc. Rev.*, 33: 526–538, 2004.

[12] William I. F. David, Kenneth Shankland, Kenneth Shankland, and Norman Shankland. *Chem. Commun.*, pages 931–932, 1998.

[13] S. Kirkpatrick, C. D. Gelatt, and M. P. Vecchi. *Science*, 220(4598):671–680, 1983.

[14] A. Coelho. Topas Academic. TOPAS-Academic is available online at www.topas-academic.net., 2007.

[15] G. Oszlanyi and A. Suto. *Acta Cryst. A*, 64:123–134, 2008.

[16] H.M. Rietveld. *J. App. Cryst*, 2:65, 1969.

[17] J. Bernstein. *Polymorphism in Molecular Crystals*. International Union of Crystallography. Oxford University Press, 2008.

[18] M. Kuhnert-Brandsttter and H. W. Sollinger. *Microchimica Acta.*, 3: 137–149, 1990.

[19] Matthias Zeller, Jake L. Stouffer, Virgil C. Solomon, and Larry S. Curtin. *Acta Crystallographica Section C*, 67(10):o397–o404, 2011.

[20] T. Wieckowski and T.M. Krygowski. *Croat.Chem.Acta*, 58:5, 1985.

[21] S. J. Grabowski and T. M. Krygowski. *Acta Crystallographica Section C*, 41(8):1224–1226, 1985.

[22] P. Prince, F. R. Fronczek, and R. D. Gandour. *Acta Crystallographica Section C*, 47(4):895–898, 1991.

[23] Andrew D. Bond. *CrystEngComm*, 9:833–834, 2007.

[24] Gautam R. Desiraju. *CrystEngComm*, 5:466–467, 2003.

[25] Jack D. Dunitz. *CrystEngComm*, 5:506–506, 2003.

[26] K.R. Seddon and M. Zaworotko. *Crystal Engineering: The Design and Application of Functional Solids*. Number v. 539 in NATO science series: Mathematical and physical sciences. Kluwer Academic, 1999.

[27] Marcel Hoffman and Jeffrey A. Lindeman. Chapter 14 co-crystals: Commercial opportunities and patent considerations. In *Pharmaceutical Salts and Co-crystals*, pages 318–329. The Royal Society of Chemistry, 2012.

[28] Arijit Mukherjee and Gautam R. Desiraju. *Chem. Commun.*, 47:4090–4092, 2011.

[29] Xuefeng Mei and Christian Wolf. *Crystal Growth & Design*, 4(6):1099–1103, 2004.

[30] Nathaniel L. Rosi, Juergen Eckert, Mohamed Eddaoudi, David T. Vodak, Jaheon Kim, Michael O'Keeffe, and Omar M. Yaghi. *Science*, 300(5622): 1127–1129, 2003.

[31] David Britt, Hiroyasu Furukawa, Bo Wang, T. Grant Glover, and Omar M. Yaghi. *Proceedings of the National Academy of Sciences*, 106 (49):20637–20640, 2009.

[32] Robert Fairchild. *Functionalization and applications of the pentamethylcyclopentadienyl ruthenium moiety*. PhD thesis, Georgetown University, 2008.

[33] S.J. Gregg and K.S.W. Sing. *Adsorption, surface area, and porosity*. Academic Press, 1991.

[34] Anthony L. Spek. *Acta Crystallographica Section D*, 65(2):148–155, 2009.

[35] K. Momma and F. Izumi. *J. Appl. Cryst.*, 41:653–658, 2008.

[36] J.A. Real, A.B. Gaspar, V. Niel, and M.C. Muoz. *Coord. Chem. Rev.*, 236:121, 2003.

[37] L. Palatinus and G. Chapuis. *J. Appl. Cryst.*, 40:786–790, 2007.

[38] J. W. Larson and T. B. McMahon. *Journal of the American Chemical Society*, 104(21):5848–5849, 1982.

[39] Jamie L. Manson, Marianne M. Conner, John A. Schlueter, Tom Lancaster, Stephen J. Blundell, Michael L. Brooks, Francis L. Pratt, Thomas Papageorgiou, Andreas D. Bianchi, Jochen Wosnitza, and Myung-Hwan Whangbo. *Chem. Commun.*, 47:4894–4896, 2006.

[40] Jamie L. Manson, John A. Schlueter, Kylee A. Funk, Heather I. Southerland, Brendan Twamley, Tom Lancaster, Stephen J. Blundell, Peter J. Baker, Francis L. Pratt, John Singleton, Ross D. McDonald, Paul A. Goddard, Pinaki Sengupta, Cristian D. Batista, Letian Ding, Changhoon Lee, Myung-Hwan Whangbo, Isabel Franke, Susan Cox, Chris Baines, and Derek Trial. *J. Am. Chem. Soc.*, 131:6733–6747, 2009.

[41] E. Cimr, S. A. Zvyagin, R. Beyer, M. Uhlarz, M. Ozerov, Y. Skourski, J. L. Manson, J. A. Schlueter, and J. Wosnitza. *Phys. Rev. B.*, 81:064422, 2010.

[42] Jamie L. Manson, Saul H. Lapidus, Peter W. Stephens, Peter K. Peterson, Kimberly E. Carreiro, Heather I. Southerland, Tom Lancaster, Stephen J. Blundell, Andrew J. Steele, Paul A. Goddard, Francis L. Pratt, John Singleton, Yoshimitsu Kohama, Ross D. McDonald, Rico E. Del Sesto, Nickolaus A. Smith, Jesper Bendix, Sergei A. Zvyagin, Jinhee Kang, Changhoon Lee, Myung-Hwan Whangbo, Vivien S. Zapf, and Alex Plonczak. *Inorganic Chemistry*, 50(13):5990–6009, 2011.

[43] O. Kahn. *Molecular Magnetism*. VCH Publishers, Weinheim, 1993.

[44] S.J.L. Billinge and F. Thorpe. *Local Structure from Diffraction*. Fundamental Materials Research. Plenum Press, 1998.

[45] Jamie L Manson, Kimberly E Carreiro, Saul L Lapidus, Peter Stephens, Paul A Goddard, Rico Del Sesto, Jesper Bendix, Saman Ghannadzadeh, Isabel Franke, John Singleton, Tom Lancaster, Johannes Moeller, Peter J Baker, Francis L Pratt, Stephen J Blundell, Jinhee Kang, Changhoon Lee, and Myung-Hwan Whangbo. *Dalton Trans.*, Accepted.

[46] F. H. Allen. *Acta Crystallogr.*, B58:380–388, 2002.

[47] H. J. Buser, D. Schwarzenbach, W. Petter, and A. Ludi. *Inorg. Chem.*, 16:2704–2710, 1977.

[48] S. Ferlay, T T. Mallah, R. Ouahes, P. Veillet, and M. Verdaguer. *Nature*, 378:701, 1995.

[49] S. M. Holmes and G.S. Girolami. *J. Am. Chem. Soc.*, 121:5593, 1999.

[50] Melvin B. Robin. *Inorganic Chemistry*, 1(2):337–342, 1962.

[51] D.M.P. Mingos. *Essential Trends in Inorganic Chemistry*. Oxford University Press, New York, 1998.

[52] J.-H. Her, P.W. Stephens, C.M. Kareis, J.G. Moore, K.S. Min, J.-W. Park, G. Bali, B.S. Kennon, and J.S. Miller. *Inorg. Chem.*, 49:1524, 2010.

[53] A. Tullberg and N. Vannerberg. *Acta Chem. Scand., Ser. A*, 28:551, 1974.

[54] A. Tullberg and N. Vannerberg. *Acta Chem. Scand., Ser. A*, 25:343, 1971.

[55] G. W. Beall, W. O. Milligan, J. Korp, and I. Bernal. *Inorg. Chem.*, 16: 2715, 1977.

[56] Julie L. Heinrich, Jennifer J. Sokol, Allan G. Hee, and Jeffrey R. Long. *Journal of Solid State Chemistry*, 159(2):293 – 301, 2001.

[57] A. M. Glazer. *Acta Crystallographica Section B*, 28(11):3384–3392, 1972.

[58] Mois I. Aroyo, Asen Kirov, Cesar Capillas, J. M. Perez-Mato, and Hans Wondratschek. *Acta Crystallographica Section A*, 62(2):115–128, 2006.

[59] Branton J. Campbell, Harold T. Stokes, David E. Tanner, and Dorian M. Hatch. *Journal of Applied Crystallography*, 39(4):607–614, 2006.

[60] Christopher M. Kareis, Saul H. Lapidus, Jae-Hyuk Her, Peter W. Stephens, and Joel S. Miller. *Journal of the American Chemical Society*, 134(4):2246–2254, 2012.

[61] Angela Altomare, Rocco Caliandro, Mercedes Camalli, Corrado Cuocci, Carmelo Giacovazzo, Anna Grazia Giuseppina Moliterni, and Rosanna Rizzia. *J. Appl. Cryst.*, 37:1025–1028, 2004.

[62] Nicole E. Chakov, Sheng-Chiang Lee, Andrew G. Harter, Philip L. Kuhns, Arneil P. Reyes, Stephen O. Hill, N. S. Dalal, Wolfgang Wernsdorfer, Khalil A. Abboud, and George Christou. *Journal of the American Chemical Society*, 128(21):6975–6989, 2006.

[63] Jae-Hyuk Her, Peter W. Stephens, Christopher M. Kareis, Joshua G. Moore, and Joel S. Miller. *Angewandte*, 49:77773, 2010.

[64] Andrew E. Smith, Hiroshi Mizoguchi, Kris Delaney, Nicola A. Spaldin, Arthur W. Sleight, and M. A. Subramanian. *Journal of the American Chemical Society*, 131(47):17084–17086, 2009.

[65] Kendric J. Nelson, Ian D. Giles, William W. Shum, Atta M. Arif, and Joel S. Miller. *Angewandte Chemie International Edition*, 44(20):3129–3132, 2005.

[66] Christopher M. Kareis, Saul H. Lapidus, Peter W. Stephens, and Joel S. Miller. *Inorg. Chem.*, 51:30463050, 2012.

[67] B. F. Hoskins and R. Robson. *J. Am. Chem. Soc.*, 112:1546, 1990.

[68] D. J. Williams, D. E. Partin, F. J. Lincoln, J. Kouvetakis, and M. O'Keefe. *J. Solid State Chem.*, 134:164, 1997.

[69] O. Reckeweg and A. Simon. *Z. Naturforsch.*, 57b:895, 2002.

[70] Mangayarkarasi Nagarathinam, Anjana Chanthapally, Saul H. Lapidus, Peter W. Stephens, and Jagadese J. Vittal. *Chem. Commun.*, 48:2585–2587, 2012.

[71] Jamie L. Manson, Toby J. Woods, Saul H. Lapidus, Peter W. Stephens, Heather I. Southerland, Vivien S. Zapf, John Singleton, Paul A. Goddard, Tom Lancaster, Andrew J. Steele, and Stephen J. Blundell. *Inorganic Chemistry*, 51(4):1989–1991, 2012.

[72] Christopher Olson, Christopher L. Heth, Saul H. Lapidus, Peter W. Stephens, Gregory J. Halder, and Konstantin Pokhodnya. *The Journal of Chemical Physics*, 135(2), 2011.

[73] Andreas Lemmerer, Joel Bernstein, Ulrich J. Griesser, Volker Kahlenberg, Daniel M. Tbbens, Saul H. Lapidus, Peter W. Stephens, and Catharine Esterhuysen. *Chemistry: A European Journal*, 17(48), 2011.

[74] Saul H. Lapidus, Peter W. Stephens, Kapildev K. Arora, Tanise R. Shattock, and Michael J. Zaworotko. *Crystal Growth & Design*, 10(10):4630–4637, 2010.

[75] J. Samuel Smart. *Amer. J. Phys.*, 23:356, 1955.

Appendix A

Derivation of the Néel Hyperbolic Equation

The following derivation is based upon the derivation by J. Smart. [75] This derivation will be done in a system consisting of two sublattice but it can be trivially generalized to any number of sublattices. Consider a lattice consisting of two types of sites A and B then the total field at each site will be given by:

$$H_a = H_0 + \gamma_{aa} M_a + \gamma_{ab} M_b$$
$$H_b = H_0 + \gamma_{ab} M_a + \gamma_{bb} M_b$$

where H_0 is the applied field, M_i is the magnetization of site i and the γ's are the molecule field coefficients. It is useful to define a number of things for convenience:

$$\alpha = \frac{\gamma_{aa}}{\gamma_{ab}}$$
$$\beta = \frac{\gamma_{bb}}{\gamma_{ab}}$$
$$\sigma_a = \frac{M_a}{\lambda N g \mu_B S}$$
$$\sigma_b = \frac{M_b}{\nu N g \mu_B S}$$

where N is the number of magnetic ions per volume; λ and ν are the fraction of magnetic ions on the A and B sites, respectively; σ_i is the reduced magnetism

for each site. Under these new variables, equations A.1 becomes:

$$H_a = H_0 + Ng\mu_B S\gamma_{ab}[\lambda\alpha\sigma_a + \nu\sigma_b]$$
$$H_b = H_0 + Ng\mu_B S\gamma_{ab}[\lambda\sigma_a + \nu\beta\sigma_b]$$

The reduced magnetism can also be written as:

$$\sigma_a = B_s(\frac{g\mu_B S H_a}{kT})$$
$$\sigma_b = B_s(\frac{g\mu_B S H_b}{kT})$$

where the Brillouin function $B_S(x) = \frac{2S+1}{2S}\coth\frac{2S+1}{2S}z - \frac{1}{2S}\coth\frac{z}{2S}$. If the high temperature limit is considered, the Brillouin function can be written as $B_S(x) = \frac{x}{3}(1+\frac{1}{S})$. From this the σ's can be rewritten as $\sigma_i = \frac{g\mu_B S H_i(S+1)}{3kT}$ and thus equations A.1 can be rewritten as:

$$H_a = H_0 + C\gamma_{ab}[\lambda\alpha\frac{H_a}{T} + \nu\frac{H_b}{T}]$$
$$H_b = H_0 + C\gamma_{ab}[\lambda\frac{H_a}{T} + \nu\beta\frac{H_b}{T}]$$

where C is the Curie constant, $C = \frac{Ng^2\mu_B^2}{3k}S(S+1)$. This set of equations can be solved and result in:

$$H_a = \frac{T^2 + (1-\alpha)\gamma_{ab}\lambda T}{T^2 - (\nu\beta+\lambda\alpha)C\gamma_{ab}T + (\alpha\beta-1)\nu\lambda C^2\gamma_{ab}^2}H_0$$
$$H_b = \frac{T^2 + (1-\beta)\gamma_{ab}\nu T}{T^2 - (\nu\beta+\lambda\alpha)C\gamma_{ab}T + (\alpha\beta-1)\nu\lambda C^2\gamma_{ab}^2}H_0$$

From this the total magnetization can be found:

$$M = M_a + M_b = \frac{C[T + \lambda\nu C\gamma_{ab}(2-\alpha-\beta)]}{T^2 - (\nu\beta+\lambda\alpha)C\gamma_{ab}T + (\alpha\beta-1)\nu\lambda C^2\gamma_{ab}^2}H_0 \qquad \text{(A.1)}$$

Using that $\chi = \frac{dM}{dH}$,

$$\frac{1}{\chi} = \frac{T^2 - (\nu\beta+\lambda\alpha)C\gamma_{ab}T + (\alpha\beta-1)\nu\lambda C^2\gamma_{ab}^2}{C[T + \lambda\nu C\gamma_{ab}(2-\alpha-\beta)]} \qquad \text{(A.2)}$$

which can be further be written as the Néel hyperbolic equation (equation 4.1) $\frac{1}{\chi} = \frac{T-\theta}{C} - \frac{\zeta}{T-\theta'}$ where $\theta = C\gamma_{ab}\lambda\nu[2 + \frac{\lambda\alpha}{\nu} + \frac{\nu\beta}{\lambda}]$, $\theta' = -C\gamma_{ab}\lambda\nu[2 - \alpha - \beta]$ and $\zeta = C\gamma_{ab}^2\lambda\nu[\lambda(1-\alpha) - \nu(1-\beta)]^2$.

Appendix B

Atomic Positions

B.1 3,4-Dinitrobenzoic Acid

B.1.1 Form I

Table B.1 lists fractional atomic coordinates for form I of 3,4-Dinitrobenzoic Acid.

Table B.1: Atomic coordinates for form I of 3,4-Dinitrobenzoic Acid

Atom	x	y	z	Atom	x	y	z
C1	-0.1083	-0.5442	0.8601	C6a	-1.027	-0.2358	0.9808
C2	-0.1276	-0.6095	0.8044	C5a	-1.1834	-0.1691	1.0034
C3	0.023	-0.6736	0.7705	C4a	-1.1817	-0.0982	1.0575
C4	0.1929	-0.6725	0.7924	C3a	-1.0236	-0.094	1.0889
C5	0.2122	-0.6072	0.8481	C2a	-0.8672	-0.1607	1.0663
C6	0.0616	-0.543	0.882	C1a	-0.8689	-0.2316	1.0122
C7	-0.2719	-0.4745	0.8969	C7a	-0.699	-0.304	0.9876
O1	-0.2538	-0.4144	0.9444	O1a	-0.7005	-0.3669	0.9397
O2	-0.4235	-0.4776	0.8795	O2a	-0.5588	-0.3003	1.0154
O3	-0.0309	-0.7143	0.6449	O5a	-1.3621	0.0561	1.0544
O4	0.0185	-0.8303	0.7276	O6a	-1.4738	-0.051	1.129
O5	0.3437	-0.7878	0.6984	O4a	-1.165	0.0208	1.185
O6	0.497	-0.751	0.7841	O3a	-0.877	0.0054	1.1563
N1	0.0023	-0.7434	0.7109	N2a	-1.3488	-0.0269	1.0817
N2	0.3538	-0.741	0.7562	N1a	-1.0217	-0.0182	1.1467
H2	-0.2454	-0.6103	0.7892	H5a	-1.2931	-0.172	0.9816
H5	0.33	-0.6064	0.8633	H2a	-0.7575	-0.1578	1.0881
H6	0.075	-0.4977	0.9207	H6a	-1.0282	-0.2849	0.9432
C1b	0.936	-0.044	0.6434	C1c	-0.5016	0.738	0.5214
C2b	0.9947	-0.1365	0.672	C2c	-0.4516	0.6654	0.5757
C3b	0.8702	-0.1886	0.715	C3c	-0.5601	0.595	0.5971
C4b	0.6869	-0.1481	0.7293	C4c	-0.7186	0.5973	0.5642
C5b	0.6283	-0.0556	0.7007	C5c	-0.7686	0.67	0.5099
C6b	0.7528	-0.0035	0.6578	C6c	-0.6601	0.7403	0.4885
C7b	1.0714	0.0126	0.5968	C7c	-0.3836	0.8146	0.4981
O2b	1.2356	-0.0135	0.5978	O1c	-0.4399	0.8863	0.4591
O1b	1.0176	0.0848	0.5578	O2c	-0.2312	0.8052	0.5182
O3b	1.0752	-0.305	0.7742	O4c	-0.6023	0.5121	0.7195
O4b	0.8423	-0.3518	0.7421	O3c	-0.3667	0.4583	0.6386
O5b	0.581	-0.2393	0.8402	O6c	-0.9986	0.5459	0.6087
O6b	0.4166	-0.2143	0.748	O5c	-0.7664	0.436	0.5843
N1b	0.9328	-0.2875	0.7455	N1c	-0.5066	0.5173	0.6551
N2b	0.5538	-0.2038	0.7751	N2c	-0.8346	0.522	0.587
H2b	1.1218	-0.1646	0.6621	H2c	-0.3416	0.6638	0.5985
H5b	0.5012	-0.0275	0.7106	H5c	-0.8786	0.6715	0.4871
H6b	0.7121	0.0607	0.6379	H6c	-0.6948	0.7908	0.4508

Table B.2: Atomic coordinates for form II of 3,4-Dinitrobenzoic Acid

Atom	x	y	z	Atom	x	y	z
C1	-0.8602	-0.0232	0.7464	C6a	-0.6728	-0.6521	0.9792
C2	-0.7796	-0.0599	0.8331	C5a	-0.5688	-0.6924	0.9211
C3	-0.8838	-0.0886	0.9002	C4a	-0.65	-0.7331	0.8378
C4	-1.0687	-0.0806	0.8806	C3a	-0.8353	-0.7335	0.8125
C5	-1.1494	-0.0438	0.7939	C2a	-0.9394	-0.6932	0.8705
C6	-1.0451	-0.0151	0.7268	C1a	-0.8581	-0.6525	0.9538
C7	-0.7525	0.0065	0.6771	C7a	-0.9656	-0.6108	1.0138
O1	-0.8268	0.0445	0.5989	O2a	-1.1386	-0.6116	0.9906
O2	-0.5809	-0.0046	0.6926	O1a	-0.8897	-0.5724	1.0912
O3	-0.6752	-0.096	1.0484	O6a	-0.4105	-0.7445	0.748
O4	-0.8496	-0.192	1.0132	O5a	-0.5763	-0.8432	0.7529
O5	-1.129	-0.1043	1.0427	O3a	-1.0421	-0.8229	0.7317
O6	-1.3224	-0.1434	0.9207	O4a	-0.8731	-0.7667	0.6423
N1	-0.7982	-0.1277	0.9923	N2a	-0.5396	-0.776	0.7762
N2	-1.1794	-0.1111	0.9519	N1a	-0.9216	-0.7767	0.724
H2	-0.6524	-0.0654	0.8466	H5a	-0.4414	-0.6922	0.9385
H5	-1.2766	-0.0383	0.7804	H2a	-1.0668	-0.6934	0.8531
H6	-1.1006	0.0102	0.6672	H6a	-0.617	-0.6241	1.0365

B.1.2 Form II

Table B.2 lists fractional atomic coordinates for form II of 3,4-Dinitrobenzoic Acid.

B.2 m-Hydroxybenzoic Acid and Acridine (3:2)

Tables B.3 and B.4 list fractional atomic coordinates for the cocrystal m-Hydroxybenzoic Acid and Acridine (3:2).

Table B.3: Atomic coordinates for m-Hydroxybenzoic Acid and Acridine (3:2)]

Atom	x	y	z	Atom	x	y	z
C1	-0.1992	-0.6714	0.7659	O7	0.3683	0.1777	-1.6583
C2	-0.247	-0.6934	0.9042	O8	0.2329	0.1895	-1.9098
C3	-0.3401	-0.734	0.8576	O9	-0.0507	0.318	-1.7017
C4	-0.3855	-0.7527	0.6728	H16	0.0888	0.2666	-1.8456
C5	-0.3378	-0.7307	0.5345	H18	0.0118	0.2872	-1.3653
C6	-0.2446	-0.69	0.5811	H19	0.1635	0.2254	-1.2207
C7	-0.1029	-0.6293	0.8141	H20	0.2778	0.1842	-1.3885
O1	-0.0291	-0.6354	0.9703	H7	0.413	0.1616	-1.7239
O2	-0.0921	-0.5881	0.7054	H9	-0.0653	0.3261	-1.8238
O3	-0.3837	-0.7541	0.9839	C8	-0.6347	-0.9373	-0.119
H1	0.0305	-0.6093	1.0001	C9	-0.6569	-0.9491	-0.3097
H2a	-0.2179	-0.6814	1.0227	C10	-0.7294	-0.9985	-0.391
H3	-0.4434	-0.7801	0.9541	C11	-0.7797	-1.0361	-0.2815
H4	-0.4452	-0.7787	0.643	C12	-0.7576	-1.0243	-0.0907
H5	-0.3669	-0.7426	0.4161	C13	-0.6851	-0.9749	-0.0094
H6a	-0.2141	-0.6759	0.4925	C14	-0.5597	-0.8862	-0.0349
C15	0.1959	0.2209	-1.6354	O6	-0.7496	-1.0093	-0.5651
C16	0.1034	0.2586	-1.7236	O4	-0.5244	-0.882	0.1419
C17	0.0337	0.2837	-1.6213	O5	-0.5303	-0.8472	-0.1331
C18	0.0564	0.2711	-1.4308	H9a	-0.6246	-0.925	-0.3799
C19	0.1489	0.2334	-1.3427	H11	-0.8262	-1.0678	-0.3335
C20	0.2186	0.2083	-1.445	H12	-0.7898	-1.0484	-0.0205
C21	0.268	0.1949	-1.7412	H13	-0.6709	-0.9674	0.1128

Table B.4: Atomic coordinates for m-Hydroxybenzoic Acid and Acridine (3:2)]

Atom	x	y	z	Atom	x	y	z
H6	-0.796	-1.0409	-0.6172	H46	-0.4537	0.4929	0.6592
C37	-0.8727	0.6479	0.7344	H2	-0.5817	0.5766	0.7152
C38	-0.9631	0.6056	0.6815	C32	0.6401	0.8348	0.0104
C39	-0.9451	0.5437	0.628	C31	0.5456	0.8743	-0.0413
C40	-0.8368	0.5242	0.6273	C30	0.557	0.937	-0.0952
C35	-0.7464	0.5666	0.6802	C29	0.663	0.9602	-0.0974
C36	-0.7644	0.6285	0.7337	C34	0.7575	0.9207	-0.0457
C42	-0.7104	0.4429	0.5731	C33	0.7461	0.858	0.0082
C47	-0.62	0.4852	0.626	C27	0.7804	1.046	-0.1535
C41	-0.8188	0.4624	0.5738	C22	0.875	1.0065	-0.1018
C43	-0.6924	0.381	0.5196	C28	0.6744	1.0228	-0.1513
C44	-0.584	0.3615	0.519	C26	0.7919	1.1086	-0.2075
C45	-0.4936	0.4039	0.5718	C25	0.8979	1.1318	-0.2097
C46	-0.5116	0.4658	0.6253	C24	0.9924	1.0923	-0.158
N2	-0.6385	0.5487	0.6809	C23	0.981	1.0296	-0.104
H37	-0.8843	0.6876	0.7686	N1	0.8632	0.9422	-0.0465
H38	-1.0326	0.6181	0.6819	H32	0.6328	0.7947	0.045
H39	-1.003	0.5166	0.5941	H31	0.4777	0.8595	-0.0399
H36	-0.7065	0.6556	0.7676	H30	0.4964	0.9623	-0.1283
H41	-0.8767	0.4352	0.5399	H33	0.8067	0.8327	0.0413
H43	-0.7503	0.3539	0.4858	H28	0.6139	1.0481	-0.1845
H44	-0.5725	0.3219	0.4847	H26	0.7313	1.134	-0.2406
H45	-0.4242	0.3914	0.5714	H25	0.9052	1.172	-0.2442

Table B.5: Atomic coordinates for the partially hydrated phase of $Cd_{0.5}$[Cp*Ru(η^6-isophthalate)]

Atom	x	y	z	Atom	x	y	z
Cd1	0.3072	0.3602	0.7156	C17	0.589	0.716	1.1412
Cd2	-0.9292	-0.1577	-0.7641	C18	0.4339	0.4789	0.8826
Ow1	0.4993	0.7094	0.3415	H11	0.4282	0.6798	1.1538
Ow2	0.5761	0.3264	0.7399	H12	0.3015	0.5792	1.0674
Ru1	0.3765	0.6649	0.9591	H13	0.304	0.4899	0.9468
Ru2	-0.1263	-0.4897	0.421	H15	0.5601	0.6016	0.9991
Ru3	-0.3162	0.045	-0.404	H61	0.3383	0.8774	1.0366
Ru4	-0.1893	0.6563	-0.0982	H62	0.4343	0.8528	1.0573
O1	0.596	0.7513	1.213	H63	0.384	0.9219	0.9886
O2	0.6475	0.7326	1.114	H71	0.5048	0.8534	0.941
O3	0.3712	0.4234	0.8416	H72	0.5203	0.7673	0.91
O4	0.498	0.4882	0.8614	H73	0.4701	0.8364	0.8413
C1	0.3391	0.8034	0.9371	H81	0.4086	0.6862	0.7538
C2	0.3894	0.7808	0.8878	H82	0.357	0.6099	0.7613
C3	0.3365	0.7154	0.8203	H83	0.3067	0.6789	0.6927
C4	0.2535	0.6975	0.8279	H91	0.1827	0.607	0.7336
C5	0.2551	0.7519	0.9002	H92	0.1699	0.5981	0.8167
C6	0.3779	0.8709	1.0127	H93	0.1197	0.6672	0.748
C7	0.4806	0.8128	0.8959	H101	0.1392	0.7251	0.9083
C8	0.354	0.6677	0.7497	H102	0.2177	0.7483	0.9996
C9	0.1731	0.6361	0.7762	H103	0.1674	0.8173	0.9309
C10	0.1879	0.7617	0.9387	O1a	-0.0898	-0.5541	0.6709
C11	0.4292	0.6465	1.1089	O2a	0.0498	-0.5853	0.6941
C12	0.3497	0.5834	1.0546	O3a	-0.2644	-0.2876	0.4504
C13	0.3513	0.5274	0.979	O4a	-0.1938	-0.219	0.3857
C14	0.4324	0.5344	0.9576	C1a	-0.1536	-0.5892	0.3152
C15	0.5119	0.5975	1.0118	C2a	-0.169	-0.6262	0.3874
C16	0.5103	0.6535	1.0875	C3a	-0.2432	-0.5782	0.3913

B.3 $Cd_{0.5}$[Cp*Ru(η^6-isophthalate)]

B.3.1 Partial Hydrate

Tables B.5, B.6 and B.7 lists fractional atomic coordinates for the partially hydrated phase of $Cd_{0.5}$[Cp*Ru(η^6-isophthalate)].

Table B.6: Atomic coordinates for the partially hydrated phase of $Cd_{0.5}$[Cp*Ru(η^6-isophthalate)]

Atom	x	y	z	Atom	x	y	z
C4a	-0.2736	-0.5115	0.3214	H91a	-0.376	-0.4469	0.3292
C5a	-0.2183	-0.5183	0.2743	H92a	-0.321	-0.3895	0.3008
C6a	-0.0794	-0.6264	0.295	H93a	-0.3902	-0.4504	0.2332
C7a	-0.123	-0.7008	0.4531	H101a	-0.2627	-0.4249	0.1785
C8a	-0.2889	-0.5871	0.452	H102a	-0.1617	-0.442	0.2158
C9a	-0.3479	-0.4424	0.2932	H103a	-0.2309	-0.503	0.1483
C10a	-0.2184	-0.4667	0.1961	O1b	-0.2472	-0.0047	-0.6202
C11a	-0.0385	-0.4847	0.5724	O2b	-0.3674	-0.0795	-0.6369
C12a	0.0222	-0.4951	0.5254	O3b	-0.2079	0.2881	-0.3071
C13a	0.009	-0.4344	0.4468	O4b	-0.1174	0.2352	-0.3584
C14a	-0.0649	-0.3634	0.4153	C1b	-0.34	-0.0847	-0.363
C15a	-0.1255	-0.3529	0.4623	C2b	-0.2465	-0.0803	-0.351
C16a	-0.1124	-0.4136	0.5408	C3b	-0.1971	-0.0132	-0.2842
C17a	-0.0254	-0.5447	0.6502	C4b	-0.2602	0.0239	-0.2549
C18a	-0.1987	-0.2826	0.431	C5b	-0.3485	-0.0203	-0.3036
H16a	-0.1484	-0.4074	0.5687	C6b	-0.4084	-0.1495	-0.4293
H12a	0.0661	-0.5373	0.5441	C7b	-0.1977	-0.131	-0.3942
H13a	0.0451	-0.4406	0.4189	C8b	-0.0986	0.0203	-0.2445
H14a	-0.0727	-0.3273	0.3686	C9b	-0.2481	0.0953	-0.1872
H61a	-0.0787	-0.5961	0.2481	C10b	-0.4396	-0.0097	-0.3014
H62a	-0.0234	-0.622	0.3463	C11b	-0.427	0.0542	-0.5488
H63a	-0.0926	-0.6829	0.2787	C12b	-0.4445	0.1197	-0.4891
H71a	-0.0782	-0.7238	0.4418	C13b	-0.3668	0.1806	-0.4257
H72a	-0.0973	-0.6806	0.5118	C14b	-0.2716	0.1761	-0.4218
H73a	-0.1665	-0.7416	0.4443	C15b	-0.2541	0.1107	-0.4814
H81a	-0.262	-0.6316	0.4919	C16b	-0.3318	0.0497	-0.5449
H82a	-0.2812	-0.5369	0.4837	C17b	-0.3145	-0.0151	-0.604
H83a	-0.3504	-0.5978	0.4162	C18b	-0.1947	0.2365	-0.3589

Table B.7: Atomic coordinates for the partially hydrated phase of $Cd_{0.5}$[Cp*Ru(η^6-isophthalate)]

Atom	x	y	z	Atom	x	y	z
H11b	-0.4732	0.018	-0.5865	C6c	-0.4068	0.7024	-0.2452
H12b	-0.5011	0.1224	-0.4914	C7c	-0.2799	0.8474	-0.0991
H13b	-0.3772	0.2195	-0.3902	C8c	-0.0748	0.8372	-0.0808
H15b	-0.1975	0.108	-0.4791	C9c	-0.075	0.6859	-0.2155
H61b	-0.4634	-0.1439	-0.4288	C10c	-0.2802	0.6026	-0.3171
H62b	-0.4162	-0.1388	-0.4867	C11c	-0.206	0.515	-0.0868
H63b	-0.3855	-0.2039	-0.4114	C12c	-0.1038	0.537	-0.0536
H71b	-0.2379	-0.1703	-0.4342	C13c	-0.0573	0.6092	0.017
H72b	-0.1786	-0.0937	-0.4245	C14c	-0.113	0.6595	0.0543
H73b	-0.1479	-0.1587	-0.3491	C15c	-0.2151	0.6375	0.021
H81b	-0.0684	-0.0096	-0.2698	C16c	-0.2616	0.5653	-0.0495
H82b	-0.1002	0.0776	-0.2579	C17c	-0.0487	0.4872	-0.0905
H83b	-0.0695	0.0126	-0.1826	C18c	-0.067	0.731	0.1241
H91b	-0.1892	0.1161	-0.1628	H11c	-0.2336	0.4721	-0.1287
H92b	-0.2893	0.1383	-0.2172	H12c	-0.0707	0.5072	-0.0757
H93b	-0.2587	0.0733	-0.1419	H13c	0.0033	0.6223	0.0367
H101b	-0.4333	0.0331	-0.261	H15c	-0.2482	0.6673	0.0432
H102b	-0.4847	0.0046	-0.3586	H61c	-0.4293	0.6588	-0.287
H103b	-0.454	-0.0604	-0.2833	H62c	-0.4114	0.6879	-0.1941
O1c	0.0363	0.5033	-0.0607	H63c	-0.439	0.7519	-0.27
O2c	-0.0878	0.4298	-0.151	H71c	-0.3405	0.8393	-0.1144
O3c	-0.1145	0.7768	0.1496	H72c	-0.2436	0.8381	-0.0379
O4c	0.0188	0.7447	0.1568	H73c	-0.2712	0.9021	-0.1138
C1c	-0.3056	0.7171	-0.2185	H81c	-0.0898	0.8758	-0.0483
C2c	-0.2532	0.7836	-0.1523	H82c	-0.0287	0.8017	-0.0416
C3c	-0.1596	0.7831	-0.1403	H83c	-0.0564	0.8657	-0.1175
C4c	-0.154	0.7162	-0.1991	H91c	-0.0236	0.7178	-0.1802
C5c	-0.2443	0.6754	-0.2474	H92c	-0.0637	0.629	-0.2001

Table B.8: Atomic coordinates for the dehydrated phase of $Cd_{0.5}$[Cp*Ru(η^6-isophthalate)]

Atom	x	y	z	Atom	x	y	z
Cd1	0.5515	-0.7779	-0.9079	H11	0.6953	-0.2632	0.2363
Cd2	-0.4747	-0.7301	-0.4514	H12	0.7867	-0.2883	0.0773
Ru1	0.8028	-0.1935	0.1808	H13	0.8835	-0.2916	0.0518
Ru2	-0.4072	0.495	-0.8322	H15	0.7974	-0.2448	0.3444
Ru3	-0.732	0.6748	-0.815	H61	0.836	-0.1045	0.3215
Ru4	-0.5427	0.0303	-0.2104	H62	0.8999	-0.118	0.2244
O1	0.6191	-0.229	0.4255	H63	0.8754	-0.0514	0.2505
O2	0.6792	-0.2256	0.4933	H71	0.9602	-0.1457	0.0492
O3	0.9698	-0.2816	0.0817	H72	0.9512	-0.1611	-0.0308
O4	0.917	-0.2619	0.2603	H73	0.9642	-0.0942	-0.0175
C1	0.8341	-0.1023	0.2001	H81	0.8884	-0.1445	-0.0906
C2	0.8736	-0.1196	0.0917	H82	0.8267	-0.1796	-0.0364
C3	0.832	-0.1251	0.0597	H83	0.8292	-0.1104	-0.0595
C4	0.7667	-0.1113	0.1483	H91	0.7109	-0.0933	0.1042
C5	0.768	-0.0971	0.2351	H92	0.6885	-0.15	0.1725
C6	0.8645	-0.0931	0.2548	H93	0.676	-0.0846	0.2164
C7	0.9447	-0.1314	0.0152	H101	0.6777	-0.0935	0.3617
C8	0.8455	-0.1416	-0.0422	H102	0.7241	-0.0986	0.3866
C9	0.704	-0.1096	0.1618	H103	0.715	-0.0365	0.3523
C10	0.7158	-0.0796	0.3453	O1a	-0.4339	0.3066	-0.8214
C11	0.7335	-0.2645	0.2262	O2a	-0.4409	0.3377	-0.9562
C12	0.7888	-0.2797	0.13	O3a	-0.4731	0.6481	-0.8854
C13	0.8474	-0.2817	0.1146	O4a	-0.473	0.572	-0.9955
C14	0.8507	-0.2685	0.1954	C1a	-0.3145	0.5259	-0.9658
C15	0.7953	-0.2534	0.2917	C2a	-0.3355	0.5683	-0.8797
C16	0.7367	-0.2514	0.3071	C3a	-0.3434	0.53	-0.7977
C17	0.6766	-0.2348	0.4117	C4a	-0.3273	0.4639	-0.8331
C18	0.9143	-0.2707	0.1787	C5a	-0.3094	0.4614	-0.937

B.3.2 Dehydrated

Tables B.8, B.9 and B.10 lists fractional atomic coordinates for the partially hydrated phase of $Cd_{0.5}$[Cp*Ru(η^6-isophthalate)].

Table B.9: Atomic coordinates for the dehydrated phase of $Cd_{0.5}$[Cp*Ru(η^6-isophthalate)]

Atom	x	y	z	Atom	x	y	z
C6a	-0.3023	0.5525	-1.0627	H93a	-0.2913	0.4039	-0.7835
C7a	-0.349	0.6393	-0.8648	H101a	-0.2622	0.3807	-1.0079
C8a	-0.3639	0.5473	-0.6916	H102a	-0.3235	0.3848	-0.9953
C9a	-0.3265	0.4036	-0.7825	H103a	-0.2674	0.4229	-1.0762
C10a	-0.2884	0.4068	-1.0118	O1b	-0.5455	0.7427	-0.9708
C11a	-0.4814	0.4322	-0.7282	O2b	-0.5973	0.7453	-0.79
C12a	-0.4975	0.4941	-0.689	O3b	-0.8981	0.7759	-0.6119
C13a	-0.4952	0.5437	-0.7482	O4b	-0.836	0.7755	-0.5475
C14a	-0.4767	0.5315	-0.8467	C1b	-0.7586	0.6	-0.7035
C15a	-0.4606	0.4697	-0.8859	C2b	-0.7995	0.5968	-0.7372
C16a	-0.4629	0.42	-0.8267	C3b	-0.7587	0.5854	-0.8477
C17a	-0.4454	0.3528	-0.8694	C4b	-0.6927	0.5816	-0.8822
C18a	-0.4742	0.5854	-0.911	C5b	-0.6926	0.5907	-0.7931
H11a	-0.4829	0.3999	-0.6896	C6b	-0.7878	0.6115	-0.5917
H12a	-0.5095	0.502	-0.6248	C7b	-0.8711	0.6029	-0.6797
H13a	-0.5057	0.584	-0.7226	C8b	-0.7738	0.5777	-0.9239
H15a	-0.4486	0.4617	-0.9501	C9b	-0.6304	0.5707	-0.9869
H61a	-0.2642	0.5375	-1.1176	C10b	-0.6391	0.5916	-0.7816
H62a	-0.3342	0.5396	-1.0664	C11b	-0.6693	0.739	-0.9335
H63a	-0.3014	0.5958	-1.0608	C12b	-0.7285	0.741	-0.9158
H71a	-0.3496	0.6545	-0.9165	C13b	-0.7837	0.7512	-0.817
H72a	-0.3874	0.646	-0.8037	C14b	-0.7797	0.7595	-0.736
H73a	-0.3177	0.6591	-0.8654	C15b	-0.7204	0.7575	-0.7537
H81a	-0.3835	0.586	-0.6739	C16b	-0.6652	0.7472	-0.8524
H82a	-0.3914	0.5172	-0.6465	C17b	-0.6008	0.745	-0.8717
H83a	-0.3289	0.549	-0.6922	C18b	-0.8396	0.7706	-0.6287
H91a	-0.3623	0.4025	-0.7167	H11b	-0.6333	0.7323	-0.9978
H92a	-0.3255	0.3693	-0.8174	H12b	-0.7312	0.7356	-0.9686

Table B.10: Atomic coordinates for the dehydrated phase of $Cd_{0.5}$[Cp*Ru(η^6-isophthalate)]

Atom	x	y	z	Atom	x	y	z
H13b	-0.8224	0.7526	-0.8055	C8c	-0.6502	0.0482	0.0371
H15b	-0.7177	0.7628	-0.7008	C9c	-0.6413	0.1519	-0.1187
H61b	-0.7765	0.5791	-0.5684	C10c	-0.6114	0.0759	-0.3163
H62b	-0.773	0.6492	-0.5856	C11c	-0.4802	0.0931	-0.2089
H63b	-0.831	0.613	-0.5555	C12c	-0.4794	0.034	-0.1702
H71b	-0.8888	0.6138	-0.6137	C13c	-0.4679	-0.0214	-0.2263
H72b	-0.8793	0.6336	-0.7099	C14c	-0.4572	-0.0177	-0.3211
H73b	-0.887	0.5648	-0.6817	C15c	-0.4579	0.0414	-0.3597
H81b	-0.8017	0.6087	-0.9127	C16c	-0.4694	0.0968	-0.3036
H82b	-0.737	0.5812	-0.9883	C17c	-0.4702	0.161	-0.3456
H83b	-0.7915	0.5386	-0.9153	C18c	-0.4447	-0.0779	-0.382
H91b	-0.6387	0.5657	-1.0334	H11c	-0.4876	0.1292	-0.1723
H92b	-0.6046	0.6051	-1.0037	H12c	-0.4864	0.0316	-0.1084
H93b	-0.6114	0.535	-0.9848	H13c	-0.4674	-0.0599	-0.2011
H101b	-0.6023	0.579	-0.8415	H15c	-0.4509	0.0438	-0.4215
H102b	-0.6347	0.632	-0.766	H61c	-0.5675	-0.0652	-0.3472
H103b	-0.6489	0.5645	-0.7305	H62c	-0.5939	-0.1102	-0.26
O1c	-0.4635	0.2165	-0.3066	H63c	-0.6367	-0.0811	-0.2818
O2c	-0.4777	0.1642	-0.4229	H71c	-0.5889	-0.1134	-0.1085
O3c	-0.4402	-0.1361	-0.3466	H72c	-0.6294	-0.0816	-0.0068
O4c	-0.4378	-0.0747	-0.4731	H73c	-0.6597	-0.1162	-0.0476
C1c	-0.615	-0.0193	-0.2127	H81c	-0.68	0.0211	0.0862
C2c	-0.6254	-0.031	-0.1151	H82c	-0.6135	0.0451	0.0315
C3c	-0.6368	0.0304	-0.0643	H83c	-0.6651	0.0889	0.0531
C4c	-0.6335	0.0801	-0.1305	H91c	-0.6254	0.1661	-0.0851
C5c	-0.6201	0.0494	-0.2221	H92c	-0.6196	0.17	-0.1818
C6c	-0.6019	-0.0747	-0.2827	H93c	-0.6834	0.1617	-0.0822
C7c	-0.6259	-0.0918	-0.0642	H101c	-0.6121	0.1193	-0.3132

Table B.11: Atomic coordinates for $K_4V(NCS)_6$

Atom	x	y	z	Occupancy
V1	0	0	0	0.5
S1	0.51106	0	0.25	1
K1	$\frac{1}{3}$	$\frac{2}{3}$	0	1
N1	0.21162	0	0.38301	0.5
C1	-0.33341	0	0.82043	0.5

Table B.12: Atomic coordinates for $\alpha - Ni(HF_2)(pyz)_2]PF_6$ (**3.1**)

Atom	x	y	z	Atom	x	y	z
P1		-0.0463	0.2	H2	0.238853	0.412212	0.625214
F1	0.16109	-0.04423	0.23603	C3	0.286373	0.199776	0.09098
F2		0.11734	0.2	C4	0.18968	0.295367	0.0960303
F3	-0.01543	-0.04240	0.37911	N2	0.347825	0.153286	-0.00510
F4		-0.20386	0.2	H3	0.310674	0.166221	0.151778
C1	0.338191	0.250040	0.571628	H4	0.149383	0.325678	0.160188
C2	0.24331	0.347243	0.575064	Ni1	0.		0.
N1	0.345986	0.151656	0.496524	H5	0.	0.00775060	0.7
H1	0.397112	0.250067	0.619484	F5	0.530055	-0.00685	0.3373

Table B.13: Atomic coordinates for $Ni(HF_2)(pyz)_2]SbF_6$ (**3.2**)

Atom	x	y	z	Atom	x	y	z
Ni1	0	0	0	F2	0	0.5	0.6968
F3	0	0	0.3255	F4	0	0.5	0.1174
N1	0.1511	0.1511	0	C1	0.2240	0.1761	0.1688
Sb	0	0.5	0.4036	H1	0.20153	0.1225	0.290239
F1	0.1909	0.5	0.4095	H2	0	0	0.5

B.4 $K_4V(NCS)_6$

Tables B.11 lists fractional atomic coordinates for $K_4V(NCS)_6$.

B.5 $[Ni(HF_2)(pyz)_2]X$ Materials

Tables B.12, B.13 and B.14 lists fractional atomic coordinates for $\alpha - Ni(HF_2)(pyz)_2]PF_6$, $Ni(HF_2)(pyz)_2]SbF_6$ and B.14 respectively.

Table B.14: Atomic coordinates for $\beta - Ni(HF_2)(pyz)_2]PF_6$ (**3.3**)

Atom	x	y	z	Atom	x	y	z
Ni1	0	0	0	F2	0	0.5	0.64008
F3	0	0	0.32578	F4	0	0.5	0.14707
N1	0.15047	0.15047	0	C1	0.22268	0.17520	0.16735
P	0	0.5	0.39102	H1	0.20153	0.1225	0.290239
F1	0.00000	0.3404	0.4015	H2	0	0	0.5

Table B.15: Atomic coordinates for $NiF(pyz)_{1.5}(H_2O)_2$ TaF_6 (**3.4**)

Atom	x	y	z	Atom	x	y	z
Ni1	0	0.23877	0.5	N1	0	0.09682	0.5
O1	-0.07124	-0.75149	0.31788	C1	0.03776	0.04633	0.30548
F7	0	-0.37548	0.5	H1	0.06329	0.07495	0.17395
Ta1	0.24399	0	0.60645	N1b	0.34686	0.26516	-0.2076
F1	0.1422	0.08563	0.75196	C1b	0.25864	0.3156	-0.1423
F2	0.2279	0	0.3758	C2b	0.1659	0.3010	0.0563
F3	0.3457	-0.08563	0.4609	H1b	0.2643	0.3590	-0.2366
F6	0.2599	0	0.8370	H2b	0.1103	0.3349	0.09360

B.6 $NiF(pyz)_{1.5}(H_2O)_2$ TaF_6

Table B.15 lists fractional atomic coordinates for $NiF(pyz)_{1.5}(H_2O)_2$ TaF_6.

B.7 $Ni_2F_2(pyz)_3(H_2O)_4(BF_4)_2$

Table B.16 lists fractional atomic coordinates for $Ni_2F_2(pyz)_3(H_2O)_4(BF_4)_2$.

Table B.16: Atomic coordinates for $Ni_2F_2(pyz)_3(H_2O)_4(BF_4)_2$ (**3.5**)

Atom	x	y	z	Atom	x	y	z
Ni1	0.0	0.0	0.25	N1	0.0	0.1522	0.25
Ni2	0.5	0.0	0.25	N2	0.0	0.3478	0.25
O1	0.1326	0.0	0.1453	C1	0.0882	0.2015	0.2967
F4	0.6765	0.0	0.25	C2	0.0882	0.2985	0.2967
B1	0.3115	0.3107	0.5	H1	0.146	0.1697	0.3273
F1	0.205	0.3633	0.5	H2	0.146	0.3303	0.3273
F2	0.411	0.3714	0.5	C3	0.4193	0.0544	0.4513
F3	0.3145	0.2503	0.5795	N3	0.5	0.0	0.4018

Table B.17: Atomic coordinates for $Na_2Mn[Mn(CN)_6]$ $2H_2O$ (**4.1**)

Atom	x	y	z	Atom	x	y	z
Mn1	0.5	0.5	0.5	C1	0.5034	0.2031	0.8357
Mn2	0.5	0.0	1.0	C2	0.1828	0.4923	0.4981
N1	0.5058	0.3233	0.7463	C3	0.5042	0.1643	0.2055
N2	0.2876	0.4917	0.4831	O1	0.2522	0.216	0.2874
N3	0.4998	0.2555	0.3254	Na1	0.2425	0.448	0.0347

Table B.18: Atomic coordinates for $Na_2Mn[Mn(CN)_6]$ (**4.2**)

Atom	x	y	z
Mn1	0	0	0
Mn2	$\frac{1}{3}$	$\frac{2}{3}$	$\frac{1}{6}$
N1	0.3335(7)	0.3789(6)	0.10324(15)
C1	0.2316(6)	0.2436(6)	0.05970(17)
Na1	0	0	0.19424(10)

B.8 $Na_2Mn[Mn(CN)_6]$ $2H_2O$ and $Na_2Mn[Mn(CN)_6$

Tables B.17 and B.18 lists fractional atomic coordinates for $Na_2Mn[Mn(CN)_6]$ $2H_2O$ (**4.1**) and $Na_2Mn[Mn(CN)_6$ (**4.2**), respectively.

B.9 $Mn(CN)_6Mn_4(OH)_4$ $5H_2O$

Table B.19 lists fractional atomic coordinates for $Mn(CN)_6Mn_4(OH)_4$ $5H_2O$ (**4.3**).

Table B.19: Atomic coordinates for $Mn(CN)_6Mn_4(OH)_4$ $5H_2O$ (**4.3**)

Atom	x	y	z	Atom	x	y	z
Mn1	0.0	0.0	0.0	Mn3	0.1762	0.1945	-0.2518
C1	-0.1553	0.0096	0.0332	Mn4	0.0	0.0	0.3316
N1	-0.2515	0.0127	0.0509	O1	0.0	0.0	0.124
Mn2	0.0	0.0	0.5	O2	-0.5176	-0.161	-0.0427
C2	0.1143	0.1848	0.4673	O3	-0.814	-0.9657	-0.625
N2	0.1769	0.2963	0.4492	O4	-0.6792	0.114	0.1275

Table B.20: Atomic coordinates for $Mn_5(CN)_{13}NMe_4$ (**4.4**)

Atom	x	y	z	Atom	x	y	z
Mn1	0	0	0	Mn3	0.1762	0.1945	-0.2518
C1	-0.1553	0.0096	0.0332	Mn4	0	0	0.3316
N1	-0.2515	0.0127	0.0509	O1	0	0	0.124
Mn2	0	0	0.5	O2	-0.5176	-0.161	-0.0427
C2	0.1143	0.1848	0.4673	O3	-0.814	-0.9657	-0.625
N2	0.1769	0.2963	0.4492	O4	-0.6792	0.114	0.1275

B.10 $Mn_5(CN)_{13}NMe_4$

Table B.20 lists fractional atomic coordinates for $Mn_5(CN)_{13}NMe_4$ (**4.4**).